Fysisk institutt

Strange and non-strange baryon production in ultrarelativistic sulphur-tungsten and sulphur-sulphur collisions

by
Håvard Helstrup

a thesis submitted to Fysisk institutt, Universitetet i Bergen,
in partial fulfilment of the requirements for
the degree of Doctor Scientiarum

April 1993
Universitetet i Bergen
Bergen, Norway

Abstract

Relativistic heavy ion collisions provide an opportunity to create a new phase of matter, the quark gluon plasma, in the laboratory.

A possible quark gluon plasma will be very short-lived, and only its decay products can be observed. There exists no unambigous signal to identify plasma formation yet, although several candidates have been suggested. An enhanced production of strange particles is one of these proposed signals.

The WA85 experiment measures strange particle production ratios in a narrow window in rapidity and transverse momentum. At present, WA85 is the only collaboration who have published results on multistrange particles. A remarkably high $\overline{\Xi^-}/\overline{\Lambda}$ ratio has been observed in sulphur-tungsten reactions.

From 1991, the experimental program of WA85 is carried forward by the WA94 collaboration. An extended study of production ratios of baryons with 0, 1, 2 and 3 units of strangeness is in progress, To accomplish this, protons and antiprotons must be identified among the non-decaying particles (mostly pions) in the detector setup. A Ring Imaging Čerenkov (RICH) detector is used to determine the particle velocity. This information can be used to deduce the particle mass.

A simulation study is carried out to study details on the feasibility of such an approach, and to decide what measures to take to reduce noise levels.

Experimental data using the RICH was taken in spring 1992. The analysis of these data is in an initial phase, but it seems justified that the RICH signal itself can be reliably reconstructed.

An enhanced version of the WA85/94 detector setup will be used by the WA97 collaboration to measure baryon production ratios in the lead beam foreseen in the autumn of 1994. This detector setup is discussed in the final chapter of the thesis.

Preface

It has been a great pleasure to take part in the work of the WA85, WA94 and WA97 collaborations during the last three years. A large number of people have contributed to the success of these experiments. I want to thank all of them; the list would grow too long if they should all be mentioned explicitly.

I have enjoyed to work at Fysisk institutt, Universitetet i Bergen. I would like to thank all my colleagues at the department for providing a good climate for work, both in the scientific and in the social context.

First and foremost I would like to thank my supervisor, Professor Gunnar Løvhøiden, for his continued support and encouragement. I would also express my thanks to Tor Fredrik Thorsteinsen for his support and stimulating discussions.

I have been very fortunate to be able to work in close collaboration with the spokesman of our experiments, Dr. Emanuele Quercigh. His valuable guidance and suggestions are highly appreciated.

Several computer-related problems have been solved by Ken Knudson. I am grateful for his quick replies and continued interest in all the problems and difficulties arising while operating physics software.

Bergen was a newcomer in the collaborations when I started my thesis work in 1990. I am indebted to all the people who helped us join the collaborations in a smooth and rapid way, in particular the members of the group from University of Birmingham.

A special thank to my fellow Ph.D.-student and now spokesman of the WA85 collaboration, David Evans, who have been very helpful in my recent work with analysis of the WA85 1990 data.

Experimental relativistic heavy ion collisions is a young field of science. This is reflected in the Bergen nuclear physics group, where a significant part of the effort in this field is carried out by students. I am very grateful for the stimulating collaboration with Erling Andersen and Alv Kjetil Holme, without whom this work would hardly have been possible.

Nuclear physics is a very internationally oriented field. I am very grateful for having been able to take part in a number of international activities, such as CERN Summer Student course, Nordic Summer School in Nuclear Physics at Falsterbo, Sweden and NATO Advanced Science Institute in Il Ciocco, Italy. I want to thank all my new friends who helped make all these events both instructive and enjoyable experiences. It has also been a great pleasure to take part in a number of Norwegian Student Seminars in Nuclear Physics, where I have learnt to know fellow students and scientific staff from Oslo and Trondheim and their scientific projects.

Heavy ion collisions produce huge amount of raw data. During 1991-92 400 raw data

tapes, each with a capacity of 200 megabytes, have been processed in Bergen. Each tape consumed more than ten hours of IBM 3090 processor time. I want to thank IBM Bergen Scientific Centre for providing these computer resources, and for mounting the vast amounts of computer tapes needed to handle this task.

This work was paid by a grant from Norges Allmennvitenskapelige Forskningsråd (NAVF). Financial support for travel and data analysis has been received from NAVF and from Universitetet i Bergen.

Finally, I would like to thank all my friends and relatives for their continued support and encouragement.

Bergen, April 1993

Håvard Helstrup

Contents

List of Figures

List of Tables

Chapter 1

The Quark Gluon Plasma

1.1 Introduction

The possibility to create a new phase of matter, the Quark Gluon Plasma, is a major motivation for the study of relativistic heavy ion collisions. Given sufficient temperature (energy) or density, the individuality of the protons and neutrons in the colliding nuclei may get lost, and an entity containing a large number of 'free' quarks and gluons may be formed.

In the Big Bang theory, it has been suggested that the Universe consisted of quark gluon plasma in its early phases, until it cooled down to a temperature of 200 MeV, after about 10^{-5} s.

Although a quark gluon plasma may be formed in heavy ion collisions, it will be very short-lived, and there is still no unambiguous signal available to identify plasma formation.

This thesis discusses the investigation of the production of strange particles in relativistic ion collisions done by the WA85 collaboration and its successors at CERN. An enhanced production of strange particles has been suggested as a signal for plasma production. Even if no plasma is produced, the experiment may reveal interesting information on the physics of the fireball produced by colliding heavy nuclei, the highest concentration of energy presently available on Earth.

1.2 Quarks and Gluons

Since the quark model of hadrons was introduced independently by Gell Mann and Zweig in 1964, numerous experiments have tried to observe isolated quarks. To this date, none of them have succeeded. This has led to the development of the concept of confinement, now a crucial part of the Quantum Chromodynamics (QCD) theory of strongly interacting particles.

In QCD the strong force relates to a 'colour' charge, in close analogy to the role of the familiar electrical charge in Quantum Electrodynamics (QED), the well established theory for the electroweak forces. This colour charge comes in three different versions, labeled 'red', 'green' and 'blue'. Only colour-neutral particles exist in nature. This can be accomplished either by the combination of three different colour charges (red + green

+ blue makes white), or by a combination of a colour charge with its anti-charge. Both combinations exist, all baryons consist of three quarks carrying different colour charges, mesons are composed of a quark and an anti-quark carrying the same colour/anti-colour.

At short distances, the field lines around a colour charge are believed to be spherically symmetric, and rather similar to the field lines surrounding electrical charges, giving rise to a potential of the form $V(r) \sim 1/r$. At larger distances, at the order of one femtometer (fermi), the colour field lines tend to group together to form a flux tube connecting two colour charges. This causes the energy of the field to grow linearly with the quark separation, and to give a free coloured quark an infinite amount of energy. Hence quarks can only exist in the close vicinity of other quarks, making the net colour charge of the composite object zero.

When quarks are forced to separate, a flux tube is formed. Due to the finite quark masses, this flux tube, or string, can break down by producing a quark-antiquark pair. Thus the original excited colour-neutral object turns into two new objects, both still colour neutral. Such processes explain the multitude of produced particles observed in high energy particle reactions.

Once colour-neutral hadrons are produced, reactions can be understood at the hadronic level. To study the individual quarks, one would need to operate at sufficiently small separation distances that the $1/r$ character of the inter-quark potential is retained. At normal conditions, this is not possible, as the hadrons themselves would produce reactions while the separation distance remains significantly larger.

As was first suggested by Collins and Perry [Col75], quark degrees of freedom might be observed if matter could be compressed to several times normal nuclear density. QCD calculations show that similar behaviour can be expected when nuclear matter is heated to high temperatures. The situation is outlined in the phase diagram shown in fig. 1.1. Below the phase barrier quarks are confined, and only hadronic matter can be observed. In the quark gluon plasma phase above the barrier the quarks act as 'normal' free particles. The arrows in figure 1.1 suggest some available paths to the quark gluon plasma phase. The early Universe cooled down from very high temperatures into the hadronic phase. In neutron stars matter may be compressed to such densities that the quark matter phase is reached. In heavy ion collisions, the matter is initially compressed, then temperature increases and expansion starts before the hot fireball returns to the normal phase.

Heavy ion collisions at relativistic energies provide the only possible way to reach the quark gluon plasma phase on Earth. In the last decade, facilities to provide such collisions have been made available, both in the US (Brookhaven National Laboratory) and at the European Centre for Nuclear Research CERN in Geneva.

1.3 Heavy Ion Collisions

Relativistic heavy ion collisions is believed to be the only possible way to create sufficiently hot and dense matter to produce a quark gluon plasma in the laboratory. This system is of quantum nature, making the tools of particle physics necessary to describe the observed phenomena. On the other hand, the number of particles produced in such a collision may reach thousands, suggesting statistical or thermodynamical degrees of freedom to be relevant as well.

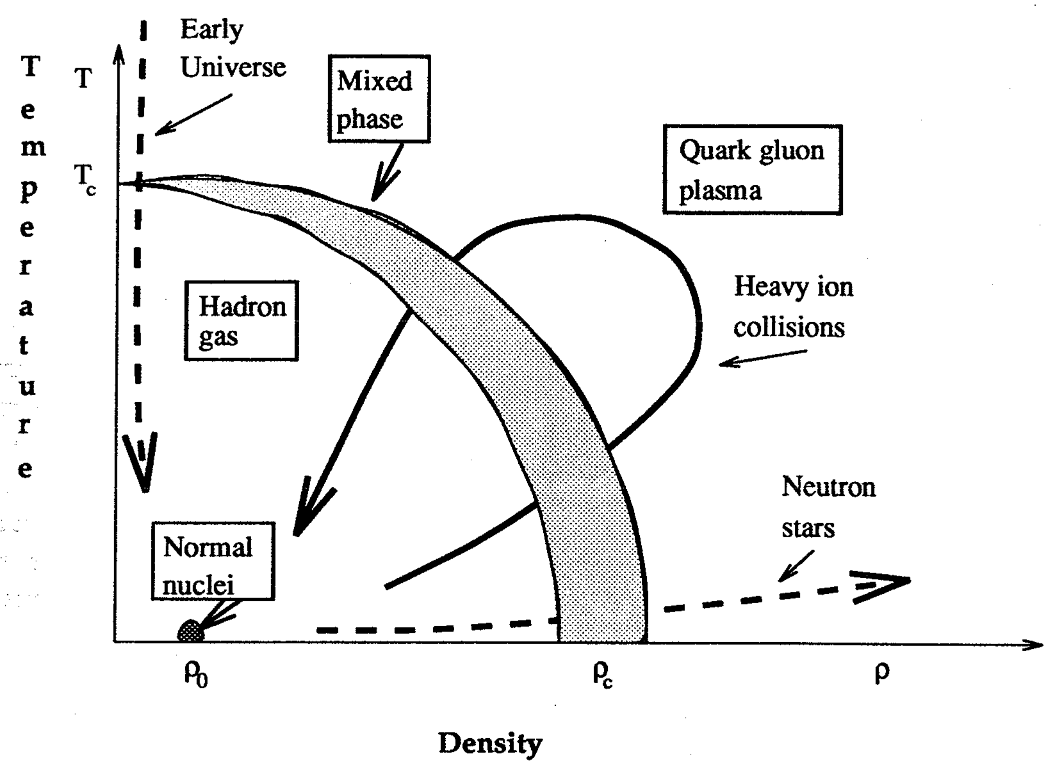

Figure 1.1: Quark matter phase diagram

1.3.1 Kinematics

Observable quantities in heavy ion collisions are often plotted as functions of rapidity or transverse momentum, energy or mass.

Unless otherwise stated, the normal particle physics convention of setting $\hbar = c = 1$ is used.

The rapidity y is closely related to the velocity of the particle, and is defined by

$$y = \text{artanh}(v_{\|}) = \text{artanh}(\frac{p_{\|}}{p^0}) = \frac{1}{2}\ln(\frac{E + p_{\|}}{E - p_{\|}}) \tag{1.1}$$

This entity is additive under Lorentz transformations. The parallel direction is normally defined by the beam axis.

If a beam of particles with a rapidity y_b in the laboratory system impinges on a target with a rapdity $y_t = 0$, beam particles that do not interact with the target leave the system with a rapidity close to y_b. Particles from the target that do not interact with the beam, will have a rapidity close to y_t. Particles originating from the interaction zone have a rapidity close to that of the center of mass of the system.

By investigating the rapidity distribution of various observables, it is thereby possible to classify which part of the reaction volume the different particles originate from.

In high energy experiments with fixed target, the major part of the energy of the outcoming particles will go in the direction of the beam, to ensure momentum conservation. Particles emitted in the transverse directions (with respect to the beam) must have undergone interactions in the target. A significant transverse momentum component can also be produced by a hot thermal source in the target.

Detected particles in the transverse directions will thereby provide information of the reaction processes of the collision. Various transverse observables are used:

Transverse momentum, p_t: the fraction of the linear momentum emitted in the transverse directions.

Transverse energy, E_t: the fraction of the collision energy emitted in the transverse directions.

Transverse mass, m_t: defined by $m_t = \sqrt{p_t^2 + m^2}$

The temperature of the system can be extracted from the transverse mass distribution. To measure this quantity properly, particle identification is necessary.

1.3.2 Reaction dynamics

When two nuclei collide, they will generally not overlap completely. The situation may be as described in figure 1.2. Some fraction of the projectile nucleus will interact with a fraction of the target. The remaining parts of the projectile and target will leave the reaction area comparatively undisturbed. These particles are referred to as 'spectators', the particles in the dense reaction area are called 'participants'.

The impact parameter b is defined as the distance between the centres of the colliding nuclei, measured perpendicular to the beam axis. Head-on collisions, with an impact

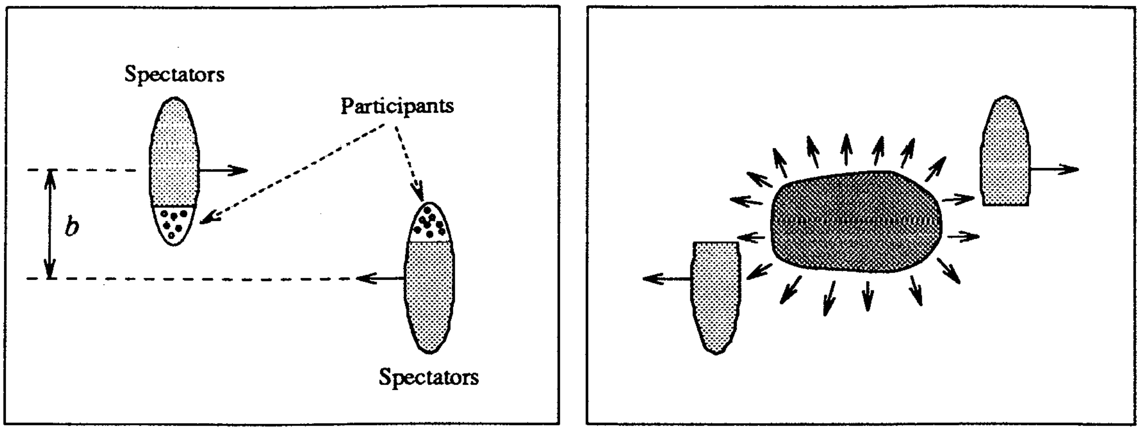

Figure 1.2: Relativistic collision between two nuclei. Lorentz contraction will make the spherical nuclei disk-shaped

parameter b=0, will produce the maximum number of participant nucleons, and the maximum size and density of the hot and dense reaction zone.

In symmetric collisions (when the projectile and target isotope is the same), any deviation from b=0 is likely to introduce spectator nucleons both from the projectile and the target. When the projectile is much smaller than the target, as is the case in many of the CERN and BNL experiments, target spectators will always be present. On the other hand, a complete overlap of target and projectile will be possible even for impact parameters greater than zero.

A quark gluon plasma is most likely to be seen in central collisions. This corresponds to events with a small impact parameter. As this parameter is not experimentally available, various other trigger conditions have been used to identify interesting events, mainly a threshold on the energy or the number of particles emitted in transverse directions.

1.3.3 Plasma evolution

If a quark gluon plasma is formed in an ion collision, it is expected to evolve as outlined in figure 1.3. The light cone is limited by the trajectories of the incoming projectile and target nuclei. A possible quark gluon plasma will have a short life time, at the order of some fm/c. When it cools down to the critical temperature, it will start to hadronise, and the mixed phase of QGP and newly formed hadrons will exist for some other fm/c. Later on a hot and dense interacting hadron gas is formed. Finally the produced particles stop colliding and fly apart, eventually to be seen in detectors located far away from the collision point.

1.4 The Bag Model

The confinement property of the strong force can be described by the MIT bag model [Cho74]. In this model the quarks and gluons can act as free particles within well defined

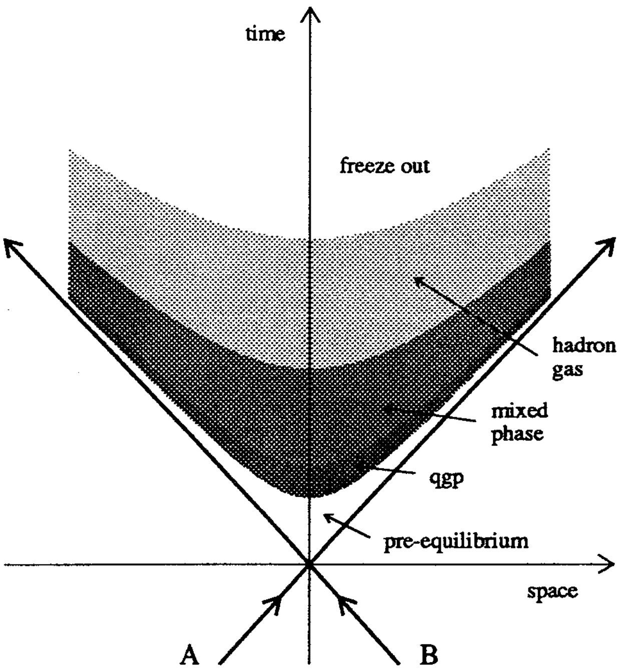

Figure 1.3: Space-time evolution of a relativistic heavy ion collision with quark gluon plasma formation

regions of space, defined as 'bags'. Inside the bags the quarks and gluons experience an excited perturbative QCD vacuum. This perturbative vacuum is distinguished from the normal QCD vacuum by addition of a 'bag constant' B to the energy density of the bag volume. The total energy of the 'quantum gas' within the gas is then given by

$$E = E_r + BV \tag{1.2}$$

where E_r is the internal energy of the gas, B is the bag constant, and V is the volume of the gas. The equation of state of the matter inside the bags is given by

$$p = \frac{1}{3}(\varepsilon - 4B) \tag{1.3}$$

where p is the pressure, ε is the energy density and B is the bag constant. This is to be compared to the Stefan-Boltzmann expression valid for a normal hadron gas, where

$$p = \frac{1}{3}\varepsilon \tag{1.4}$$

In normal matter these bags can be associated with the individual hadrons. At high temperatures and densities, one could imagine that the bags belonging to each individual hadron would overlap, making it possible for the quarks and gluons originating from different hadrons to interact freely. A quark gluon plasma could be regarded as a giant bag, containing quarks and gluons corresponding to several hadrons.

As a quark gluon plasma would correspond to the interior of such a bag, the bag equation of state (1.3) is valid. Normal matter obey the hadron gas equation of state (1.4). If a quark gluon plasma is produced, a phase transition will occur when the plasma cools down. To obtain experimental information from the quark phase, it is necessary to know how the various signals will be affected by the transition process.

1.5 Lattice QCD

To study the phase transition in more detail, predictions from QCD calculations are useful. In particular predictions of the order of the phase transition, along with the critical temperature are needed. In general QCD integrals cannot be solved analytically. To study consequences of the theory, different numerical approximations have to be carried out. A popular approach is to replace the four continuous space-time dimensions with a finite four-dimensional lattice. Thus one can avoid some divergences encountered in continuum QCD, and at the same time make the problem manageable within a finite amount of available computing power. Ideally one would like an infinitely small spacing between lattice points, but this is limited by computer resources.

The zero temperature phase of QCD, corresponding to the ground state properties of the different elementary particles, is characterized both by quark confinement and by spontaneous breaking of chiral symmetry. The latter property of QCD gives rise to the differences of left and right, as experienced by the weak force, and is also necessary to describe massive quarks in the model. Both of these features are supposed to be lost in the high temperature phase of QCD. In principle one could have two phase transitions, one for the confinement/deconfinement and another at chiral symmerty restorations. Lattice

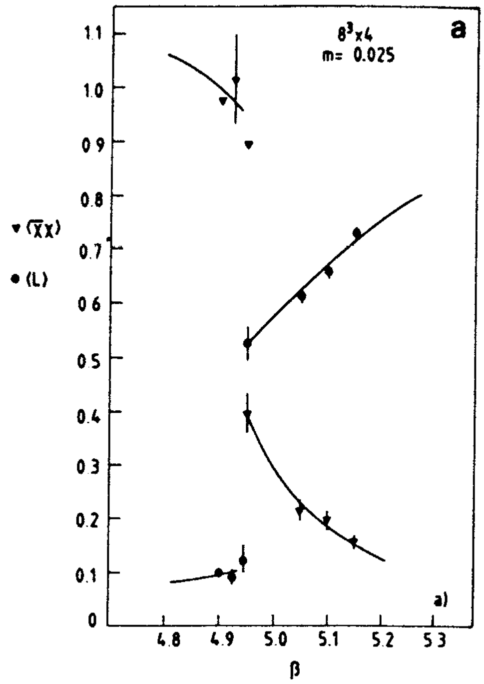

Figure 1.4: Order parameters of QCD phase transitions. Figure taken from [Kar87]

calculations [Kar90] indicate that these transitions occur at the same critical temparature, so that only one phase transition should be observed experimentally.

Phase transitions can be characterised by associated order parameters. An order parameter vanishes on one side of the phase transition, and takes non-zero values in the less symmetric phase on the other side of the transition. A phase transition is known as *first order* if the order parameter has a discontinuous jump at the transition points. In *second order* transitions the order parameter itself is continuous, but the first derivative of the order parameter exhibit a discontinuous jump. Higher order transitions are defined in a similar way: a n-th order phase transition has a discontinuity in its *(n-1)*-th derivative.

The order parameters for the QCD phase transitions are the Polyakov loop <L> for the confinement-deconfinement transition, and the chiral condensate $< \bar{\chi}\chi >$ for the chiral symmetry restoration [Kar87]. In figure 1.4, taken from [Kar87], these parameters are plotted as a function of β, which is directly related to the temperature. The Polyakov loop, <L>, is related to the free energy of static quarks. The order parameter of the chiral symmetry transition, the chiral condensate $< \bar{\chi}\chi >$, vanishes when chiral symmetry is restored above the phase transition, but takes a finite value in the normal phase of broken symmetry.

In the simplest approach all quark masses are infinite [Kar90]. The quarks then remain at fixed coordinates in the lattice, leaving only gluon degrees of freedom. Since the gluons mediate the colour field, which in turn causes the quark confinement, this could still be a good starting point to study the QCD at high temperatures. Current calculations find a first order phase transition with a critical temperature T_c in the range 150-250 MeV [Pet91].

Several attempts have been made to include dynamic quarks in the lattice. The introduction of fermions makes non-physical degeneracies appear. In ref. [Pet91] calculations with four degenerate flavours are presented. These calculations agree on the existence of a phase transition in the same range of T_c, but some of the calculations conclude that the phase transition appears to be continuous, whereas others observe a first order transition. Further calculations are needed to settle this issue.

1.6 QGP signatures

If a quark gluon plasma is formed in a heavy ion collision, it will only exist for a very short time, at the order of some fm/c, or some 10^{-23} seconds. During this life time, the plasma will only move very small distances, as can be readily seen from the first unit of time mentioned above.

Any detector in accelator-based experiments must be placed at macroscopic distances from the target, at least at the order of centimetres away from the reaction area. Thus, the plasma cannot be studied directly. Only the final hadrons can be observed experimentally, and careful calculations are needed to show how an initial plasma phase may influence the final hadron production.

Unfortunately, there exists as yet no unambigous signal that will prove or disprove plasma formation in the collision zone. No new particles are expected, and many effects can be produced by several different mechanisms. In particular, in the multitude of hadrons produced in such collisions secondary scatterings between these hadrons are expected to be an important part of the reaction dynamics. Such scatterings will tend to disturb any possible signal from the original plasma decay.

Even with these difficulties taken into account, a number of signals for plasma production have been proposed. Quite a few of them have also been observed experimentally during the last five years, but none of them provide a clean proof for plasma production. One of these signals, strangeness enhancement, forms the basis of the experimental effort carried out by the WA85/WA94/WA97 collaborations. This signal will be discussed in more detail in the next chapter. Some other signals will be mentioned in the remainder of this section.

1.6.1 Global signals

Phase diagram

A classical phase transition can be described by a plateau followed by a second rise in a plot of relevant thermodynamic variables, for example in a pV-diagram of the water-vapour phase transition. An intuitive approach, suggested by Van Hove (ref. [vHo85]), is to try to observe something similar in the spectra produced in heavy ion reactions. The transverse momentum, p_t, is closely related to the temperature, and the energy density can be related to the number of produced particles per unit of rapidity, suggesting a scenario as scetched in figure 1.5b. A similar pattern was observed in cosmic ray exposures by the JACEE collaboration at quite an early stage [Bur86], as shown in figure 1.5a. The plateau shape has been observed in later efforts to study this effect in heavy ion reactions in the laboratory, but no second rise have been reproduced. As an example, WA80 data as they appear in [Jac91], are shown in figure 1.6.

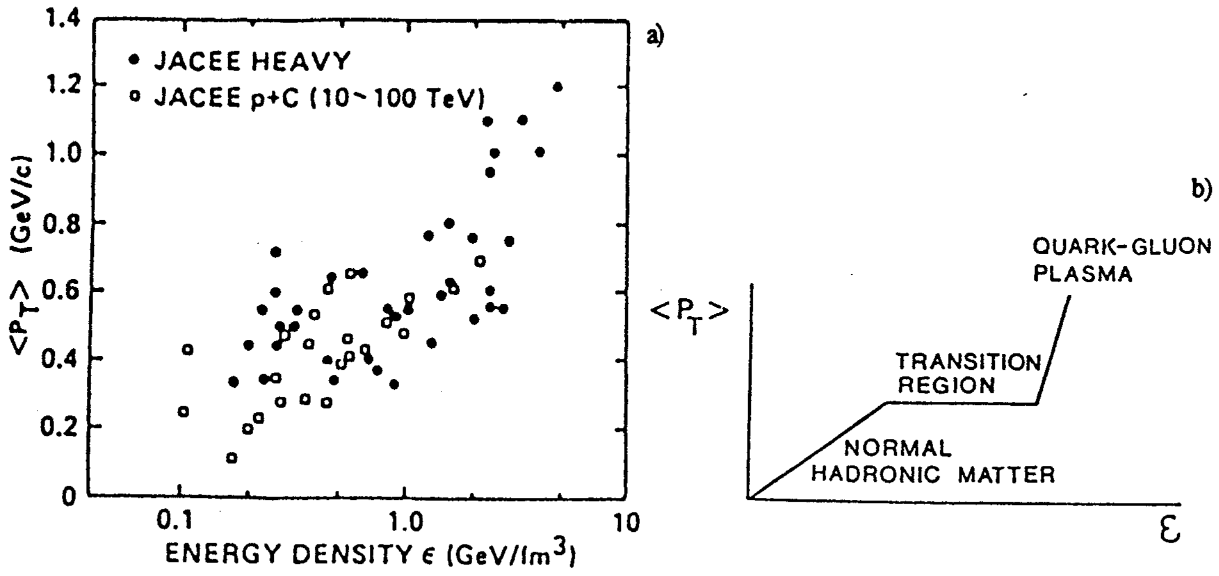

Figure 1.5: $p_t$vs. energy density as observed by JACEE (a), along with possible explanation (b). The figure is taken from ref. [Sch92]

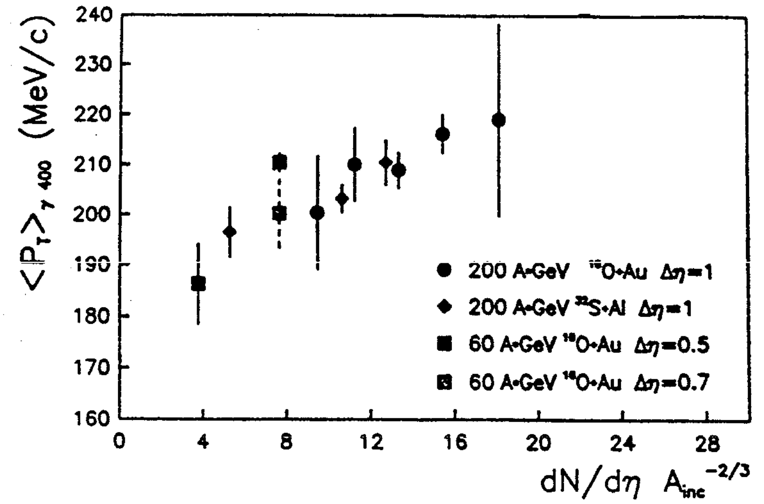

Figure 1.6: p_t vs. energy density as observed by WA80, taken from [Jac91]

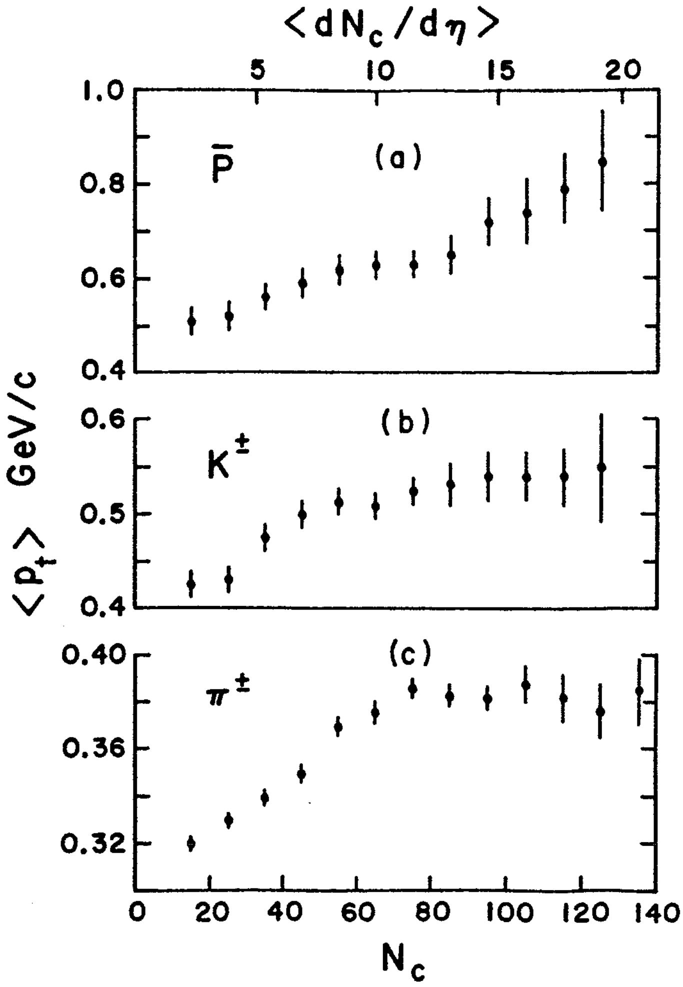

Figure 1.7: p_t vs. energy density for various particles species observed by E735, taken from [Ale90]

Recently, the E735 Collaboration at Fermilab (ref [Ale90]) claimed to see a second rise in $p\bar{p}$ collisions at a centre-of-mass energy of 1.8 TeV. Quark gluon plasma production in such a small system would be rather surprising, and several other explanations have been proposed. In particular, a closer look into the data (figure 1.7) shows that the second rise is only observed for antiprotons. On the other hand the plateau structure is not very well developed there.

The distributions for kaons and pions show the familiar pattern of initial rise then a plateau that extends to the highest measured densities. This could be an indication of a different production mechanism for antiprotons compared to other particles, and is less compatible with an hypothesis of thermal production of all particles from a central hot zone.

Transverse momentum distributions

The emission of particles (mainly pions) from a hot fireball in thermal equilibrium can be described by the formula

$$\frac{1}{p_t}\frac{dN}{dp_t} = \frac{1}{m_t}\frac{dN}{dm_t} = \frac{m_t}{T}K_1\left(\frac{m_t}{T}\right) \tag{1.5}$$

which was first suggested by Hagedorn [Hag83]. K_1 is the modified Bessel function.

This expression can be approximated by [Egg91]

$$\frac{1}{p_t}\frac{dN}{p_t} = \frac{1}{T}\sqrt{m_t}\exp-\frac{m_t}{T} \tag{1.6}$$

The transverse mass m_t is defined as $m_t = \sqrt{p_t^2 + m^2}$. The cross section and the m_t can be measured experimentally. The temperature of the hot zone is then extracted from the spectra according to the Hagedorn formula. This has been done by almost all the heavy ion experiments. They generally see a temperature in the region of 150-200 MeV, which is in good agreement with the critical temperature for the QGP phase transition as predicted by lattice QCD.

As shown in figure 1.8, the distributions deviate from the exponential shape in the high and low p_t regions. (The p_t distributions shown in the figure have a similar shape to the m_t distributions discussed above. p_t distributions can be measured as a 'global observable', whereas m_t distributions require particle identification. To a good approximation, however, all emitted hadrons can be considered as pions.) Already the proton-nucleus reaction shows clear deviations from the exponential shape observed in pp experiments. The effect is even stronger in nucleus-nucleus interactions.

This shape can be explained by collective flow effects [Cse89]. A systematic study of the collective flow in different reactions would provide information on the equation of state of the hot matter, and would in this way contain information of a possible phase transition.

On the other hand, the enhancement at high p_t can be explained by the Cronin effect, the enhanced production of high p_t particles by multiple scattering within heavy nuclei, which was first discovered by J.W.Cronin and collaborators in 1975 [Cro75]. In nucleus-nucleus collisions such effects are expected to be present both in the target and in the projectile. This could explain the large enhancement observed in these reactions.

The enhancement at low p_t is not yet fully understood, but several mechanisms have been suggested to contribute to this effect. Among them are production of resonances, which in turn decay to pion pairs, rescattering effects in the reaction zone and phase space effects [Sch92]. Van Hove has also suggested this effect to be due to decay of supercooled droplets of quark gluon plasma, which eventually would produce a number of pions [vHo88].

Interferometry

Interferometry studies provide another approach to obtain information on the global features of the hot reaction zone. The technique is based on ideas developed by Hanbury Brown and Twiss [Han54] to measure stellar radii. Although the light waves reaching the Earth are incoherent, any two photons arriving at any instant will produce normal interference patterns. When the amplitudes are averaged over time, these interference patterns get washed out, and no maxima or minima are observed. However, when the instant intensity, as produced by the interference pattern, is recorded, a dependence on the distance between the two photon detectors is retained. This dependence is closely related to the $d \sin\theta$ dependence of the interference pattern, and can be used to determine the radius of the emitting star [Han56].

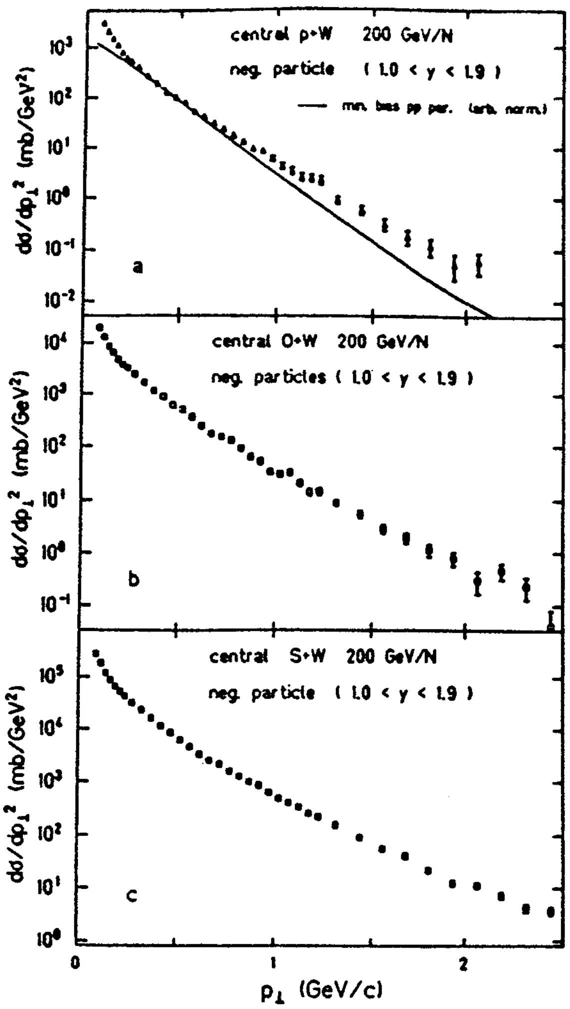

Figure 1.8: p_t distributions measured by HELIOS. The straight line show a pure exponential function, as observed in pp reactions. The figure is taken from ref. [Jac91]

A similar technique can be used to study source sizes in high energy particle reactions, as first discussed in [Gol60]. Charged pion pairs replace the photons detected by Hanbury Brown and Twiss' interferometer. The experimental observable is the correlation function,

$$C(P_1, P_2) = \frac{N_2(P_1, P_2)}{N_1(P_1)N_1(P_2)} \tag{1.7}$$

where P_i are the four-momenta of the pions, N_2 is the cross section for the simultaneous observation of two pions with the given momenta, and N_1 is the cross section to observe one pion with the specified four-momentum.

The correlation function relates to the Fourier transform of the source size by

$$C(P_1, P_2) = 1 + \lambda\,|\rho(Q)|^2 \tag{1.8}$$

where Q is the four-momentum difference $P_1 - P_2$ and $\rho(Q)$ is the Fourier transform of the space-time source density. λ is a chaoticity parameter, taking account of the fact that the source is not perfectly incoherent.

The source size extracted from heavy ion collisions by this method corresponds to the size of the hot zone at freeze-out, when the hot and dense matter is turned into hadronic particles, mainly pions.

Several groups have made this kind of measurements. The NA35 collaboration reported a source radius $\sim$ 8 fm [Bam88] in the transverse direction at mid rapidity. This value is a factor of two greater than the sum of the projectile and target radii, and can be taken as a good indication that a central hot zone is formed in these reactions. Later measurements with higher statistics gave a slightly smaller source size (around 6 fm [Sey92]), but this is still significantly larger than the pure geometrical overlap of the projectile and target.

The E802 collaboration, and its successor E859, have measured different two-particle correlations at AGS energies (15 GeV per nucleon). The pion interferometry gives a source size close to the size of the projectile, in contrast to NA35 results. Two-kaon correlations became available recently [Zaj92]. At first sight they appear to give a narrower distribution than the pion correlation function (figure 1.9). When fully corrected, including the proper Lorentz transformations, kaon correlations yield the same source size as the pion correlation function; 3.5 fm in the E802/E859 case.

Both NA35 and E802/E859 investigate correlation effects around mid rapidity, where a hot, possibly deconfined, fireball is expected to be formed. The WA80 collaboration made interferometry measurements in the target fragmentation region [Kam92]. In an early study using oxygen as projectile, they observe a decreasing source radius when going to heavier targets. This effect may be due to rescattering of pions, but is not yet fully understood.

Direct photons

Since the electromagnetic force is much weaker than the strong nuclear force observed by particles carrying colour charge, the mean free path of a particle interacting only electromagnetically is much longer than the mean free path of a strongly interacting one. Photons produced inside a small volume of quark gluon plasma would therefore have a good chance to reach a detector without undergoing secondary interactions.

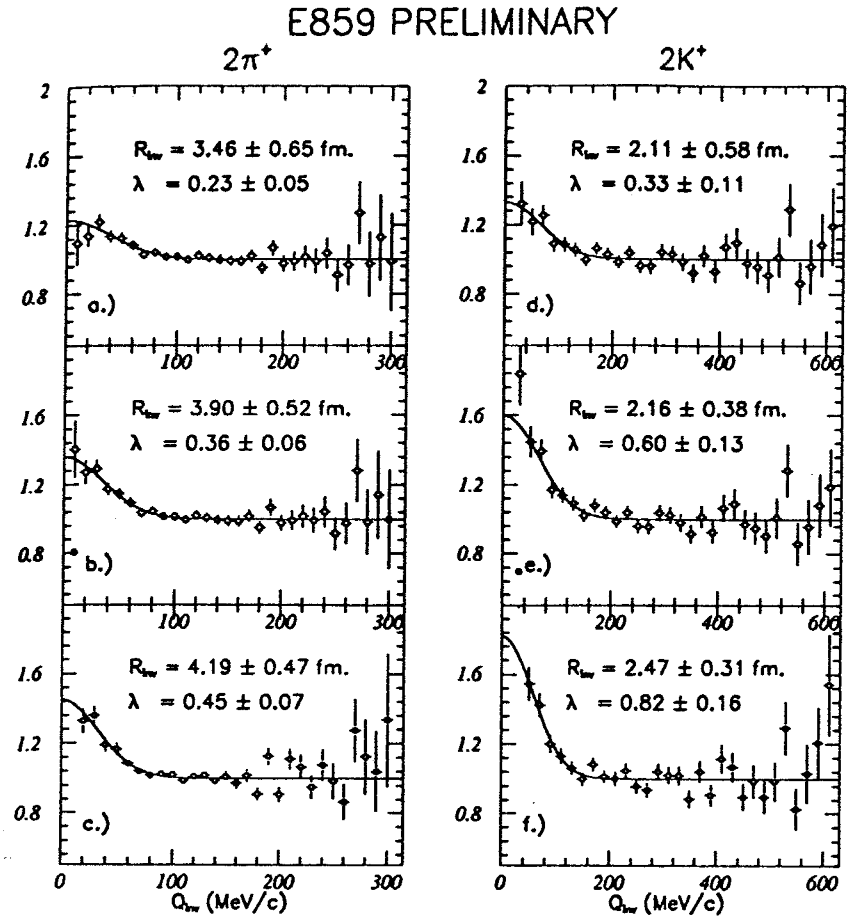

Figure 1.9: Pion and kaon correlation functions as measured by E859. The figure is taken from ref. [Zaj92]

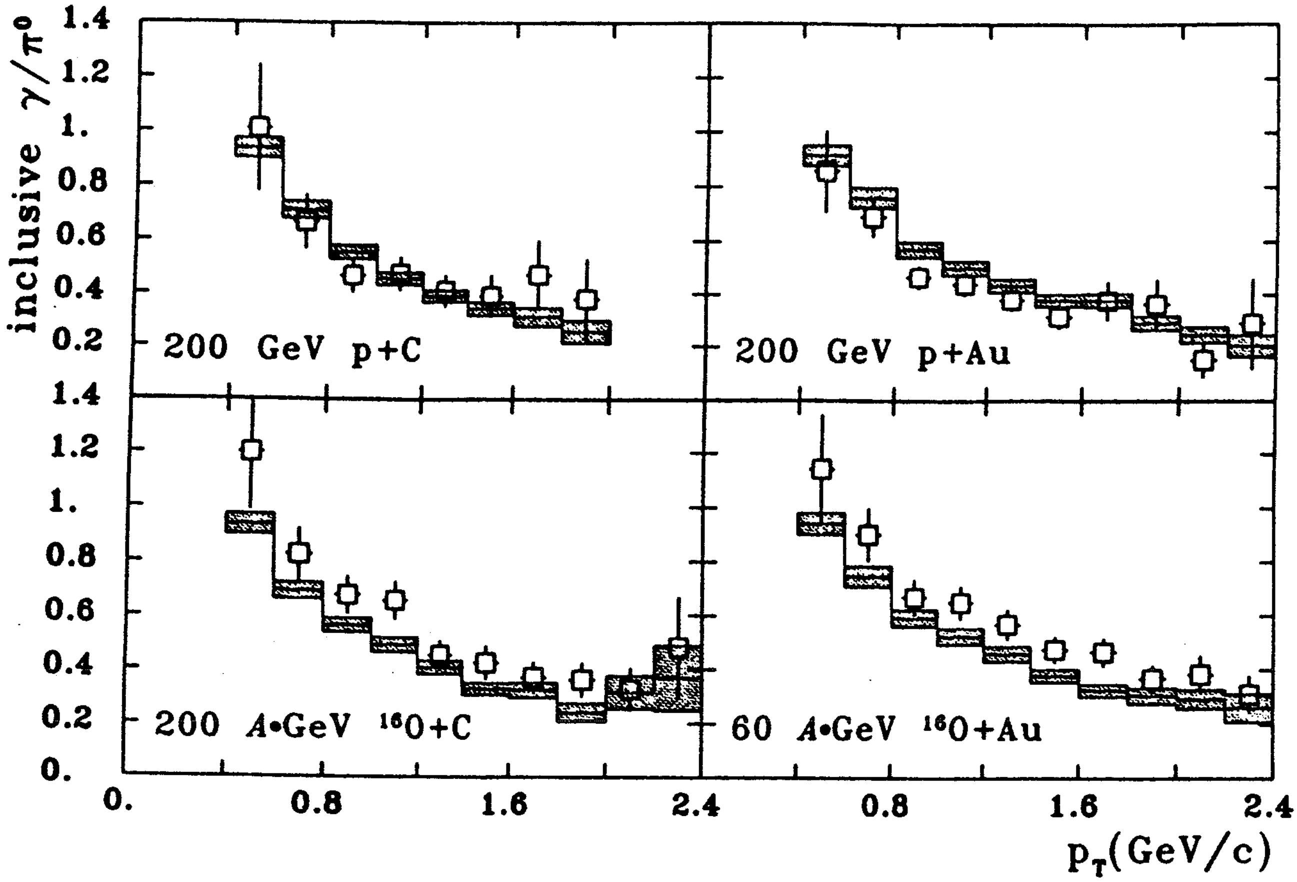

Figure 1.10: Photon spectrum observed by WA80. Squares are experimental points, histograms are calculations of hadronic background. The figure is taken from ref. [Alb91]

The study of direct photons is probably the only way to extract global information from the hot plasma zone, in analogy to the background radiation observed in the universe. Although most photons are undisturbed on their way from the reaction zone to the detectors, such measurements still have to cope with a severe background of photons produced by hadronic mechanisms. The most prominent sources of background photons are the decays of short-lived resonances (π^0, η^0, ρ^0 etc. $\rightarrow \gamma\gamma$), but also other hadron decays producing photons, along with misidentification of other neutral particles (n, K_L^0 etc.) must be taken into consideration.

Both the NA34 [Ake90] and the WA80 [Alb91] collaborations at CERN have made a careful analysis to try to eliminate the hadronic background from their observed photon spectra. The spectrum shown in figure 1.10, taken from WA80, shows that there is no significant difference between the observed spectrum and the background spectrum calculated using background sources only.

This negative result is confirmed by theoretical calculations [Ruu92]. These calculations suggest the signal to become more prominent at higher energies in future heavy ion colliders.

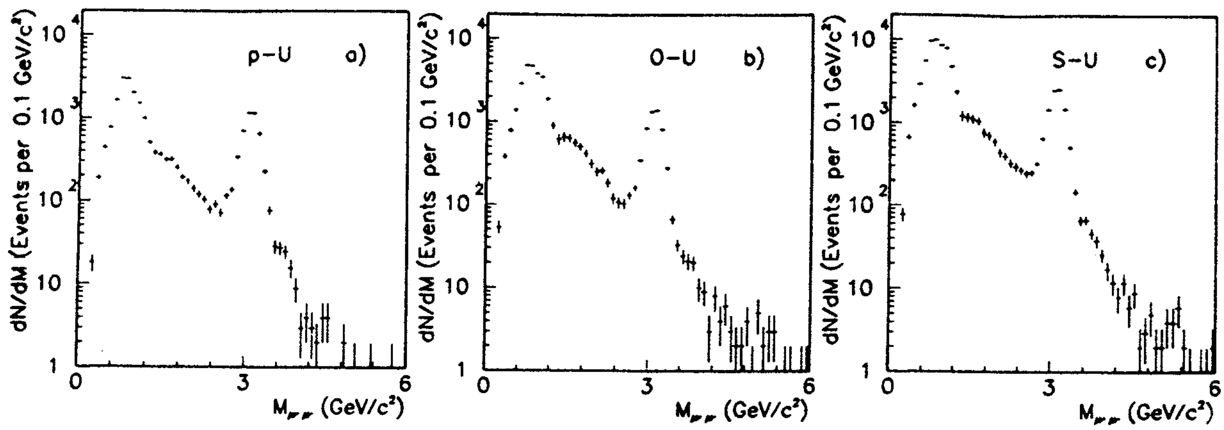

Figure 1.11: Dimuon spectrum measured by NA38. Figure taken from ref. [Bag91]

1.6.2 Specific signals

J/Ψ suppression

The J/Ψ meson is a bound state of a charmed and an anti-charmed quark ($c\bar{c}$). This particle can be produced by parton fusion, $q\bar{q} \rightarrow c\bar{c}, gg \rightarrow c\bar{c}$, once the incoming partons carry sufficient amounts of energy.

In a hadronic environment, the flux tube formed between the quarks in the $c\bar{c}$ pair would cause a J/Ψ meson to be produced. In a deconfined phase, the charmed quarks are allowed to move as free particles. At freeze-out, chances are small that there will be an anti-charmed quark in the vicinity of a given charmed quark, and the charmed quark will normally bind with a light antiquark of the appropriate colour, to produce a D meson.

Hence, one would expect a lower production rate of J/Ψ mesons when a quark gluon plasma is produced, compared to a normal hadronic reaction. This signal was first suggested by Matsui and Satz [Mat86].

The NA38 collaboration at CERN identifies the J/Ψ meson by its decay to $\mu^+\mu^-$ pairs. This branch accounts for 5.9% of the J/Ψ decays. Although there is a large background of $\mu^+\mu^-$ pairs, a peak in the invariant mass region of the J/Ψ is clearly visible, as shown in figure 1.11 [Bag91].

A suppression of the J/Ψ production in central collisions compared to peripheral collisions was observed by the NA38 collaboration at an early stage [Bus88]. This would indicate plasma production in the central events. Later theoretical work has shown that there exist several other mechanisms that can explain these data, most notably final state interactions between the J/Ψ and other hadrons [Ger92].

Strangeness enhancement

In a hadron gas, strangeness can only be formed inside hadrons containing strange quarks. An equal number of strange and anti-strange quarks must be distributed among these produced particles. The minimum energy required to produce such particles is 671 MeV, corresponding to the reaction p+n→ Λ^0+K^++n. In a quark gluon plasma a $s\bar{s}$ quark pair can be produced directly. This process requires a total energy of approximately 300

MeV. (The strange quark mass is close to 150 MeV.)

Lattice QCD calculations indicate a transition temperature from hadron gas to quark gluon plasma in the region 150-200 MeV. By thermal energy it should therefore be possible to produce a significant number of $s\bar{s}$ pairs by gluon interactions ($gg \rightarrow s\bar{s}$). This production mechanism is made even more favourable by the high number of light quarks (u and d) which originate from the incoming particles. Since all quarks are fermions, low-energy states of light quarks tend to be occupied, and Pauli blocking requires additional light quarks to carry a high excitation energy.

Since weak decays occur on a rather long time scale (at the order of 10^{-10}s), an excess of strange quarks produced in the reaction zone should remain present in the hadrons produced at freeze-out.

Several experiments have looked for such an enhanced strangeness production, both at Brookhaven (E802,E810) and CERN (NA34, NA35, NA36, WA85). The initial calculations [Koc86] indicated that the production of strange quarks should increase by a factor of 10 in quark gluon plasma events compared to normal hadron events. Most collaborations observe an enhancement about a factor of two.

Later calculations [Cle91] indicate that the observed enhancement of strangeness can also be explained by rescattering of hadrons in a hot and dense reaction zone.

As this thesis is based upon one of the experiments that investigate this signal, a more detailed discussion of both theoretical and experimental aspects of strangeness production can be found in the following chapters.

Exotica

If a yet unknown particle was formed when a quark gluon plasma hadronises, the observation of this particle would of course be the ultimate signal to prove an original plasma production. So far, no such particle is observed. There have been suggestions that the high amount of strange quarks that are expected to be present in the plasma could form novel kinds of matter, containing more than three quarks [Mul92] (strangelets).

The simplest such entity would be the H particle, with quark composition (uuddss). If this particle decays to two lambdas ($H \rightarrow \Lambda\Lambda$), it should be detectable in the experiments dedicated to the strangeness enhancement signal, among them WA85.

No experimental Hs are observed yet. It has even been suggested that the mass of the H might be lower than the mass of two lambdas, making the H rather long-lived. Such a low-mass H has also been proposed as a dark matter candidate, to explain the apparent lack of mass in the universe.

A low-mass or even stable H would be a very interesting observation, and could be a useful QGP signal. But it would probably be too optimistic to claim such new phenomena to be around the corner, and too pessimistic to write off the possibility to observe a plasma formation without them.

Chapter 2

Strangeness production

2.1 Introduction

The WA85, WA94 and WA97 experiments aim to measure production ratios of particles carrying increasing number of strange quarks. An enhanced production of strange quarks is believed to take place in a quark gluon plasma. As weak decays occur over a comparatively long time scale, these strange quarks must be present among the particles available in the final state. In this chapter strangeness in heavy ion collisions is discussed, both from a theoretical and an experimental point of view. The following chapters will go into further details on the above mentioned experiments.

2.2 Strangeness theory

The major arguments for strangeness enhancement as a signal for quark gluon plasma production is listed below:

Mass threshold: In a quark gluon plasma 300 MeV is required to produce a $s\bar{s}$ pair, compared to 670 MeV needed to produce $K\Lambda$ in a hadron gas.

Pauli blocking: Several u and d quarks from the projectile and target are present in the interaction zone. They force additional $q\bar{q}$ pairs to carry excitation energy.

Gluon abundance: A large amount of gluons are expected to be present in a quark gluon plasma. They can readily produce $q\bar{q}$ or $s\bar{s}$ pairs, to feed the mechanisms discussed above.

A broad overview of the theory of strangeness production in heavy ion collisions is given in [Koc86]. This reference gives production rates of $s\bar{s}$ pairs, based on a thermally equilibrated quark gluon plasma. This assumption should be justified, given the short life time of a possible QGP formed in a heavy ion collision (a few fm/c). Several authors [Mul92a] have investigated this assumption. Based on a requirement of an average of three collisions per particle to create a thermal system, a thermalisation time of around one fm/c is obtained, well below the expected life time of the plasma.

In addition to the thermal equilibrium, Koch, Müller and Rafelski [Koc86] assume chemical equilibrium between the three light quark flavours to be established in the plasma. They find the $s\bar{s}$ production rate to be dominated by gluon interactions ($gg \rightarrow s\bar{s}$). This process has a short equilibration time, at the order of 0.5 fm/c, well below the plasma life time. The chemical equilibration time of a hadron gas is expected to be 10-30 times longer [Egg91], which is probably longer than the life time of the hot region produced in current ion collisions.

As there are practically no strange quarks present before the collision, the abundance of strange quarks will increase until equilibrium is reached. The same argument goes for antiquarks. Strange antiquarks combine the merits of the two effects, and should be significantly enhanced in a plasma environment.

A chemically equilibrated QGP will contain about 30% strange quarks and antiquarks [Koc86]. In relativistic gases, each particle carries a fixed amount of entropy. When the plasma hadronise, particles consisting of several quarks will be formed. Intuitively this would cause the total particle number to drop, making the total entropy decrease. To avoid reduction of entropy, it is assumed that the necessary number of additional particles (mainly mesons) will be created by gluon fragmentation. About 15 % of the quarks produced by this mechanism will be $s\bar{s}$ pairs.

Altogether, an enhancement of the strangeness production in a quark gluon plasma by a factor of about 10 when compared to hadron gas mechanisms at the same temperatures, is predicted. The great majority of these strange quarks must be present in the final state.

A chemically equilibrated quark gluon plasma will contain a significant number of antiquarks. Hence, there will be a considerable probability that three antiquarks will be available to produce an antibaryon at the hadronisation stage. An increased production of antibaryons has been proposed as a plasma signal. With 30% of the antiquarks being strange, a large fraction of these antibaryons will carry strangeness. On the other hand, the production of strange antibaryons in a hadron gas is strongly suppressed due to its mass threshold. An enhanced production of strange antibaryons is therefore suggested as a particularly well suited signal for plasma formation.

2.3 BNL results

The Alternate Gradient Synchrotron, AGS, at Brookhaven National Laboratory (BNL) is able to accelerate oxygen and silicon ions to an energy of 14.6 GeV per nucleon. This corresponds to a beam rapidity of y=3.44. (A test run with gold ions was performed in 1992, physics results from real heavy ion reactions are foreseen in the next few years [Gon93].)

Two collaborations have measured strangeness production in the silicon programme, E802 and E810. The results of these experiments are discussed below.

2.3.1 E802 results

The E802 experiment is based on a magnetic spectrometer setup [Mia91], with particle identification done by a time-of-flight (TOF) counter. This works well at the energies in

Table 2.1: K/π ratios measured by E802

	p+Be	p+Au	Central Si+Au
K^+/π^+	7.8 ± 0.4 %	12.5 ± 0.6 %	18.2 ± 0.9 %
K^-/π^-	2.0 ± 0.2 %	2.8 ± 0.3 %	3.2 ± 0.3 %

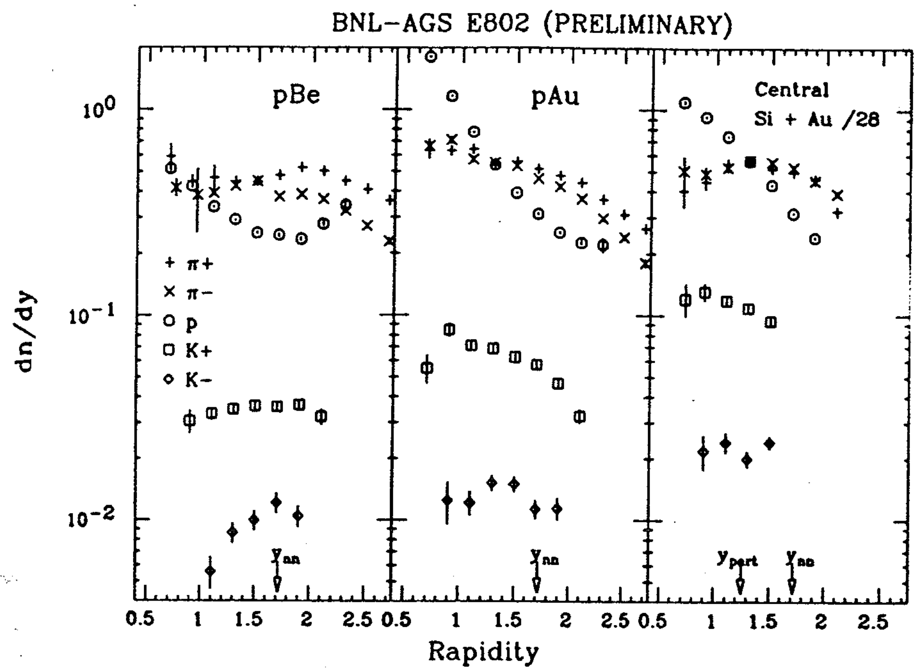

Figure 2.1: E802 rapidity distributions. Figure taken from [Mia91].

question, and E802 is able to measure pion, kaon and proton spectra in a rapidity region $0.6 < y < 2.4$.

The ion data taken from Si+Au interactions are compared to proton reference data, notably p+Be and p+Au. From pion and kaon spectra, integrated K/π ratios in the various reactions are extracted. The results are summarised in table 2.1 [Abb91].

The K^+/π^+ ratio shows a marked increase with increasing target and projectile mass. The result in ion collisions (central Si+Au) corresponds to an increased production of strange (anti)quarks by about a factor of two. The K^-/π^- show a less pronounced increase, about 50 %. The results in p+Be is compatible with earlier p+p results. The rapidity distributions are shown in figure 2.1. There is a significant difference between the K^+ and K^- spectra; K^+ peaks at low rapidity (target fragmentation region), whereas K^- peaks at central rapidity in p+Be interactions, and is practically flat for heavier projectiles and targets. This may indicate different production mechanisms for the two particle ratios, making the meaning of the direct comparison between them less obvious.

In a baryon rich plasma, the abundance of quarks will be much larger than the abundance of antiquarks. It will therefore be relatively easy for an $\bar{s}$ quark to combine with a u or d quark to form a K^+. There will be fewer light antiquarks present to form K^-s, thus strange quarks tend to hadronise as Λs, with a quark configuration of (uds) [Nag92].

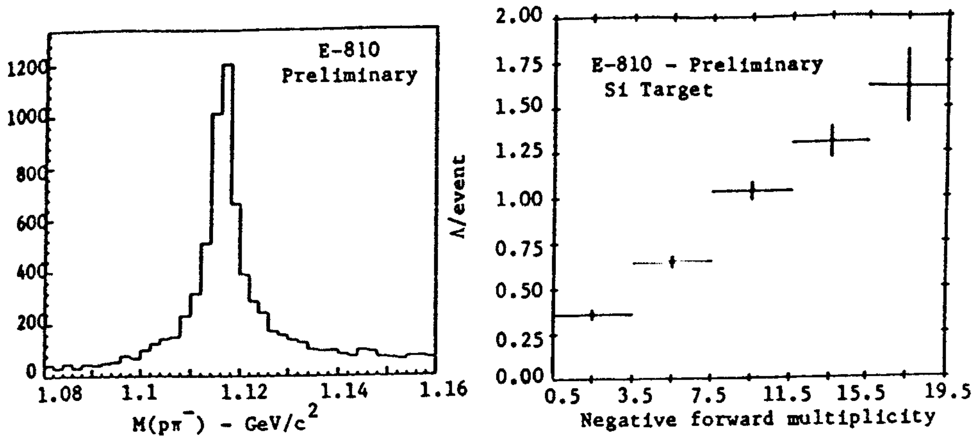

Figure 2.2: E810 Λ production. Figure taken from [Fol92]

2.3.2 E810 results

The E810 experiment at BNL is based on time projection chambers (TPCs) as tracking devices. The beam passes through the middle of the TPCs, giving a large acceptance, also for low-momentum particles. So far [Fol92, Eis92] K^0 and Λ production in Si+Si, Si+Cu, Si+Au and Si+Pb reactions are measured. No proton reference data are available. The Λ production rate in Si+Si reactions increases linearly with negative multiplicity (fig. 2.2). In other words, there is no net increase when going to more central collisions, as is observed in the NA35 data.

As no reference data are available, it is difficult to state whether E810 observe a strangeness enhancement or not. In ref. [Fol92] they compare their results to HIJET calculations, and find an increased Λ production of about a factor two, and a slightly lower increase in the K^0 production.

2.4 CERN results

The CERN Super Proton Synchrotron (SPS) was upgraded to allow for acceleration of heavy ions (up to sulphur) in the mid-eighties. At an early stage oxygen ions were accelerated to energies of 60 and 200 GeV per nucleon, later on all runs have been performed with 200 GeV·A sulphur beams. This gives a beam rapidity of y=6.

2.4.1 NA34 results

The NA34 (HELIOS) collaboration identifies particles with a time-of-flight counter. The emphasis is put on low-momentum particles originating from the target fragmentation region ($0.8< y <1.3$).

As can be seen in fig. 2.3, the K^+/π^+ ratio is enhanced by a factor of two in S+W compared to p+W data, whereas K^-/π^- is practically unchanged. The dotted lines show K/π ratios from pp experiments, extrapolated to the relevant y-p_t region.

The results agree very well with E802 data. This can be taken as an indication that the target fragmentation region at CERN corresponds well to the central rapidity region in AGS reactions. Both of these can be described as a baryon rich region of dense matter.

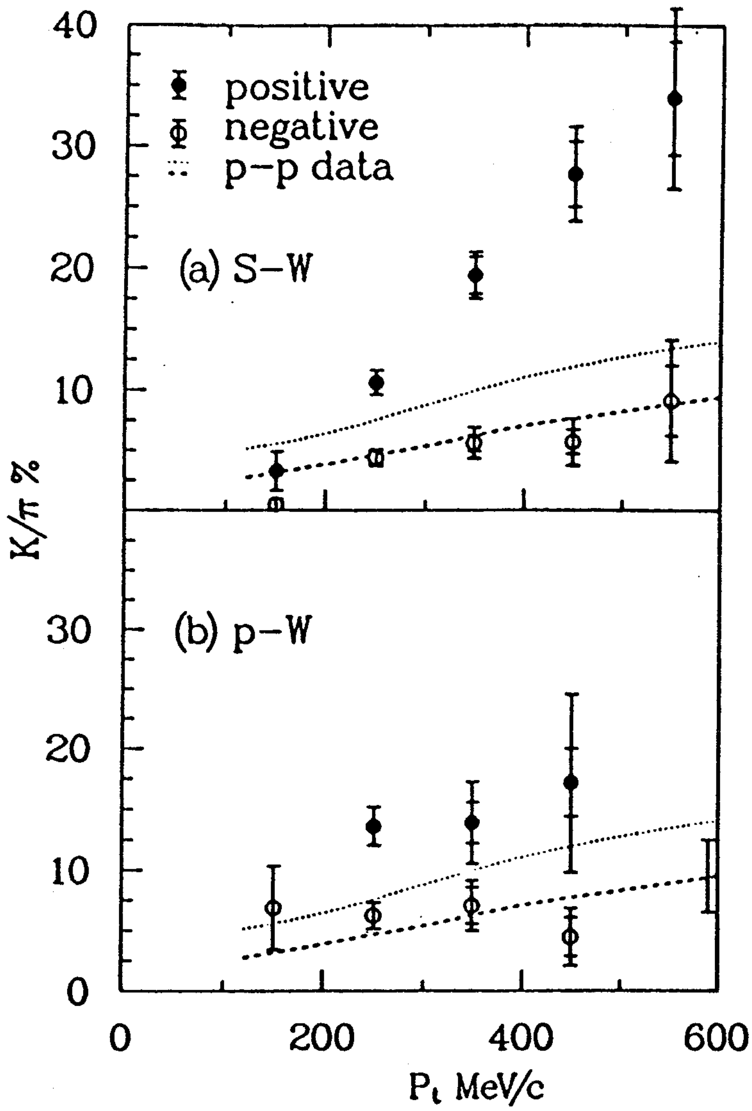

Figure 2.3: K/π ratios from NA34. Figure taken from ref. [vHe91]

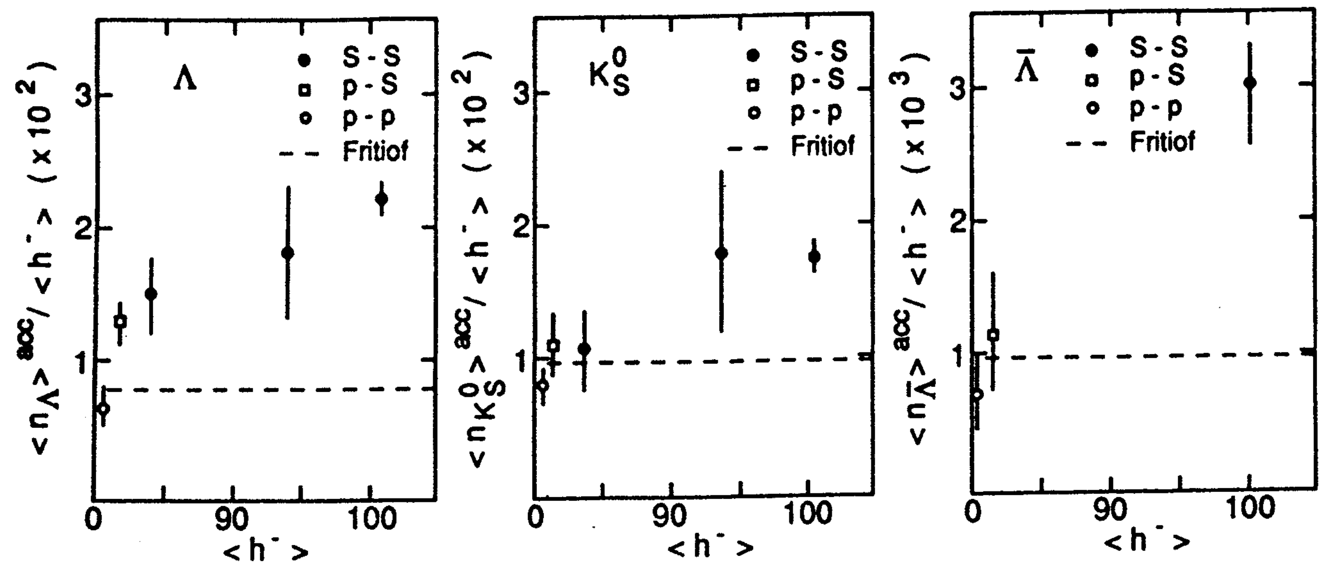

Figure 2.4: Neutral strange particle production measured by NA35. The figure is taken from [Sch92].

Both E802 and NA34 see a steeper slope in the K^+ p_t spectrum compared to the pion and K^- spectra. This corresponds to a higher temperature, and could indicate a different production mechanism for K^+s than for the more numerous pions.

2.4.2 NA35 results

The NA35 collaboration identifies outcoming particles in a streamer chamber. K^0_s, Λ and $\bar{\Lambda}$ are measured in 60 and 200 GeV·A O+Au reactions, along with p+Au reference data [Bam89]. Later on, mesurements of K^+ and K^- were also included in the 200 GeV·A S+S data [Sey92].

In the oxygen data, measured in the backward rapidity region (y~2), no increase in K^0 and $\bar{\Lambda}$ production is seen, but the number of Λs increases by a factor of two compared to a superposition of p+Au data.

In the S+S data, the acceptance region is 1< y <3, which correspond to most of the available phase space by reflection symmetry in the S+S system. (The centre of mass rapidity is y=3.) In this reaction an increase in the production rate of all the neutral strange particles in question is seen. The increase is strongest for $\bar{\Lambda}$s (about a factor of three). The Λ production rate increases already when going from p+p to p+S reactions, and for all particles there is an increase when going to more central collisions (higher negative multiplicities). The data are summarised in fig. 2.4.

The rapidity distribution of the $\bar{\Lambda}$s is rather sharply peaked at mid rapidity, the Λ rapdity distribution is much wider [Bam90]. This indicate that a significant fraction of the Λs are produced in the target and projectile region, whereas $\bar{\Lambda}$ production take place in the central hot and dense region.

The recent data on charged kaon production [Kow92] show an excess of K^+s compared to K^-s, compatible with the excess of Λs previously measured. This would indicate that the $s\bar{s}$ pairs find themselves in a baryon rich area, where the number of quarks to combine with is much larger than the number of available antiquarks. This process could be a trivial hadronic scattering (π+N $\rightarrow$ K+Λ), or it could be a baryon rich region of quark matter.

2.4.3 NA36 results

In the NA36 experiment decay of strange particles are investigated in a time projection chamber (TPC), located 1 cm above the ion beam [Gre92]. This setup gives a very large acceptance ($\sim 1 < y < 3.5$, $p_t > 0.3$ GeV/c), but also gives a very high particle multiplicity in the tracking device.

Results on neutral strange particle production are available, both from S+Pb reactions and reference p+Pb data. The rapidity distributions of the strange particles look rather different in the two reactions, as shown in figure 2.5. In ion reactions all distributions peak at mid rapidity, suggesting a production mechanism of a hot and dense central fireball. In the proton data, the $\overline{\Lambda}$ spectrum looks flat, whereas the other particle distributions peak in the target fragmentation region, suggesting hadron rescattering as their origin.

The NA36 apparatus should also be able to detect multistrange particles. A search for Ξ^-s and $\overline{\Xi}^-$s has been carried out, but results are not published yet [Jud92].

2.4.4 NA38 results

The NA38 experiment is designed to study muon pairs, in order to investigate the J/Ψ suppression, discussed in section 1.6.2.

If the enhanced production of strange particles observed by several experiments is due to an increased production of $s\bar{s}$ pairs in a quark matter, one would also expect an increased production of the ϕ meson, which has a dominant internal quark structure of ($s\bar{s}$).

The ϕ meson has a decay branch to K^+K^-, which in turn decays to $\mu\nu_\mu$ pairs. This decay channel is detectable in the NA38 setup.

Figure 2.6 shows an increased production of ϕs compared to ρ and ω mesons when going from p+U to O+U and S+U reactions, and the production does also increase when going from peripheral to central collisions.

The increased production of ϕs of about a factor of two seems compatible with what is observed in the other strangeness experiments.

A hadronic rescattering model proposed by Koch et al. [Koc90], can explain both the J/Ψ suppression and the ϕ enhancement. However, the observed ϕ enhancement corresponds to an upper limit of the model, a possible further increase when going to heavier projectiles would be a strong indication of formation of a quark gluon plasma.

2.4.5 WA85 results

The tracking device of the WA85 collaboration is seven wire chambers placed in the Omega magnet. The chambers are modified in such a way that only high p_t – mid-rapidity tracks are accepted. This reduces the number of observed tracks in each collision considerably,

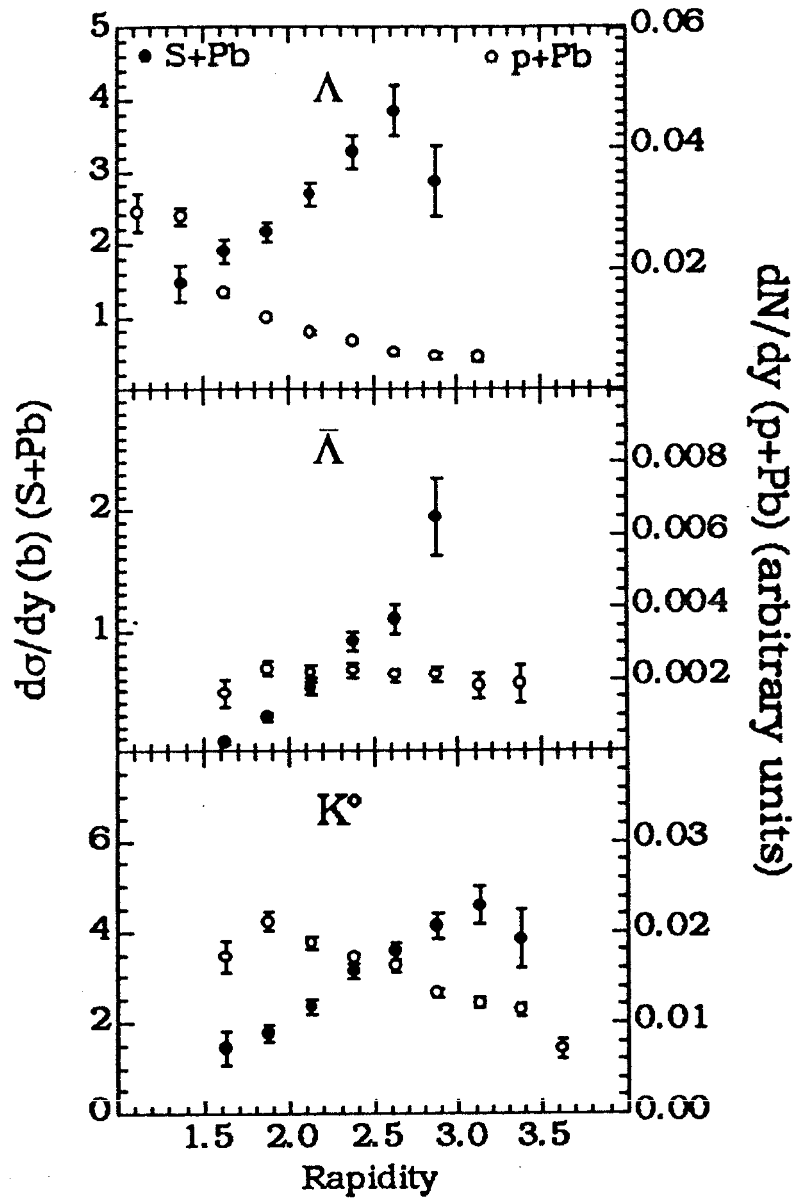

Figure 2.5: Rapidity distributions measured by NA36, taken from [Sak92]

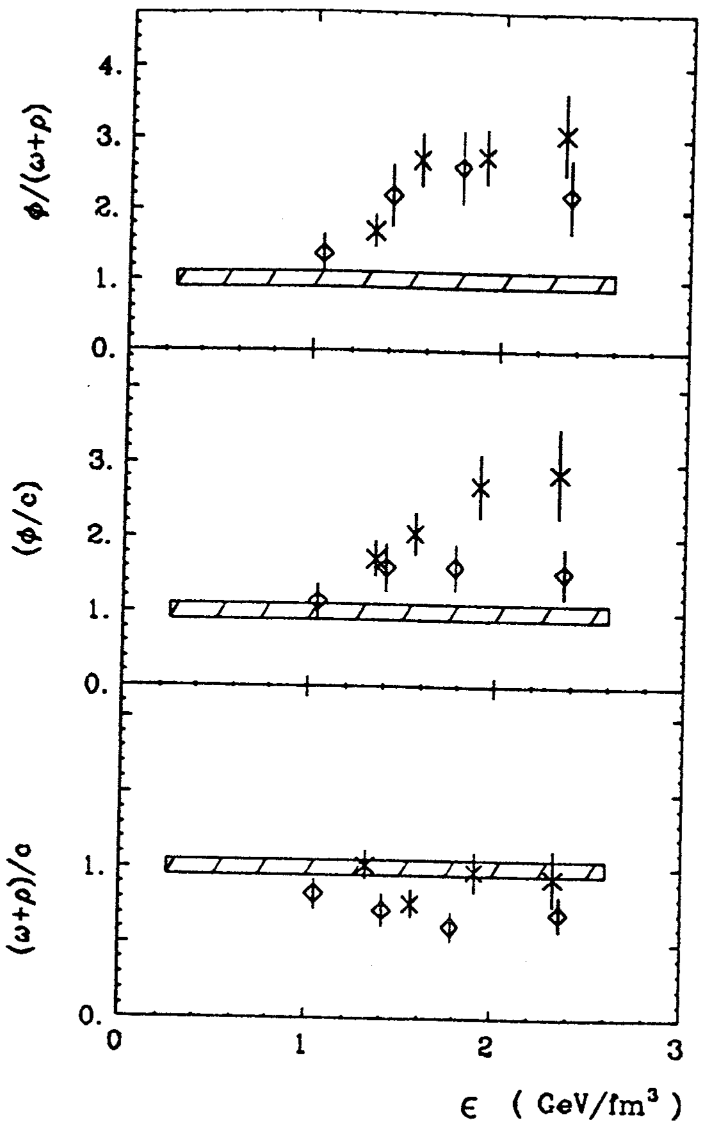

Figure 2.6: Ratios $\phi/(\rho+\omega)$, ϕ/(continuum) and $(\rho+\omega)$/(continuum) as function of energy density, as measured by NA38. Hatched area is p+U, diamonds are O+U and crosses are S+U. The figure is taken from ref. [Dra92]

on the other hand the acceptance region of the experiment is limited to 2.3< y <3.0, p_t>1GeV/c. Data are taken in S+W interactions along with reference p+W reactions.

Within the acceptance region, K^0_s, Λ, $\overline{\Lambda}$, $\Xi^-$and $\overline{\Xi^-}$ have been identified. The Λ and $\overline{\Lambda}$ production increase by a factor 1.7 when going from p+W to S+W reaction [Nar91], in general agreement with the other experiments.

So far, WA85 is the only collaboration who have published results on production of multistrange baryons. The observed $\overline{\Xi^-}/\overline{\Lambda}$ ratio appears very high. This may indicate a high degree of flavour equilibration, as discussed in the following section.

This thesis is based upon the work done in the WA85 collaboration and its successors. The WA85 experiment and results are discussed in detail in chapter 3.

2.5 Multistrange theory

The high $\overline{\Xi^-}$ production rate observed by WA85 has generated a considerable theoretical interest. In a naive picture one would expect it to be difficult to produce multistrange baryons in a hadron gas, as one would have to produce two strange (anti)quarks in the collisions, alternatively a strange baryon would have to undergo a second strangeness-producing collision. In a plasma containing a high number of $s\bar{s}$ quark pairs, it seems easier to group two (anti)strange quarks together with a light (anti)quark to form an (anti)baryon.

Several attempts have been made to study this process in more detail. H. Sorge and collaborators [Sor92] have extended their microscopic collision model RQMD to include 'coloured ropes', an extended region carrying colour charge. This model can describe the NA35 Λ production, but has so far not been applied to the WA85 data.

Another approach is given by hydrodynamic flow models. Csernai et al. [Cse92] have studied a two-component flow model, consisting of light and strange quarks as the two components. Zimanyi et al. [Zim92] investigate the flavour aspects of the hadronisation phase transition. Neither of these models have produced results directly comparable to experimental data yet.

J.Rafelski has published some considerations based on a completely equilibrated plasma approach [Raf91]. With these assumptions, particle ratios are given by the chemical fugacities of the quark flavours in question. The chemical fugacity, λ, is given by the chemical potential and the temperature by $\lambda = e^{\mu/T}$, where μ is the chemical potential. The chemical fugacity for antiquarks is given as the inverse of the fugacity for quarks. Furthermore up and down quarks are assumed to have the same chemical potential, giving the relevant variables $\lambda_q, \lambda_q^{-1}, \lambda_s$ and λ_s^{-1}.

The observed production ratios can then be given as

$$R_{\Xi} = \frac{\overline{\Xi^-}}{\Xi^-} = \frac{\lambda_q^{-1}\lambda_s^{-2}}{\lambda_q \lambda_s^2} \tag{2.1}$$

$$R_{\Lambda} = \frac{\overline{\Lambda}}{\Lambda} = \frac{\lambda_q^{-2}\lambda_s^{-1}}{\lambda_q^2 \lambda_s} \tag{2.2}$$

and finally

$$\frac{\overline{\Xi^-}}{\overline{\Lambda}} = \frac{\lambda_q^{-1}\lambda_s^{-2}}{\lambda_q^{-2}\lambda_s^{-1}} = \frac{\lambda_s^{-1}}{\lambda_q^{-1}} \tag{2.3}$$

All these ratios are measured experimentally by WA85. As a final point, the ratio $\overline{\Lambda}/\overline{p}$ turns out to be the same as $\overline{\Xi^-}/\overline{\Lambda}$. Hence, this ratio can be predicted, and hopefully compared to forthcoming WA94 data.

Elaborating these formulae further, Rafelski is able explain the WA85 data by assuming 30% fully equilibrated plasma in the reaction zone [Raf91].

This approach is based on several assumptions, which are not obviously justified. First, all strangeness observed in the reaction is assumed to come from the plasma phase, undisturbed by the hadronisation phase transition and subsequent rescatterings. Furthermore, the assumption of complete equilibration may not be valid.

Chapter 3

The WA85 Experiment

The WA85 experiment is designed to investigate strangeness production in the high p_t–mid-rapidity region. Within this region, different strange particles can be identified. So far, K^0, Λ, Ξ^- and their antiparticles are seen. Only very central collisions are triggered. This highly-specific setup complements the wide range of more general purpose facilities discussed in the previous chapter, and the collaboration aims to study specific signals of dense matter production.

3.1 Data taking

WA85 uses the heavy ion beam available in the CERN SPS accelerator. All ion data are taken with a sulphur beam, with an energy of 200 GeV per nucleon. The first batch of data was taken in 1987. The ten million triggers then taken are now fully analysed, and the results are published [Aba90, Aba91, Aba91a]. Most of the discussion in this chapter is based upon these data.

Proton reference data were taken in 1988. These are also fully analysed, and the key results are published along with the 1987 ion data.

The most interesting result obtained from the WA85 data (the $\overline{\Xi^-}/\overline{\Lambda}$ ratio), suffers from low statistics. Another round of data taking was therefore carried out in 1990. Then 90 million triggers of ion data and 110 million triggers of proton data were recorded on tape. The production part of the analysis of these data is completed, but the final physics analysis is still in progress.

The WA85 data taking is now completed. The experimental program is carried on by the WA94 collaboration, which will be discussed in the next chapter.

3.2 Apparatus

3.2.1 The Omega Spectrometer

The WA85 experiment is carried out in the Ω' spectrometer [1] [Beu84], which is a general purpose facility located in the West experimental area of the CERN SPS. The Ω magnet

[1] The old Ω spectrometer was renamed Ω' when it was upgraded and moved to a new position in the West Area. Its constituents (magnet, coordinate system etc.) are still conveniently labeled Ω.

consists of two Helmholtz coils, which generate a close to uniform magnetic field of 1.8 Tesla. Inside the magnet there is an area of about six square metres, where various detectors can be placed.

Most experimental positions are given in the Ω coordinate system. This system has its origo in the centre of the Ω magnet, close to the beam height. The downstream beam direction is defined as the positive X axis and thc positive Z direction is upwards, towards the roof. The system is right-handed, with the Y axis along the floor (positive Y direction towards the Omega counting rooms).

3.2.2 Wire Chambers

The Omega facility is equipped with a number of general purpose multiwire proportional chambers. Seven of these chambers, known as the 'A chambers', are used as the WA85 tracking device. High energy sulphur collisions may produce thousands of tracks, which by no means can be identified in the wire chambers. The A chambers are therefore modified such that only a few tracks per event are accepted. The principle of this modification is known as the 'Butterfly geometry', and will be discussed later.

Each of the seven A chambers consists of three wire planes, separated by graphite-painted cathodes. The wires in these three planes, known as U, V and Y, have different directions. The Y wires are vertical, so the number of the hit wire relates directly to the Y coordinate. The U and V wires are inclined at $+10.14^o$ and -10.14^o to the vertical respectively. Three wire hits are sufficient to obtain one space point. The resolution in the horisontal (Y) direction is better than the resolution in the vertical (Z) direction. This is desirable, as the magnetic field bends the particles horisontally, whereas the tracks are straight in the Z direction.

Each wire plane contains 752 anode wires, with an internal spacing of 2 mm. The A1 chamber is positioned at X=90 cm, the most distant chamber (A7) is placed at X=240 cm.

Four 'butterflied' lever arm chambers, marked MY1-4 in figure 3.1, are placed outside the magnetic field. Each chamber consists of 786 vertical (Y) wires with a 4 mm pitch. They are placed at X=312, 315, 427 and 430 cm, and are used to improve the momentum resolution of the tracks reconstructed in the A chambers.

3.2.3 Other detectors

The complete detector setup used by WA85 in the 1987 run is shown in figure 3.1. In addition to the tracking device, there is a number of other counters, mainly used for triggering purposes. Scintillator counters are placed at the positions labeled by S, V and $\check{C}$ in the figure.

A thin tungsten target is placed at X=–140 cm in the Omega coordinate system. In the 1987 sulphur run, the target thickness was 200 μm (0.5% interaction length), in the 1990 it was replaced by a 500 μm target (1.2% interaction length) in order to increase the event rate.

Two silicon microstrip arrays mounted 15 cm downstream of the target, measure the track multiplicity. Each array has a sensitive area of 2.5×2.5 cm^2. The two arrays are mounted above and below the beam respectively. They cover a pseudorapidity region

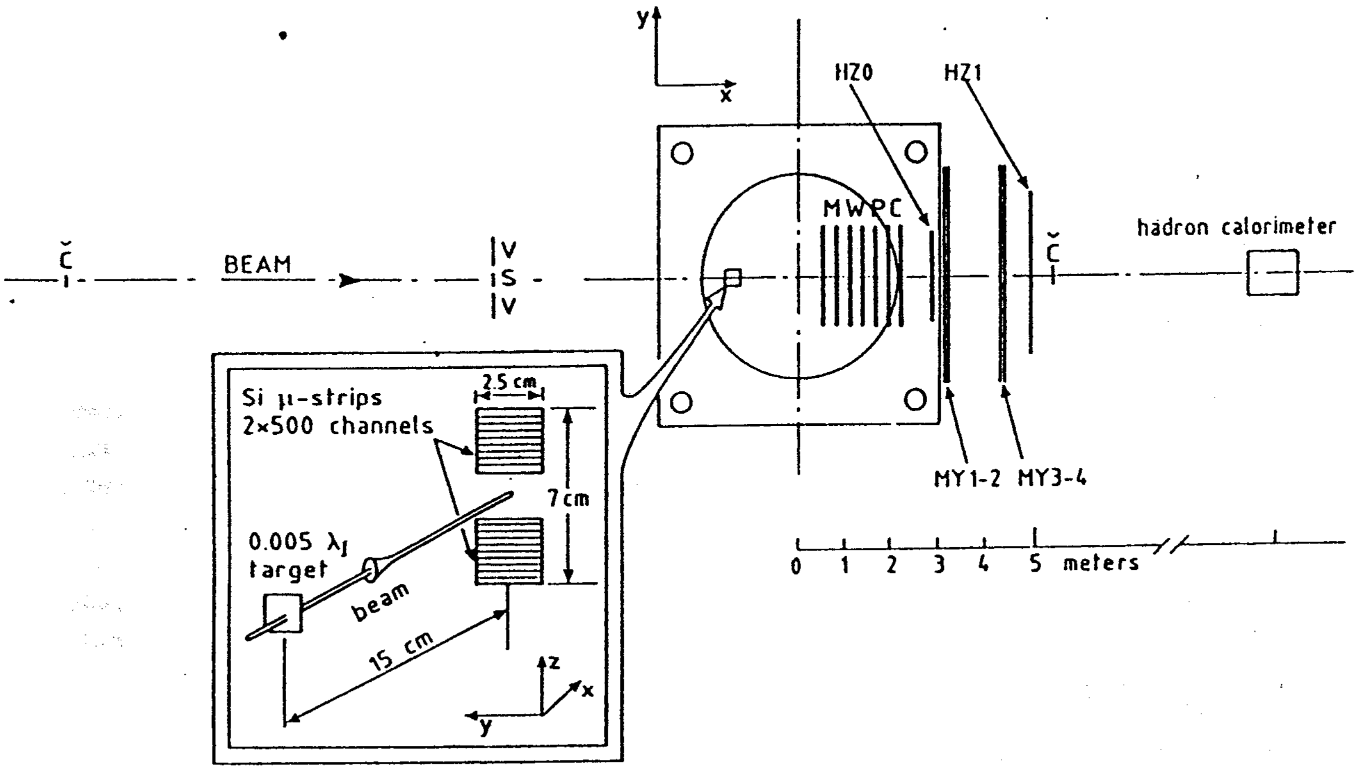

Figure 3.1: WA85 setup for 1987 run

of 2< η <3.4. A simulation study has shown [Nar91] the microstrip multiplicity to be proportional to the total rapidity density.

Two scintillator hodoscopes with a butterfly geometry are mounted behind the A chambers. These are labeled HZ0 and HZ1 in figure 3.1, and are used in the trigger to ensure that at least one track passes through the chambers.

Finally, a hadron calorimeter is placed at X=25 m in the Omega coordinate system. This is used as a veto counter, as the trigger logic required a low energy deposit in the forward direction. At the same time it works as a beam dump.

3.2.4 The Čerenkov detector C1

The setup of the 1990 run is shown in figure 3.2. In addition to the detectors used in the 1987 run, a threshold Čerenkov is added 13 m downstreams. The Čerenkov, labeled C1 in figure 3.2, is placed to one side of the beam axis, and lifted so that only high p_t particles can reach it. The detector is filled with freon 12, giving threshold momenta at 3.1 GeV/c, 10.8 GeV/c and 20.5 GeV/c for pions, kaons and protons respectively.

Scintillator hodoscopes, labeled HY1 and HY2 in figure 3.2, are mounted in front of and behind the Čerenkov. These hodoscopes are used to identify particles passing through C1.

If a particle in the momentum range 11-20 GeV/c is a pion or kaon, it will produce a signal in C1. Protons and antiprotons will not be seen in the detector, but they will leave traces in the two hodoscopes in front of and behind the Čerenkov. Thus, it should be possible to identify protons and antiprotons. (The magnetic field was reversed once during the run period, to allow particles of the opposite polarity to reach the Čerenkov.)

In the analysis phase, it turned out to be too much noise in the Čerenkov to extract a reliable signal.

3.3 The trigger

The trigger logic is designed to select central collisions only. The first part of the logic ensures there is a clean and well aligned beam. A signal is required in the beam counters, labeled S and the upstream Č in figure 3.1. The veto counter labeled V is a scintillator with a small hole in the centre to let the beam pass through. There should be no signal in this counter.

The second part of the trigger logic ensures that a central collision has taken place. A minimum multiplicity of 6 hits is required in each microstrip array, there should be no signal in the downstream Č (if there is a central interaction in the target, there should be no ions downstream) and there should be a low energy deposit in the forward calorimeter.

The third trigger component selects useful events in the detector setup. All further analysis is based on the tracks in the A chambers, and a signal in the HZ hodoscopes is required to ensure that at least one charged particle has passed through the sensitive region of the chambers. In the 1987 run at least two hits in HZ1 were required, in the 1990 run at least one correlated hit in HZ0 and HZ1 was demanded.

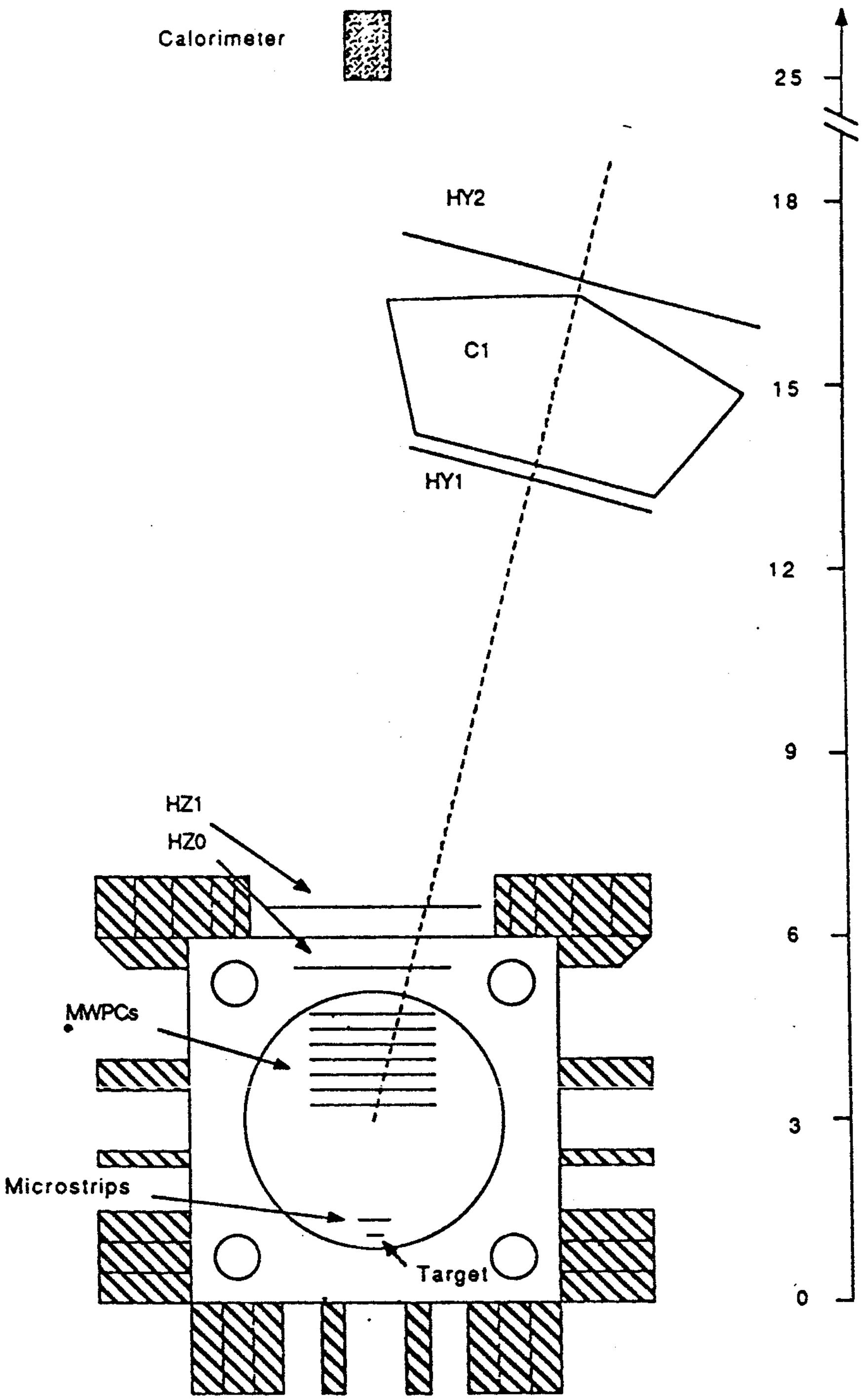

Figure 3.2: WA85 setup for the 1990 run.

3.4 The Butterfly Geometry

A central sulphur-tungsten interaction may produce several hundreds of charged particles. Such multiplicities cannot be handled by a small number of multiwire proportional chambers. WA85 has opted to study the high p_t–central rapidity zone only. There are only a few tracks per event in this region, and the detectors are modified to be insensitive to all the other tracks produced in the reaction.

The principle of this modification is shown in figure 3.3. Tracks with a given momentum will sweep out a cone as the direction of the transverse component of the momentum varies (fig. 3.3 a). In any YZ plane, as set up by the chambers, this cone will be seen as a circle. If the transverse momentum component is kept constant and the longitudinal component is decreased, the radius of the circle increases, as shown by the dotted lines in fig. 3.3 b and c. When the magnetic field is turned on, the track with the smaller longitudinal momentum (and larger circle) gets a larger horisontal displacement than the track with the larger p_l(dotted line in fig. 3.3d). Hence, the tracks with a p_t smaller than some $p_{t\min}$, will be confined to the non-shaded regions of fig. 3.3e.

The A chambers are made insensitive in the relevant regions by removing graphite paint on the cathode planes [Beu86]. In the WA85 setup, only the upper part of the shaded region of fig. 3.3e is kept sensitive. The shape and the size of the sensitive region varies from chamber to chamber, to make the geometrical acceptance similar for all planes.

The average number of tracks per event is 7.5 in sulphur-tungsten data. A "typical" event from the WA85 1987 data, with 7 reconstructed tracks, is shown in figure 3.4. As can be seen from the figure, the number of tracks is managable, and there are not too many background hits in the chambers.

3.5 Track reconstruction

A general track reconstruction program named TRIDENT [Las79, Las80] is developed for the Ω facility. A special version of this program, adapted to the experimental layout, is used by WA85. This program reads wire hits from the raw data tapes. Then elliptic tracks are fitted in the Y projection only (which is the bend direction of the magnetic field). Finally the possible Y tracks are compared to track candidates in the U and V planes, to obtain a complete three-dimensional track.

Once the tracks are found, a three-dimensional fit is performed to obtain the optimal track parameters. These parameters are written to the output file, along with the original raw data.

Each raw data tape contains about 180 Mbytes of data. TRIDENT processing of one such tape consumes about ten hours of IBM 3090 processing time. In the 1990 run, 700 raw data tapes were recorded.

The various strange particles are detected by their decay patterns. We identify Λs by the weak decay $\Lambda \rightarrow p + \pi^-$ and K^0s by $K^0 \rightarrow \pi^+ + \pi^-$. These branches correspond to 64% and 69% of the total decays respectively. Experimentally such decays can be detected by finding track pairs that intersect at a position well separated from the target.

The TRIDENT output is passed through another program, named STRIPV0, that searches for all possible charged tracks that cross each other. The distance of closest

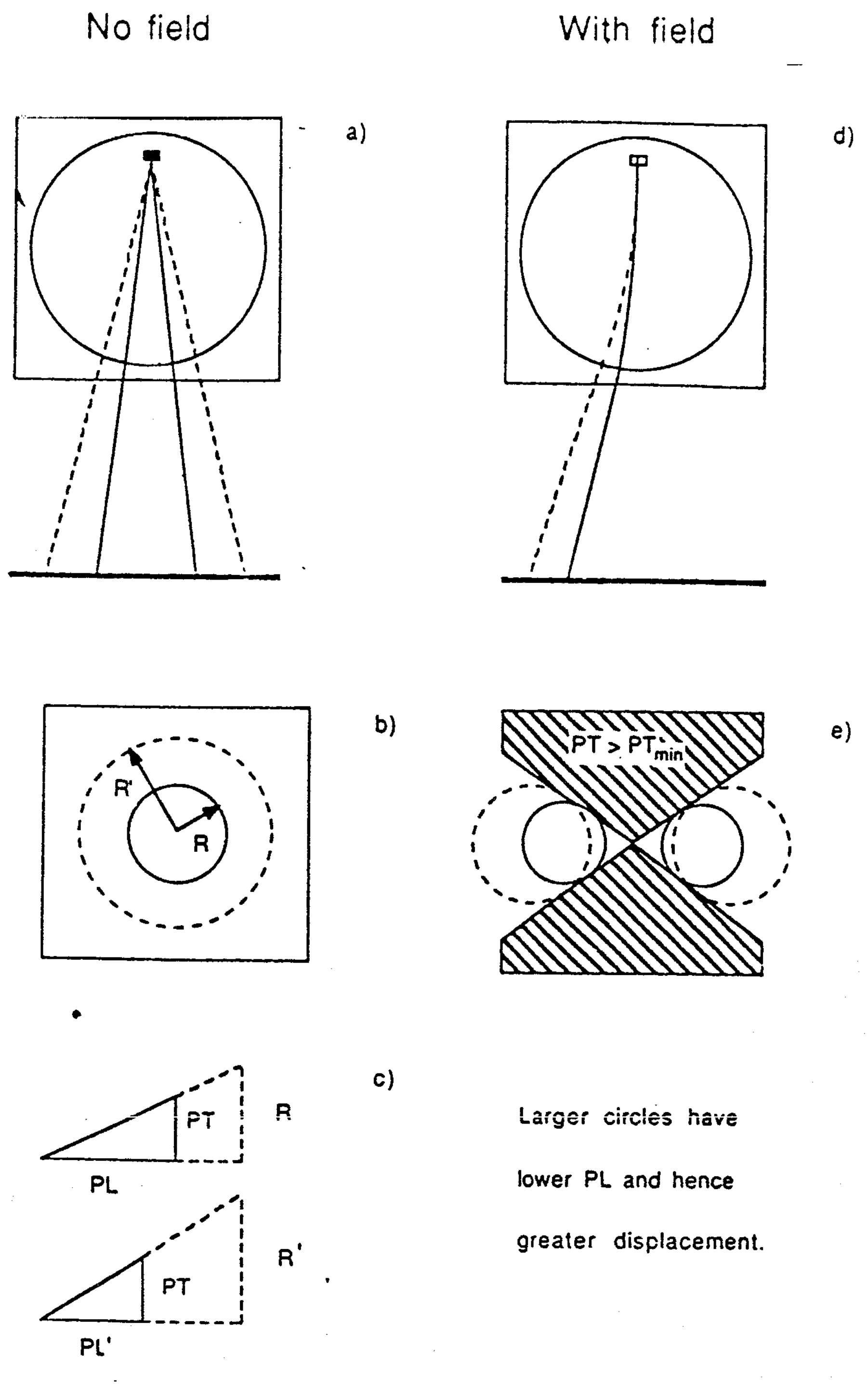

Figure 3.3: The butterfly principle

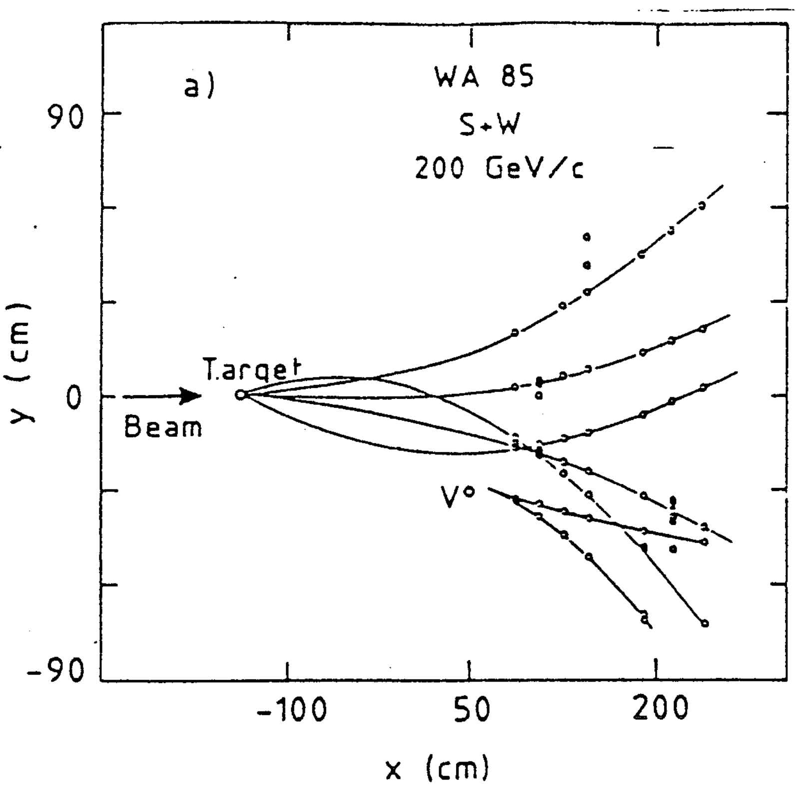

Figure 3.4: A fully reconstructed WA85 1987 event

approach is calculated for any pair of tracks related to a positive and a negative particle. If this distance is greater than 2 cm, the pair is rejected. Furthermore, the position of the V^0 vertex is required to lie in the range -40 cm<X<90 cm. The upper limit is the position of the first chamber, the lower limit is decided by acceptance considerations. Finally, a cut is made on the transverse momentum of the decay tracks with respect to the momentum of the V^0. This quantity, q_t, is required to be less than 0.4 GeV/c. Real V^0s have a q_t less than 0.2 GeV/c.

Track pairs that fulfill all the requirements listed above, are written to a special Data Summary Tape (DST) of V^0 candidates. In the final step of analysis, the V^0 candidates are subjected to various cuts, corresponding to different physical particles. These cuts are different for each of the strange particles in question, and will be discussed below.

3.6 Λ reconstruction

The DST of V^0 candidates produced by STRIPV0 is passed through the ANALYZ90 program to identify lamdbas and anti-lambdas. A number of cuts are made in order to make a proper identification. The cuts are discussed in detail after the short summary given below:

1. The distance of closest approach between the two decay track candidates is required to be < 1 cm.
2. Each track is required to have at least four space points from the chambers. (One space point is obtained by a combination of Y, U and V wire hits.)

3. Both decay tracks are required to trace through the sensitive region of all the seven chambers (although we don't require all of them to fire).
4. The X coordinate of the decay vertex is in the range $0 < X < 90$ cm.
5. The angle between the V^0 trajectory and a line coming from the target is less than 0.75°.
6. The Podolanski-Armenteros parameters $|\alpha| > 0.45$ and $q_t > 0.01$ GeV/c. (See discussion below.)
7. The decay tracks miss the target, $|\Delta Y| > 1.8$ cm for pions and $|\Delta Y| > 0.8$ cm for protons.
8. The rapidity and transverse momentum are within the defined acceptance region, see figure 3.7.
9. The effective mass is within $m_\Lambda \pm 25$ MeV/c^2.

The tightened cut on the distance of closest approach of the decay tracks compared to STRIPV0, was decided upon after a Monte Carlo study [Eva92] had shown that the background would be reduced while not many lambdas get lost this way.

A minimum number of hits per track is necessary to make a reliable reconstruction, and to obtain the momentum of the particles in question.

The requirement of having all tracks trace all the chambers is introduced to make accurate acceptance calculations possible.

A Monte Carlo distribution of the X vertex postion of Λs whose decay tracks trace all the seven chambers is shown in figure 3.5. The number of such lambdas decreases rapidly with decreasing X. Background tracks which cross, and thereby produce fake V^0s, tend to come from the target. The number of such V^0s increase with decreasing X. The tightened cut at X=0 cm was introduced to reduce the background in the Λ sample.

The decay tracks themselves are required not to point to the target. By a geometrical consideration it can be shown that the maximal distance between the two possible crossing points of the V^0 track trajectories is 40 cm for lambdas. Since the Λ is required to decay at least 140 cm from the target, one can safely require a minimum separation from the target in the bend direction, in our case 1.8 cm for pions and 0.8 cm for protons. The lambda itself, however, should come from the target, and the angle of deviation is required to be less than 0.75°.

The V^0 candidates can be identified by their appearance in the Podolanski-Armenteros plot [Pod54]. The three-momenta of the decay particles are decomposed into components parallell and transverse to the V^0 direction of motion. The longitudinal momentum component of the positive decay particle is labeled q_l^+; the negative decay particle has momentum component q_l^-. The transverse momentum component is defined as q_t.

The Podolanski-Armenteros plot is a scatter plot of the transverse momentum component q_t versus the variable α, defined by

$$\alpha = \frac{q_l^+ - q_l^-}{q_l^+ + q_l^-} \tag{3.1}$$

A Podolanski-Armenteros plot from the 1987 data is shown in figure 3.6. The kinematically allowed region for the different particles corresponds to ellipses in this plot. The ellipses for K^0s and $\Lambda/\overline{\Lambda}$ overlap in some regions, but some unambiguous areas remain.

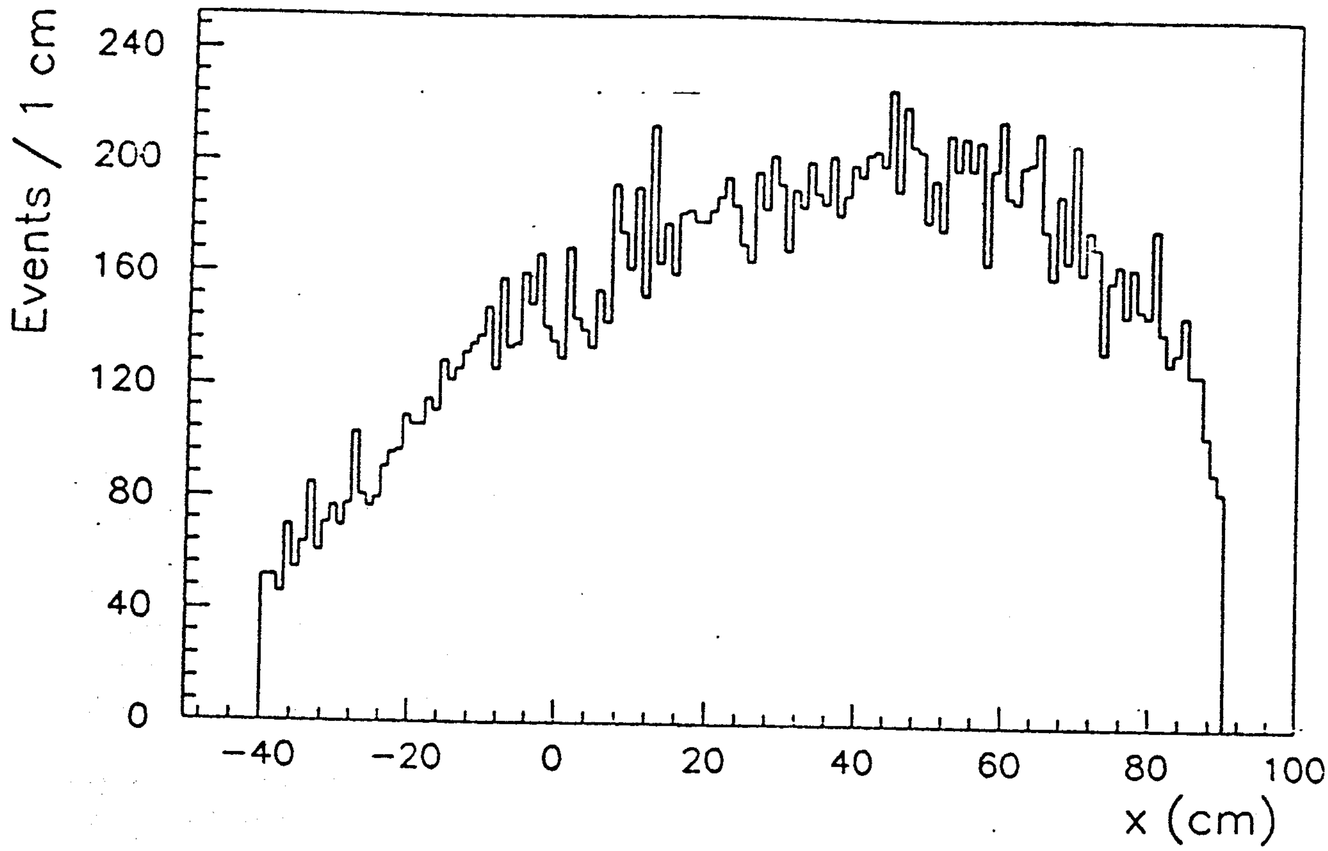

Figure 3.5: X position of decay vertices of Monte Carlo lamdas.

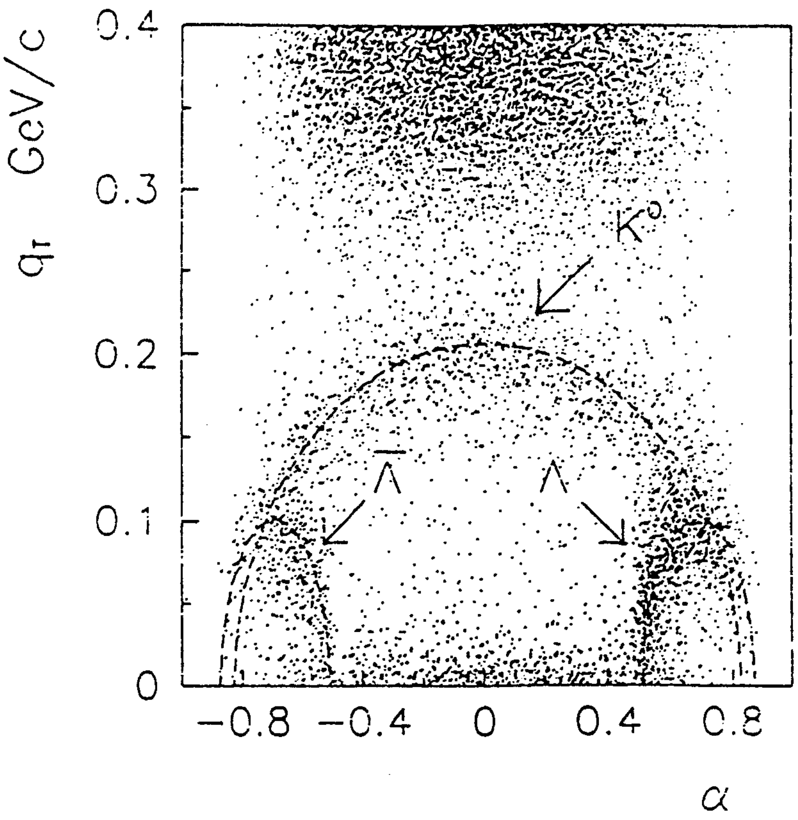

Figure 3.6: Podolanski-Armenteros plot for WA85 1987 data

There is a clear accumulation of points around the ellipses coresponding to K^0, Λ and $\overline{\Lambda}$. Close to these bands the background is low. The high number of points in the upper part of the figure corresponds to fake V^0s produced by crossing tracks coming from the target. The accumulation of points close to the α axis corresponds to gamma conversions. To eliminate these sources of background, cuts on q_t (0.01 GeV/c < q_t <0.4 GeV/c) are imposed. The cut on α ($|\alpha|$ > 0.45) includes the full kinematically allowed regions for Λs, while most of the background is rejected.

The Butterfly geometry of the tracking device makes the geometric acceptance of the experiment limited. Figure 3.7 shows the region where the acceptance is considered good. Only particles falling within this region are included in the analysis.

The effect of the cuts can be illustrated by the effective mass plots shown in figure 3.8. In picture a), cuts 1-4 have been applied, in b) cuts 1-5, in c) cuts 1-6 and in d) cuts 1-8. Even when only the basic geometric cuts are used (picture *a)*), a peak can be seen at the lamda mass, but the background is large. The Armenteros plot variable cuts eliminate most of the background, and the signal is rather clean even before the final mass cut (picture *d)*).

3.7 Ξ reconstruction

Ξ^- and $\overline{\Xi^-}$ particles are identified by their decay $\Xi^- \rightarrow \Lambda + \pi^-$. The STRIPV0 DST is passed through the WA85XI program. This program looks for single tracks that intersect the V^0 line of flight. Again a number of cuts are imposed on the Ξ^- candidates.

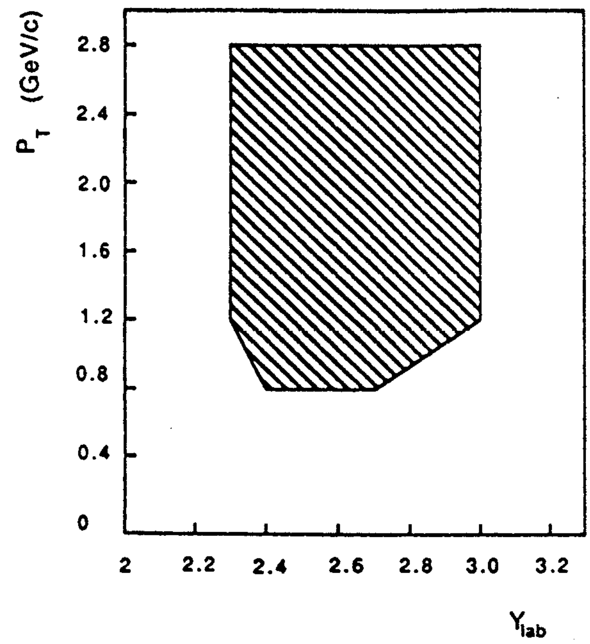

Figure 3.7: WA85 acceptance region

Cuts applied on the V^0 of the Ξ^- candidate:

1. The distance of closest approach between the two decay tracks is < 1.6 cm.
2. Each decay track has at least four space points.
3. Each track traces through the sensitive region of the first four chambers.
4. The X coordinate of the V^0 vertex is in the range $-15 < X < 90$ cm.
5. $|\alpha| > 0.40$ and $q_t < 0.12$ GeV/c.
6. The effective mass is within $m_\Lambda \pm 40$ MeV/c^2.

The cuts applied on the Ξ^- candidate itself are:

1. The distance of closest approach between the V^0 and the pion track is < 1.6 cm.
2. The pion track has at least four space points.
3. The pion track trace through the sensitive region of the first four chambers.
4. The X coordinate of the Ξ^- decay vertex is in the range $-40 < X < 90$ cm.
5. The Ξ^- vertex is before the V^0 vertex.
6. The Ξ^- trace back to the target, $|\Delta Y_\Xi| < 2$ cm.
7. The pion track miss the target, $|\Delta Y_\pi| > 11$ cm.
8. Acceptance region for Ξ^-s: $2.3 < y < 3.0$, $1.1 < p_t < 3.3$ GeV/c.
9. The effectice mass is within $m_\Xi \pm 50$ MeV/c^2.

These cuts are rather similar to the ones used for Λs, discussed in the previous section. The Ξ^-s have shorter life times than Λs, and Monte Carlo studies confirm that the lower limit on the vertex position should be closer to the target than is the case for lambdas.

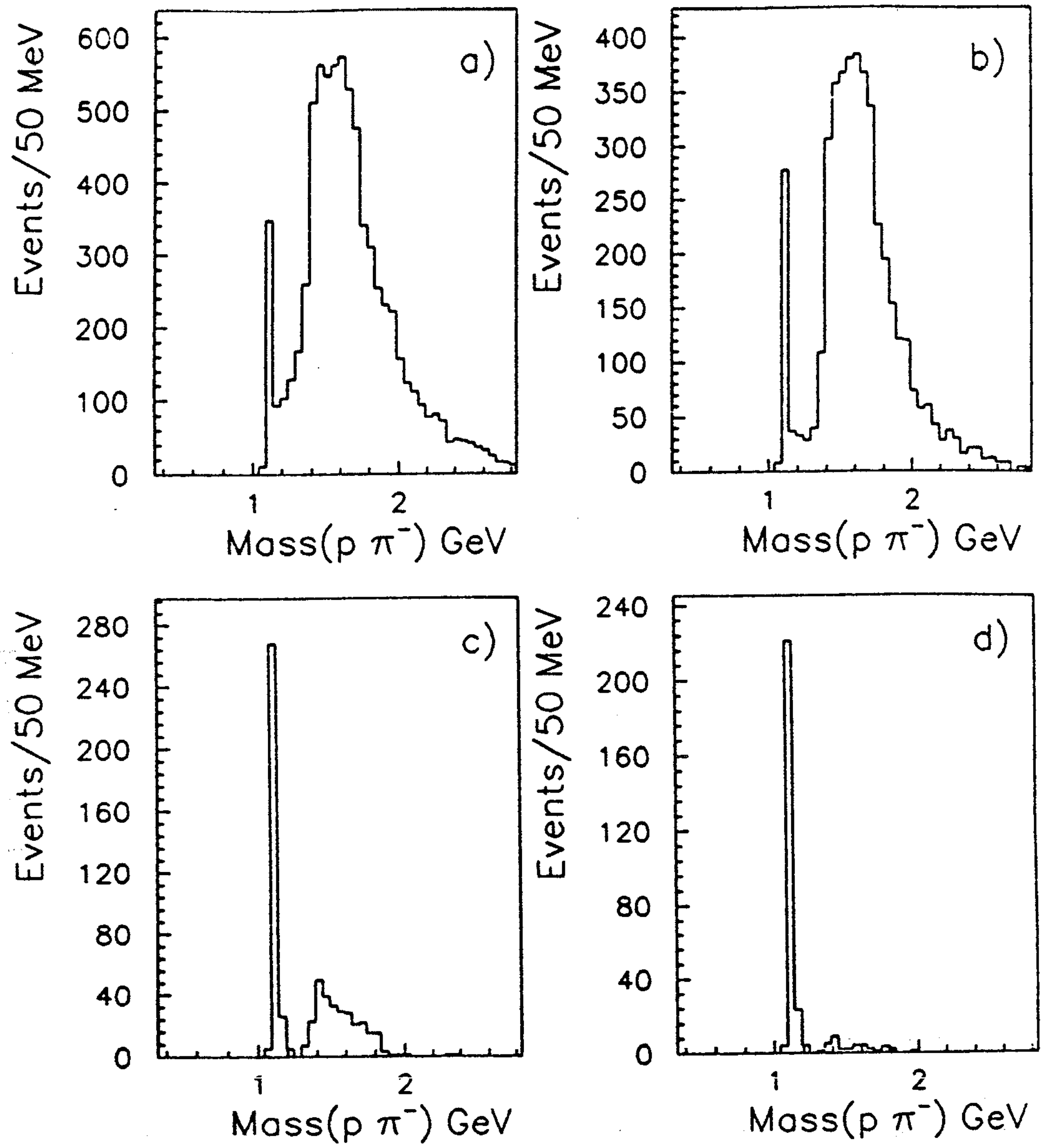

Figure 3.8: Effective mass plots of Λ candidates after cuts a) 1 to 4, b) 1 to 5, c) 1 to 6 and d) 1 to 8. The cuts are defined in section 3.6

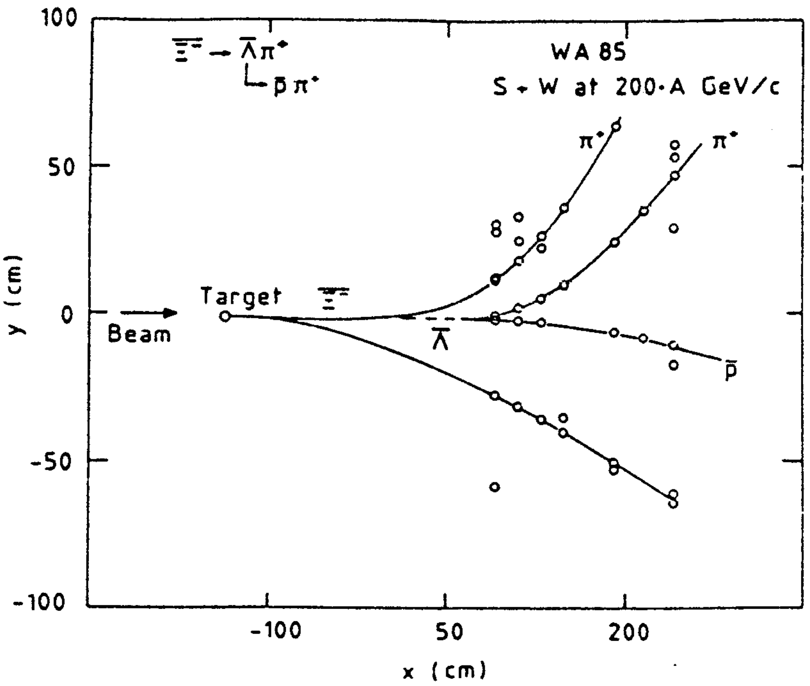

Figure 3.9: A fully reconstructed event with a Ξ^- candidate

The requirement that all tracks should trace through all the chambers is also relaxed, in order to get a reasonable acceptance, but the basic requirement of four space points per track is unchanged. Altogether, the acceptance region for Ξ^-s are somewhat different from Λs. This has to be taken into account when production ratios of the different particles are calculated.

A fully reconstructed event with a Ξ^- (actually an $\overline{\Xi^-}$) candidate is shown in figure 3.9. All the decay tracks are well identified, and the background is still low. An effective mass plot of the Ξ^- candidates is shown in figure 3.10.

3.8 Λ corrections

As can be seen from figure 3.6, the Armenteros plot ellipses for lambdas and kaons overlap in some regions. This cause a certain contamination of K^0s in the lambda sample. To avoid this ambiguity, an additional cut is imposed on the α parameter. Thus, unambiguous Λs and $\overline{\Lambda}$s are identified by the cut $0.45 < |\alpha| < 0.60$.

Some of the Λs observed in the wire chambers are likely to originate from Ξ^- decays. The number of Ξ^-s in the region $2.3 < y < 3.0$, $1.1 < p_t < 3.3$ GeV/c is known from the experiment. Monte Carlo studies based on this information [Aba91a] have been carried out to estimate the production of Ξ^-s in the total Λ acceptance region. This study gives a total contamination of the Λ sample of 22 ± 4 %. The number of $\overline{\Xi^-}$s is too low to apply the same technique to obtain the contamination of the $\overline{\Lambda}$s. An estimate can be obtained from the measured $\overline{\Lambda}/\Lambda$ and $\overline{\Xi^-}/\Xi^-$ ratios, along with the number obtained above. From these considerations, 45 ± 12 % of the $\overline{\Lambda}$ sample seem to originate from $\overline{\Xi^-}$ decays.

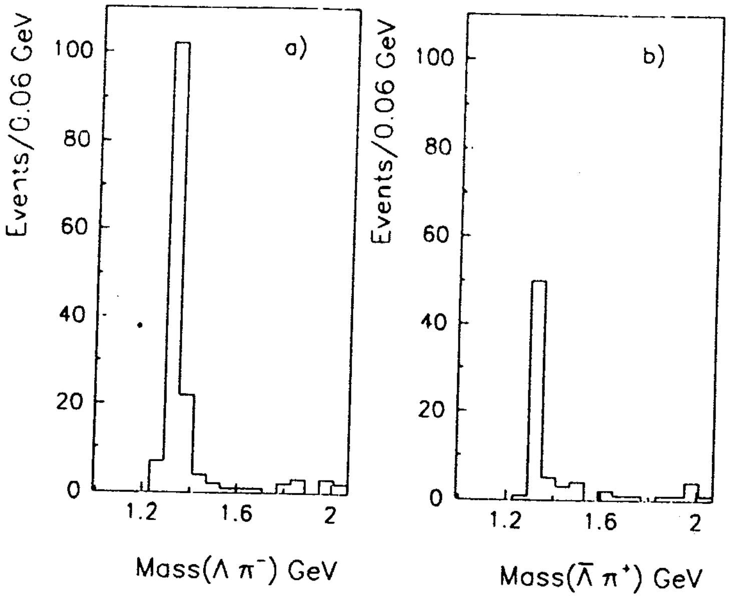

Figure 3.10: Effective mass plots for Ξ^- and $\overline{\Xi^-}$ candidates

Table 3.1: Raw data yields for different particle species in 1987/88 runs

Species	SW	pW
Λ (all)	13307	3223
Λ (unambiguous)	5586	1141
$\overline{\Lambda}$ (all)	3407	959
$\overline{\Lambda}$ (unambiguous)	1138	365
K_s^0	2753	1001
Ξ^-	108	82
$\overline{\Xi^-}$	44	22

3.9 WA85 results

The data taken in 1987/88 were subject to the analysis discussed in the previous sections. After all cuts, the raw data yields were as shown in table 3.1.

3.9.1 Multiplicity dependence

The total multiplicity measured in the two microstrip planes is closely related to the centrality of the collision. The formation of hot and dense matter is expected to be most developed in central collisions. If a centrality dependence of some quantity is observed, this could give evidence of production mechanisms involving a hot zone at central rapidity. NA35 has observed an increasing production of strange particles when going from low multiplicity to high multiplicity, as discussed in chapter 2.

The multiplicity dependence of lambdas and of charged particles in WA85 is shown

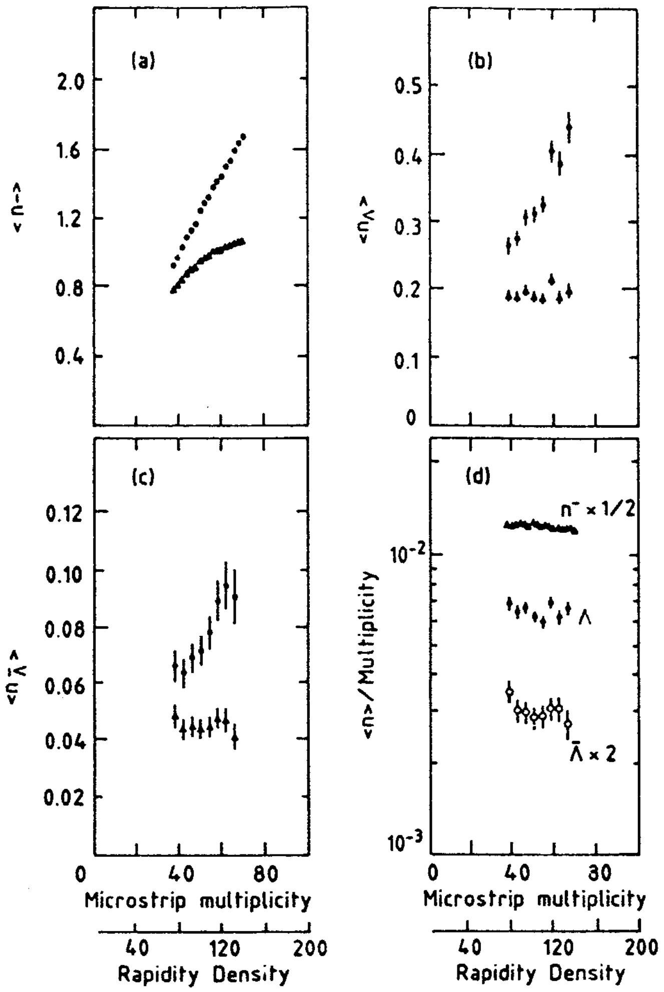

Figure 3.11: Multiplicity dependence of lambdas and negative particles

in figure 3.11 [Aba90]. Figure 3.11 (a) shows all negative particles, (b) lambdas and (c) anti-lambdas. The lower points (triangles) are corrected for geometrical acceptance only, the upper points (circles) are corrected for geometrical acceptance and reconstruction efficiency (discussed below). Figure 3.11 (d) shows the above quantities divided by microstrip multiplicity as a function of multiplicity. All the three ratios are compatible with being constant over the range of multiplicities in question. The WA85 trigger excludes peripheral collisions, so the data cannot be extended to the low multiplicity region of the NA35 data sample. Hence there is not necessarily a disagreement between the two experiments.

3.9.2 Transverse mass distributions

Particles emitted from a thermal source are expected to have a transverse mass distribution given by [Egg91]

$$\frac{1}{m_t}\frac{\mathrm{dN}}{\mathrm{d}m_t} = e^{\beta m_t} \tag{3.2}$$

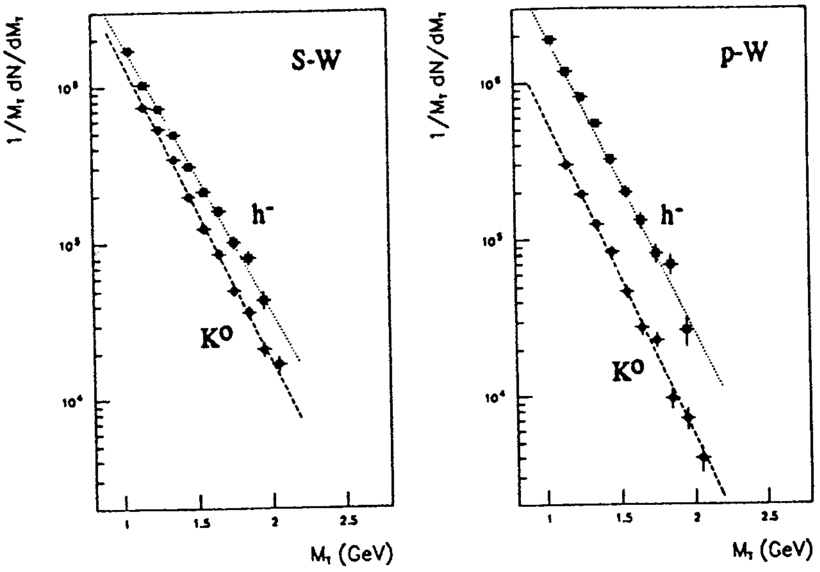

Figure 3.12: Transverse mass distributions for kaons and negative particles

where β is the inverse temperature and m_t is the transverse mass ($m_t = \sqrt{p_t^2 + m^2}$). This formula is valid for particles of a given rapidity. To approximate this condition, particles in a narrow rapidity region ($2.4 < y < 2.6$) were chosen from the WA85 data sample. The experimental acceptance does not vary much within this interval. The m_t distributions for the various particle species are shown in figures 3.12 and 3.13. Figure 3.12 shows the kaon distributions in sulphur and proton reactions [Kin92]. Figure 3.13 shows the transverse mass distributions for the observed baryons, along with the sum of the negative particles. The number of $\overline{\Xi}^-$s observed was too low to extract a m_t distribution.

The inverse slopes of the transverse mass distributions can be associated with a temperature. The temperatures thus extracted are summarised in table 3.2. The temperatures related to the strange particle species are all compatible with a value of about 230 MeV. The temperature related to all negative particles (mostly pions) appears slightly higher. The higher pion temperature might be due to the Cronin effect [Sch92, Cro75]. A high-p_t enhancement is seen above p_t= 1 GeV/c in figure 1.8. This region includes the whole acceptance region of WA85. The Cronin effect is more pronounced in pion spectra than in proton and deuteron spectra [Cro75], and it seems reasonable that this trend could continue towards the heavier Λ and Ξ baryons. All temperatures are slightly higher than what is observed in most other experiments. This can be due to the very central trigger in WA85.

The total abundance of all the strange particles in question seems to increase by a factor of about two compared to the total production of negative particles, when going from proton-tungsten to central sulphur-tungsten interactions. Transverse mass distributions for Λ, $\overline{\Lambda}$ and negatives in pW and SW reactions are shown in figure 3.14. The hyperon production cross section compared to the negatives is clearly higher in SW data than in pW data. This is in fair agreement with what is observed in other experiments, as discussed in chapter 2.

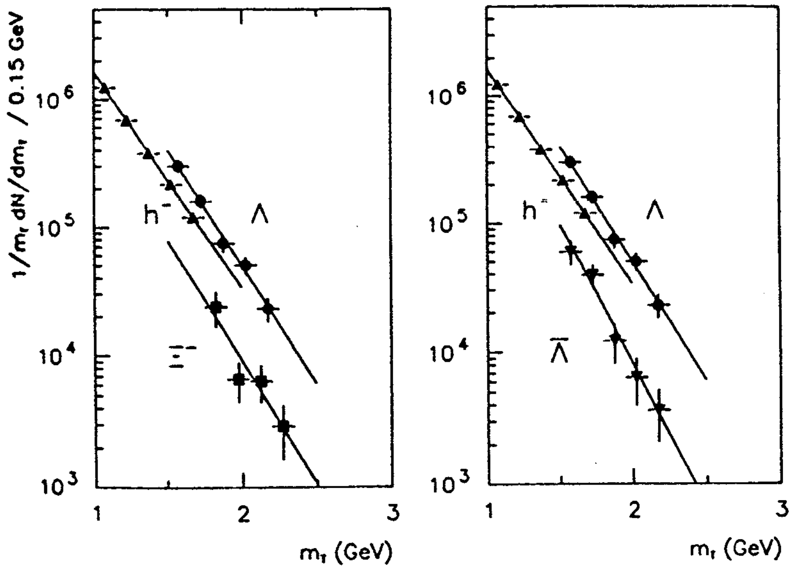

Figure 3.13: Transverse mass distributions for baryons and negative particles in sulphur-tungsten reactions

Table 3.2: Inverse slopes of various particle species

Species	Inverse slope (MeV)	Error (MeV) statistical	Error (MeV) systematical
h^-	256	± 3	± 15
Λ	238	± 9	± 15
$\overline{\Lambda}$	201	± 24	± 15
K^0_s	224	± 5	± 15
Ξ^-	233	± 54	± 15

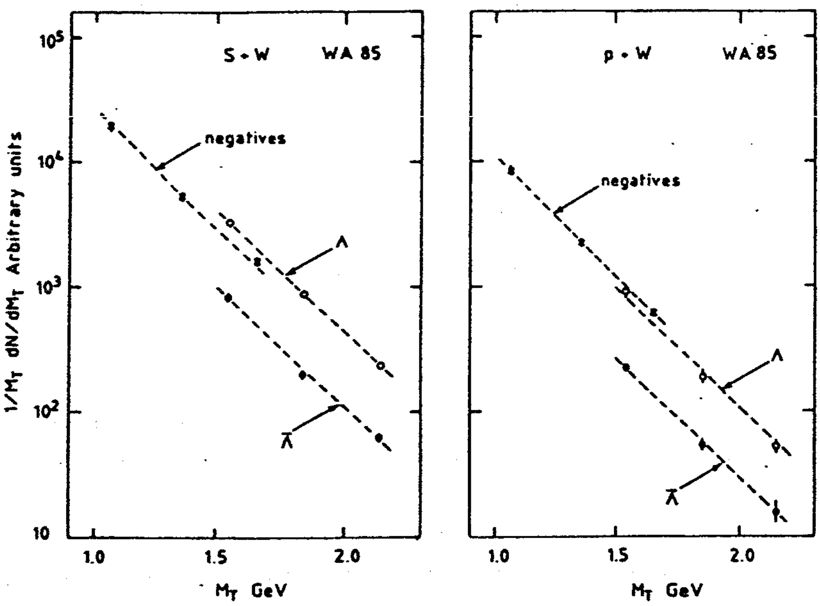

Figure 3.14: Transverse mass distributions in sulphur-tungsten and proton-tungsten interactions.

Table 3.3: Relative production rates for various hyperons

Ratio	m_t> 1.72 GeV	1 < p_t< 2 GeV/c
Λ/Λ	0.13 ± 0.03	0.13 ± 0.03
$\overline{\Xi^-}/\Xi^-$	0.39 ± 0.07	0.39 ± 0.07
Ξ^-/Λ	0.20 ± 0.04	0.11 ± 0.02
$\overline{\Xi^-}/\overline{\Lambda}$	0.6 ± 0.2	0.33 ± 0.11

3.9.3 Particle abundance ratios

To calculate the ratio of production of different particle species, a good control of the various sources of error in the experiment is needed. The data are corrected for acceptances, reconstruction efficiency, ambiguities in the particle identification and feed-down production of Λs from Ξ^- decay.

To compare with other experiments, the cuts in rapidity and p_t should be similar. Due to the different masses of Ξ^-s and Λs, the production ratio is different depending on whether a p_t or m_t cut is used. The experimental values obtained from the WA85 1987 data are shown in table 3.3 [Aba91a]. The strange baryon production ratios observed by WA85, are compared to previous experiments in figure 3.15. The Ξ^-/Λ ratio seems compatible with previous data, but the $\overline{\Xi^-}/\overline{\Lambda}$ ratio appears much higher in the WA85 ion data than in previous e^+e^- and proton-proton data. The error bars are large, however, mostly due to the very limited number of $\overline{\Xi^-}$s in the 1987 data sample. This situation is expected to improve when the analysis of the 1990 data is completed, with its 7-fold increase in statistics.

3.10 Reconstruction efficiency

A perfect detector would detect all particles coming out of the reaction zone. In real detectors, some particles are lost, and fake signals may occur. Two major effects contribute to loss of tracks in the WA85 setup:

Geometrical acceptance: is a measure of what part of space is covered by detectors.

Reconstruction efficiency: gives the detectors' ability to reliably sense the particles that pass through them, combined with the ability of the analysis programs to reconstruct the correct signal from the detectors.

The geometrical acceptance of the WA85 detector setup is optimised to cover a small amount of phase space only. The acceptance can be measured by pure geometrical considerations, (the chambers are only sensitive above the beam, and only within the butterflied region etc.). Furthermore, the effect of unseen decay modes (like $\Lambda \rightarrow n + \pi^0$) is included in the acceptance.

The reconstruction efficiency depends both on the quality of the physical detector and the features of the off line reconstruction program chain. A particle which flies through the chambers will normally leave a track, which can later on be reconstructed.

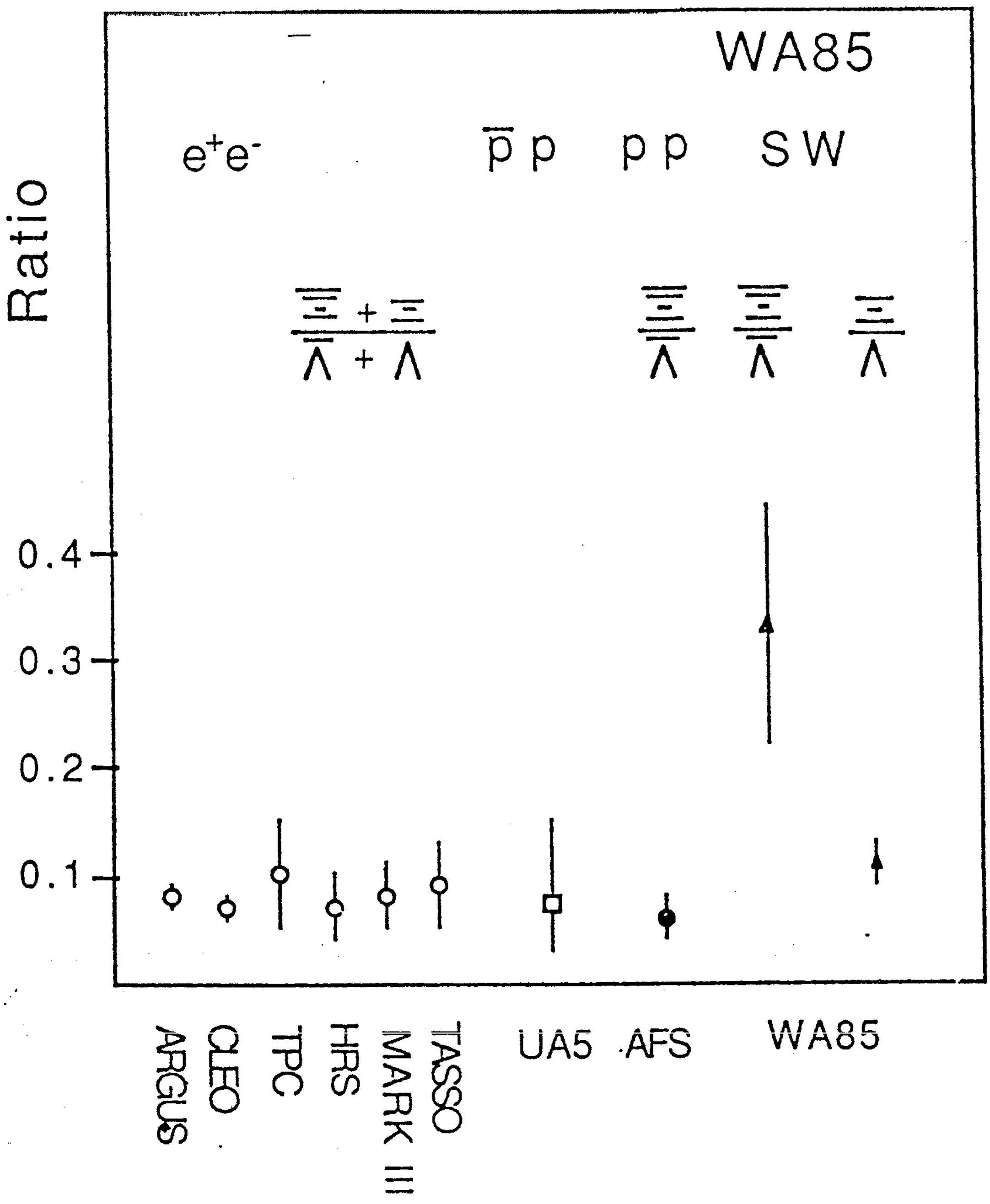

Figure 3.15: Ξ^-/Λ production rates in various experiments

At some instances, the chambers may be inefficient, so no wire hit is recorded. Also, the reconstruction program may be inable to reconstruct tracks from correctly recorded wire hits. This would typically be the case if the hit density is too large, making the algorithm unable to group the correct hits into tracks.

The complete reconstruction efficiency is estimated by Monte Carlo methods. A number of particles are generated randomly according to given distribution functions. These particles are then implanted into real events, and the merged events are fed through the normal analysis chain. Finally the number of reconstructed particles is compared to the number of generated ones. The reconstruction efficiency can then be calculated. The method is discussed in further detail below.

3.10.1 Smearing

Due to the finite resolution of the detector system, the measured quantities will in principle deviate from the 'true' values carried by the physical particle. This effect may cause particles within the acceptance region to get lost, because their reconstructed values may fall outside the experimental cuts. On the other hand, particles with 'true' y-p_t values outside the cuts may get reconstructed values within the acceptance region.

These effects should be taken into account when calculating reconstruction efficiency. The loss of 'good' particles will occur trivially. To allow for smearing in the opposite direction, Monte Carlo particles are generated in a slightly larger y-p_t region than the one decided by the final experimental cuts. The Monte Carlo particles are tagged, so the reconstruction efficiency can be calculated as the number of particles found within the acceptance region divided by the number of particles generated within the same window.

3.10.2 The NAININ program

The NAININ [2] program is the first step in the reconstruction efficiency program chain. This program generates the Monte Carlo particles which will later on be merged with background data. A separate version of NAININ exists for each of the particle species in question. The three-momenta of the particles in question are generated according to the distribution functions discussed below. Then the NAININ cuts (which take smearing into account) are applied. If the particle fails NAININ cuts, it is discarded, and a new particle is generated. If the particle passes the NAININ cuts, it is tested and tagged according to the real experimental cuts. All relevant information is written to files.

The temperature in the transverse momentum distribution function is based on the measured quantity from the WA85 1987 data. The final geometry cuts require the tracks to pass more than 1 cm from the edge of the sensitive region of the chambers, to avoid physical edge effects. The NAININ cuts include the whole sensitive region, to account for smearing effects.

[2] The program name NAIN, the French word for dwarf, was selected to mark the contrast to the huge general-purpose detector simulation program GEANT (giant), available in the CERN program library.

Table 3.4: NAININ details

Distribution functions	Ξ^-s	Λs	π s
Rapidity	flat	flat	flat
Geometry (θ, ϕ)	flat	flat	flat
Transverse momentum	$p_t e^{-\frac{1}{T} m_t}$, T=200 MeV	$p_t e^{-\frac{1}{T} m_t}$, T=200 MeV	$p_t e^{-\frac{1}{T} m_t}$, T=200 MeV
Vertex position (Xi)	flat		
Vertex position (Lambda)	flat	flat	
NAININ cuts			
Rapidity	$2.1 < y < 3.1$	$2.0 < y < 3.2$	$2.1 < y < 3.1$
Transverse momentum	$0.9 < p_t < 3.4$	$0.7 < p_t < 3.0$	$0.7 < p_t < 3.0$
Geometry	trace A1-A4, sensitive region	trace A1-A7, sensitive region	trace A1-A7, sensitive region
Vertex position (Xi)	$-70 < X < 90$ cm		
Vertex position (Lambda)	$-35 < X < 90$ cm	$-20 < X < 90$ cm	

3.10.3 The NAIN program

The Monte Carlo data generated by NAININ is read by NAIN. This program traces the Monte Carlo particles through the Omega magnetic field, and calculates which wires should be hit in the A chambers. If a track passes the gap between two wires, more than 1/3 of the wire pitch distance from any of the single wires, a hit is produced in both of them.

A real event is then read from a TRIDENT output tape (which also contains the raw data). The Monte Carlo hits are merged with the real hits, and a new file is written in raw data format. This raw data file is then run through the normal analysis chain.

A sample of 'background tapes' is generated from the 1990 data. These tapes contain selected events in which no V^0 candidate was found by STRIPV0. (There might of course be real V^0s there, which escaped reconstruction.) The background events are selected randomly from the sample of 700 raw data tapes. All reconstruction efficiency calculations are based on these background events.

3.10.4 Lambda efficiencies

The 'raw data tape' produced by NAIN is passed through the normal TRIDENT and STRIPV0 programs. Then the output of STRIPV0 is compared to the Monte Carlo output from NAININ. The V^0 candidates from STRIPV0 are subjected to the cuts discussed in section 3.6. The reconstruction efficiency is computed as

$$\text{eff}_i = \frac{N_{\text{found}}}{N_{\text{gen}}} \qquad (3.3)$$

where N_{gen} is the number of lambdas generated within the experimental cuts. (These are tagged by NAININ.) The efficiency depends on the multiplicity, and is plotted as a

Table 3.5: Reconstruction efficiencies for lambdas

Multiplicity	Number of events	Good lambdas	Found lambdas	Efficiency (%)
0.- 40.	223705	117567	42507	36.2 ± 0.2
0.- 4.	794	405	270	64.7 ± 4.6
4.- 8.	10474	5546	3354	60.9 ± 1.2
8.- 12.	43792	23198	12570	54.6 ± 0.6
12.- 16.	73376	38455	16290	42.2 ± 0.4
16.- 20.	58648	30641	8097	26.3 ± 0.3
20.- 24.	25632	13426	1743	12.9 ± 0.3
24.- 28.	6257	3348	171	5.2 ± 0.4
28.- 32.	881	468	12	2.6 ± 0.8
32.- 36.	114	58	0	0.0 ± 0.0
36.- 40.	15	6	0	0.0 ± 0.0

function of the average number of cluster hits in the A chambers. (If adjacent wires fire, the hit is recorded as a 'cluster', where first wire number and number of fired wires are given. The number of clusters in each plane is summed, and divided by 21 (number of wire planes) to give the average multiplicity.)

The efficiencies obtained for the WA85 1990 data are shown in table 3.5. These numbers are based on 223705 events from the background tapes. NAININ generated 117567 lambdas satisfying all experimental cuts, the remaining Monte Carlo particles were slightly outside the acceptance to account for smearing. The STRIPV0 program and the ANALYZ90 equivalent reconstructed 42507 lambdas, giving an overall efficiency of 36.2 ± 0.4 %, errors given by statistics.

3.10.5 Pion efficiencies

The pion events are naturally not passed through the V^0 finding procedure. The program RECPI reads TRIDENT output, and tries to find a track similar to the one implanted by NAININ. The distances between the Monte Carlo track and each experimental track in chamber A1 and A7 are calculated. These distances are calculated separately in the Y and Z component. Each component is squared, then the Z components are divided by 5 to take the better resolution in the Y direction into account. Finally the sum of squares is calculated for each track. In each event the track with the smallest sum of squares is selected. The A1 Y coordinate of this track is compared to the A1 Y coordinate of the Monte Carlo track. If the distance between these two coordinates is less than 0.5 cm, the pion is considered 'found'. The reconstruction efficiency is defined by

$$\text{eff} = \frac{N_{\text{found}}}{N_{\text{gen}}} \tag{3.4}$$

where only the pions tagged as being inside the experimental cuts are counted in N_{gen}. The experimental cuts used are the same as the ones applied for lambdas, naturally excluding the vertex position.

Table 3.6: Reconstruction efficiencies for pions

Multiplicity	Good pions	Found pions	Efficiency (%)
0.- 40.	52413	42272	80.7 ± 0.5
0.- 4.	376	371	98.7 ± 7.2
4.- 8.	3541	3469	98.0 ± 2.3
8.- 12.	12301	11441	93.0 ± 1.2
12.- 16.	17546	15012	85.6 ± 1.0
16.- 20.	12409	8954	72.2 ± 1.0
20.- 24.	4968	2607	52.5 ± 1.3
24.- 28.	1104	389	35.2 ± 2.1
28.- 32.	145	28	19.3 ± 4.0
32.- 36.	20	1	5.0 ± 5.1
36.- 40.	2	0	0.0 ± 0.0

The efficiencies obtained for the WA85 1990 data are summarised in table 3.6. NAINPI generated 52413 pions satisfying all experimental cuts. They were implanted into the background events, where 42272 pion tracks were succesfully reconstructed by TRIDENT, giving an overall efficiency of 80.7 ± 0.5 %. The pion reconstruction efficiency is calculated as a function of average number of cluster hits in the A chambers, as discussed in the previous section.

3.10.6 Other efficiencies

Similar calculations are carried out for all particles in question (K^0, $\overline{\Lambda}$, Ξ^-, $\overline{\Xi^-}$), by several laboratories inside the collaboration. Separate versions of NAININ and the final efficiency program exist for each particle species; the NAIN and TRIDENT programs are the same throughout.

The reconstruction efficiencies for Ξ^-s [Eva93], are given in table 3.7. The overall efficiency is 19.7 ± 0.3% .

The efficiencies for antiparticles are slightly different from the efficiency of their corresponding particles, since more positive than negative particles produce tracks in the chambers. (As is shown in the tables above, the efficiency drops rapidly with increasing track density.) This effect is rather small, and the antiparticle efficiencies are close to those of the corresponding particles.

3.11 Positive/negative ratio

The relative number of tracks produced by positive and negative particles may provide useful information of the dynamics of the heavy ion reaction. Since the atomic electrons don't take part in the reaction (the projectile electrons are stripped off prior to acceleration, the target electrons are blown off when the collision take place), there is an excess of positive particles due to the incoming protons.

Table 3.7: Reconstruction efficiencies for xis

Multiplicity	Efficiency (%)
0.- 40.	19.7 ± 0.3
0.- 4.	38.1 ± 9.5
4.- 8.	45.0 ± 2.1
8.- 12.	34.1 ± 0.9
12.- 16.	22.9 ± 0.5
16.- 20.	12.2 ± 0.4
20.- 24.	3.7 ± 0.4
24.- 28.	1.2 ± 0.4

Preliminary results from the WA85 1990 sulphur-tungsten data are shown in figure 3.16, along with reference data taken by a Chicago-Princeton collaboration in proton-nucleus interactions [Ant79]. Both the sulphur-tungsten and proton-tungsten data taken at 200 GeV show a strong dependence on p_t.

The WA85 data are subject to some initial cuts; all tracks should trace back to the target (± 6 cm), they should pass through the sensitive region of all the chambers, and they should contain at least four space points. There is as yet no cut in rapidity or transverse momentum. Neither are any corrections done.

Efficiency and acceptance corrections must be applied before a final positive/negative ratio can be presented. To make proper corrections, the particles in question should be identified (pion, kaon or proton). This is not possible in the WA85 setup. To carry the analysis further, the relative production ratio of these particle species must either be obtained from other experiments, or extracted from model calculations. The latter option would of course make the experimental result model dependent to some extent. Further work in this direction is in progress [Lov93].

A QGSM cascade model calculation [Ame90] shows a slight increase in the positive/negative ratio with transverse momentum, stabilising at a value around 1.5 at transverse momenta above 1.0 GeV/c, in central sulphur-tungsten interactions. This effect is weaker than the one observed in the experimental data. The QGSM results are shown in figure 3.17.

The observed p_t dependence of the positive/negative ratio might be explained by collective flow effects. A large fraction of the detected positive particles are protons. The proton production cross section obtained from the hydrodynamic flow model of Csernai and collaborators, peaks at a higher value of p_t than is the case for pions [Cse89]. The effect is illustrated in figure 3.18, taken from [Cse89], which shows transverse momentum spectra for pions, kaons and protons.

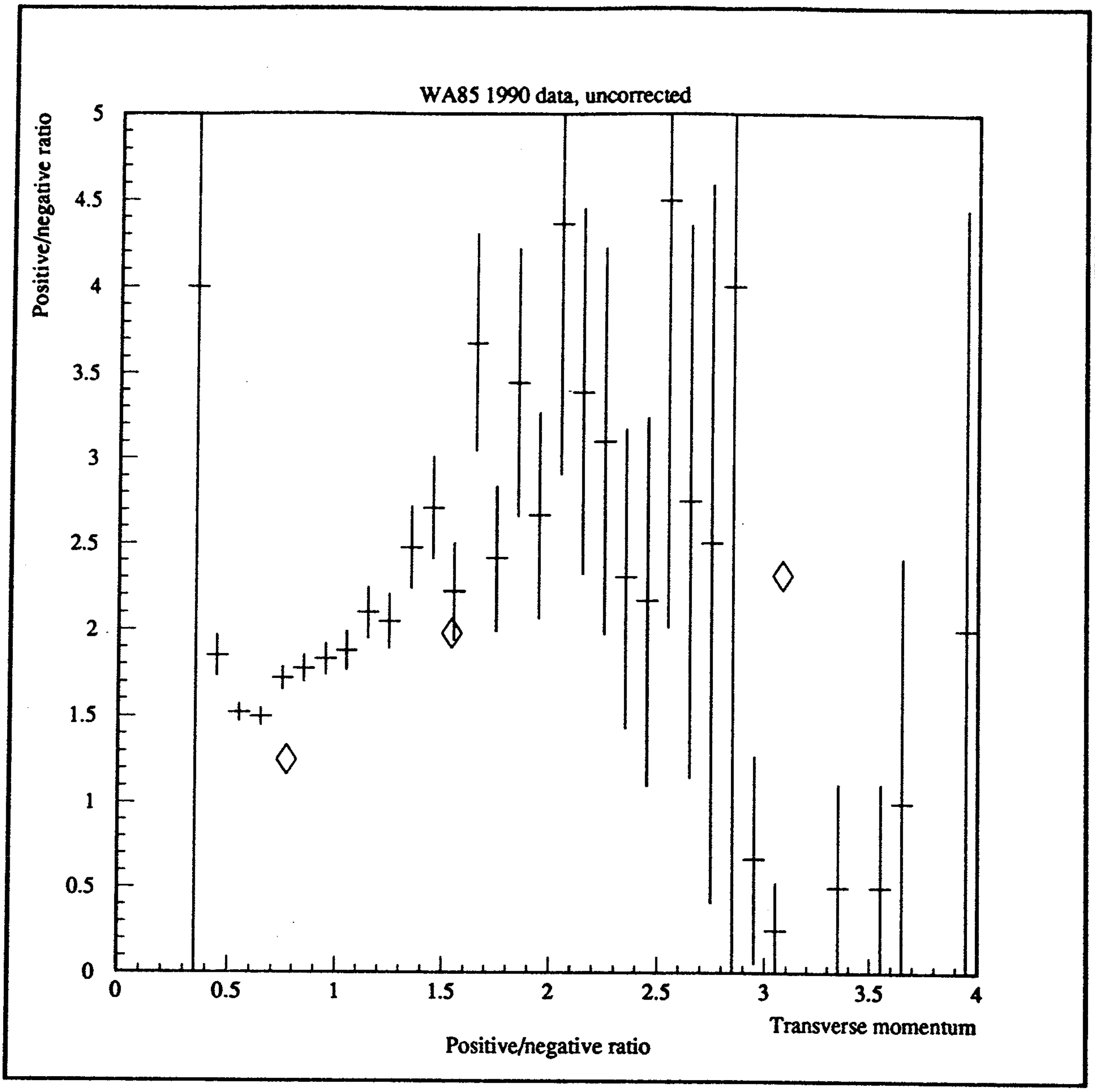

Figure 3.16: Positive/negative ratios from WA85 1990 data (S+W) and Chicago-Princeton reference data (p+W, marked with diamonds).

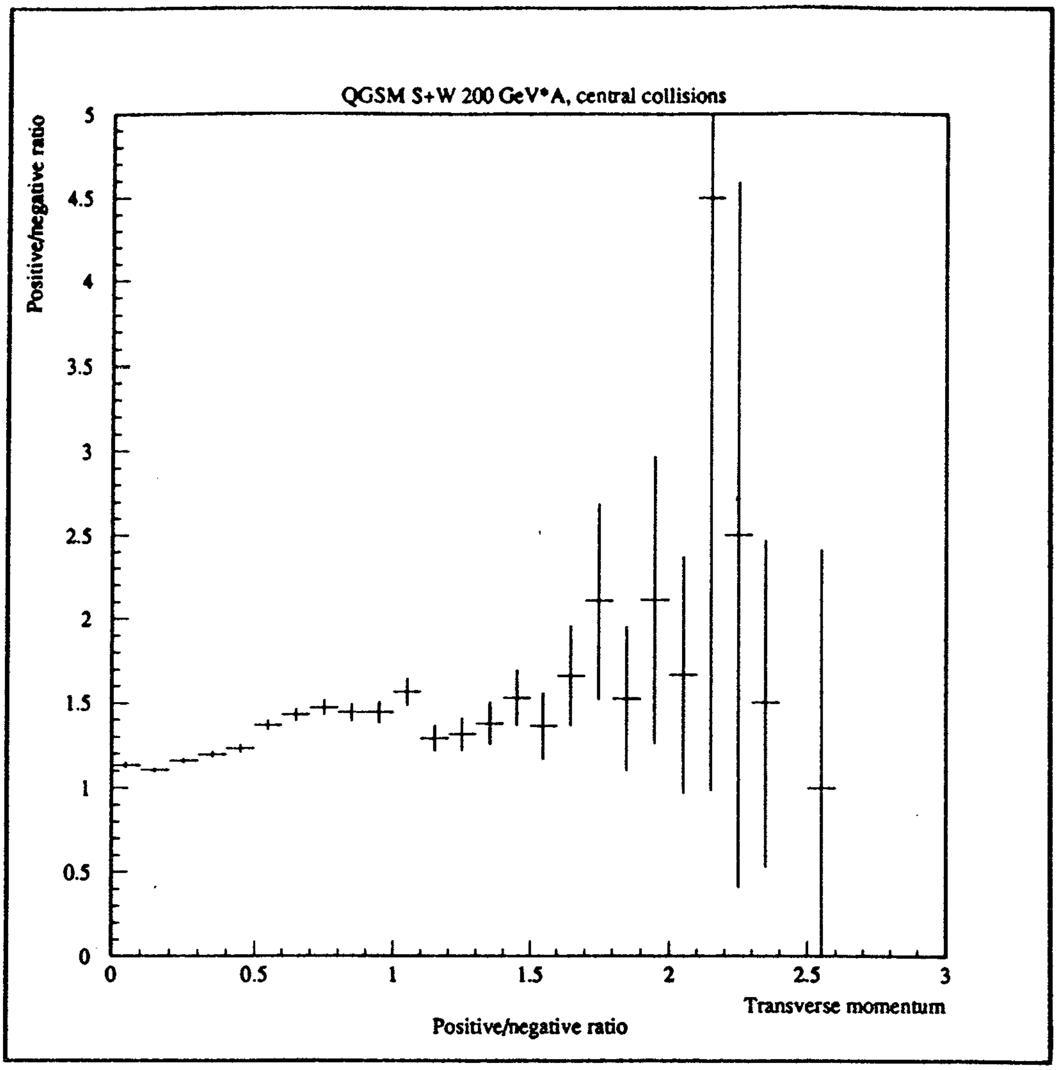

Figure 3.17: Positive/negative ratios calculated by QGSM

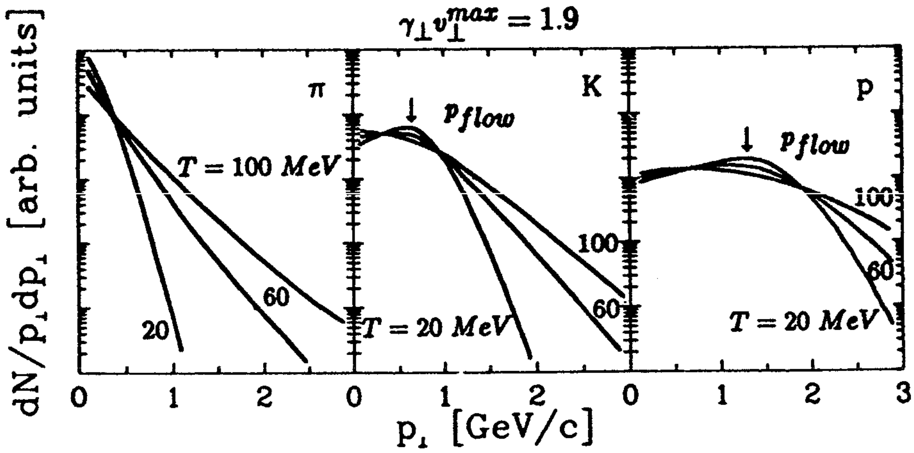

Figure 3.18: Transverse momentum spectra of pions, kaons and protons, produced by the hydrodynamic model of Csernai et al. [Cse89]

Chapter 4

The WA94 Experiment

The experimental programme of the WA85 collaboration was continued by the WA94 collaboration from 1991.

The WA94 experiment takes data from sulphur-sulphur interactions, provided by the 200 GeV·A sulphur beam in the CERN SPS. By the symmetry in this reaction, a wider region of phase space can be investigated than was the case in WA85. Furthermore, symmetric sulphur on sulphur collisions will be a useful reference to the lead-lead experiments foreseen at the SPS in the autumn of 1994. The WA97 experiment, which is based on the WA85/WA94 setup, is already approved to take part in this programme.

In addition to the particle species already identified by WA85, WA94 intends to measure the production of protons and antiprotons. Thereby baryons carrying 0,1,2 and hopefully 3 units of strangeness can be studied. The Ω^- can be identified by methods very similar to the Ξ^- identification, once the number of produced Ω^-s is sufficient to obtain a statistically significant result. To identify the protons among the 'stable' particles produced in the reaction (pions, kaons and protons), a RICH detector has been used. This detector will be discussed in more detail in the next chapter.

4.1 Data taking

The WA94 experiment runs with two different setups. In the 1991 run the butterflied Omega chambers were used to obtain hyperon production yields. The 900 tapes of raw data taken contain 100 million triggers. Proton production was measured by the RICH detector along with a silicon telescope in the 1992 run, resulting in 250 tapes of raw data, with 20 million triggers. Proton reference data for both setups will be taken in 1993 and 1994.

The offline production phase of the 1991 chamber data is completed. Further analysis is in progress. The offline processing of the 1992 data is still under preparation.

4.2 Apparatus

The experimental layout used in the 1991 run, is shown in figure 4.1. This setup closely resembles that of WA85, discussed in some detail in the previous chapter. The pixel and PAD detectors are to be used in the lead beam by the WA97 collaboration, and were only tested in this setup. The RICH detector and the additional wire chambers were operated in the 1992 run of WA94. They were only tested for short periods during the 1991 run.

The 1992 layout is shown in figure 4.2. In this setup all wire chambers inside the Ω magnet are removed, and a new silicon microstrip telescope acts as tracking device. The RICH is operational, as well as the additional wire chambers located behind the RICH (they are known as 'B chambers'). The small 'fast RICH' located inside the Ω magnet was used for test purposes only, and was only operated for a short period of time.

4.2.1 The silicon telescope

The silicon telescope consists of 14 planes of silicon microstrip detectors. Each detector has a sensitive region of 5×5 cm^2. The detector surface is divided into strips which can be read out separately. The strip number is the analogous of the wire number in a traditional wire chamber. The first 10 planes have a resolution of 50 μm (the sensitive region consists of 1024 strips). The last four planes have 2048 strips per plane, with a resolution of 25 μm.

Each plane gives one space coordinate only. To obtain three-dimensional space points, the planes have different orientations. Y planes have vertical strips, making the hit strip number proportional to the Y coordinate in space. The Z planes have their strips in the horizontal direction. The U planes are rotated 10.14^o relative to the Y planes, and the W planes are rotated 10.14^o relative to the Z planes.

In the 1992 setup, the purpose of the silicon telescope is to measure the position and momentum of the tracks that will continue towards the RICH. The RICH is only sensitive to particles arriving above the beam. To optimize the acceptance of the whole setup, the entire telescope is tilted by an angle of 69 mrad. The whole sensitive region of the telescope is located above the beam axis, to avoid excessive multiplicities in the microstrips.

A plane of silicon pixels, with two dimensional readout, is placed between microstrip plane 6 and 7. This plane was used for tests towards the WA97 pixel telescope only.

4.2.2 The RICH detector

The purpose of the RICH detector, which will be discussed in detail in the next chapter, is to identify protons and antiprotons among the 'stable' particles produced in the reactions. (Stable particles in this sense mean particles that don't decay inside the area spanned by the detector setup. These particle species include pions, kaons and protons and their antiparticles.)

The RICH, a Ring Imaging CHerenkov detector, is based on the Čerenkov principle. A particle travelling with a speed higher than the speed of light in the medium, will emit Čerenkov radiation. The Čerenkov radiation is emitted in a fixed angle with respect to the particle trajectory. This angle is related to the particle velocity.

The track momentum can be determined from the silicon telescope. Information on the particle velocity and momentum is sufficient to determine the particle mass.

A number of measures have to be taken to prevent the RICH from being flooded with tracks from the heavy ion reaction. These are discussed in detail in the next chapter.

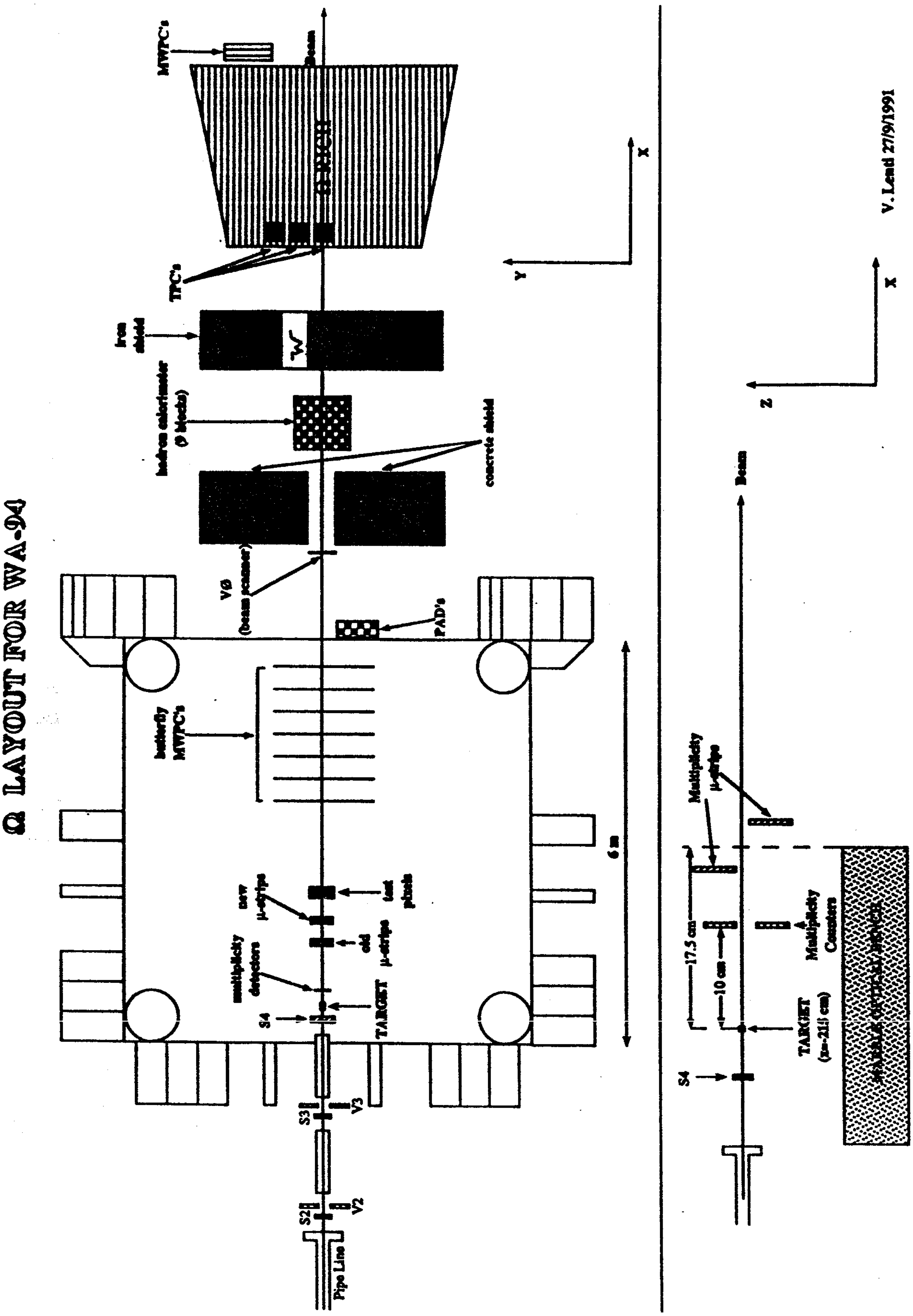

Figure 4.1: WA94 setup for the 1991 run

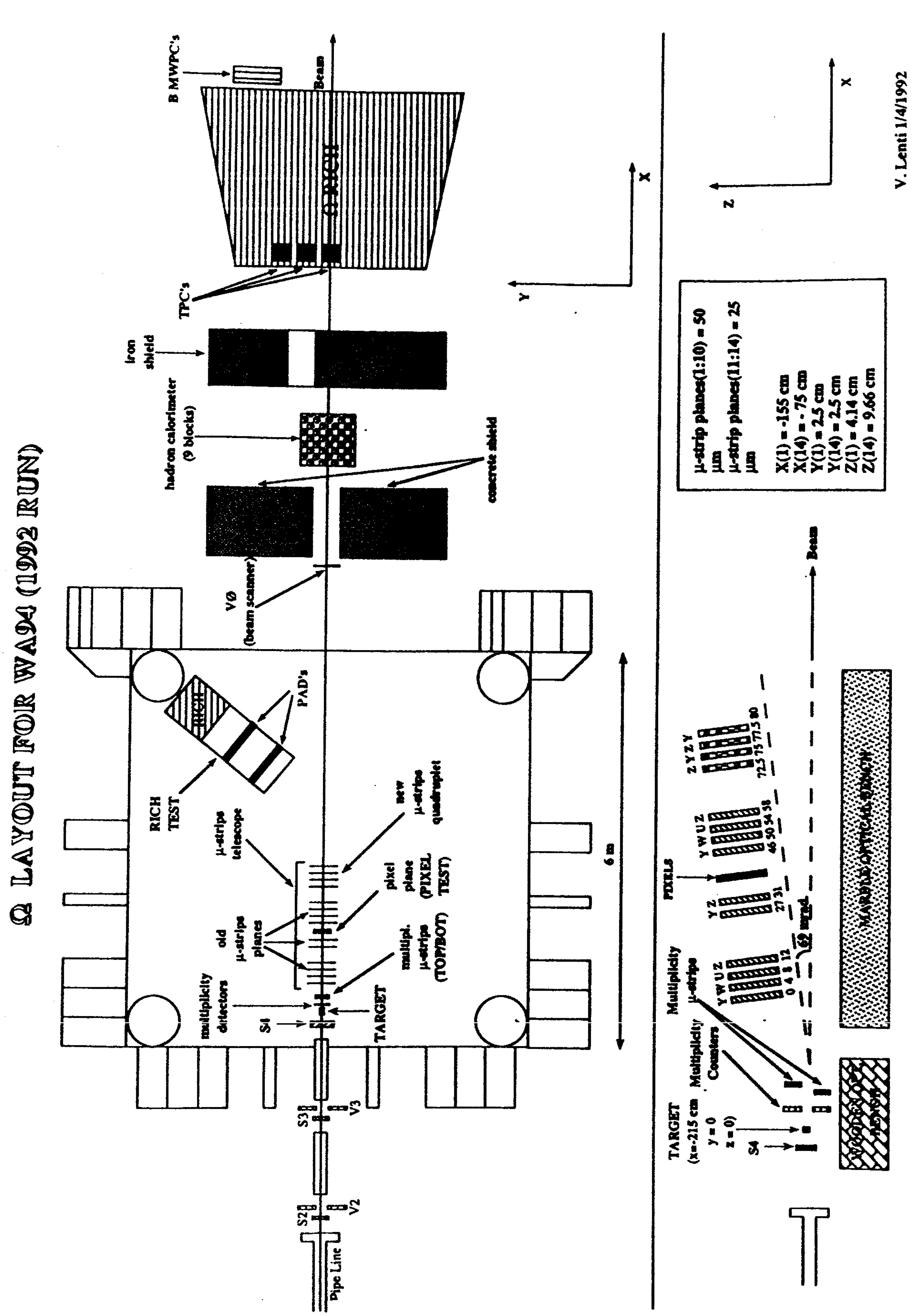

Figure 4.2: WA94 setup for the 1992 run

4.2.3 B Chambers

To obtain a reliable signal from the RICH, the exact position of the charged particle must be known. This position can in principle be determined from the silicon telescope, but since the RICH is placed 12 m downstreams from the telescope, the uncertainty in the measurements would be considerable.

A set of multiwire proportional chambers, the 'B chambers', are therefore placed behind the RICH to obtain some additional space points on the particle trajectories.

These chambers will also be discussed in some more detail in the next chapter.

4.3 Analysis

The analysis of the WA94 data is still in its early phase. Identification of strange baryons and antibaryons (Λ , Ξ^- and possibly Ω^-) will be done in a way similar to WA85, discussed in the previous chapter. The butterflied chambers have good acceptance in a rapidity window in the region 2.2< y <3.0.

Protons and antiprotons will be identified by the RICH. The telescope/RICH setup has a good acceptance in the rapidity interval 3.2< y <3.8.

The beam rapidity is 6.0. In the symmetric S+S system there is reflection symmetry around mid-rapidity, so the 3.2< y <3.8 interval can be mapped onto the 2.2< y <2.8 interval. Hence, there is a common region where particle abundance ratios can be computed.

Chapter 5

The RICH detector

The Ring Imaging CHerenkov detector (RICH) is used in the identification of protons and antiprotons among the non-decaying particles in the WA94 and WA97 experiments. The RICH measures the particle velocity. The particle momentum is determined in the silicon telescope. The particle position in the RICH is determined from combined tracks from the telescope and the B wire chambers, located behind the RICH. Altogether this information can be used to deduce the particle mass.

5.1 The Čerenkov principle

When a particle traverses a medium with a speed greater than the speed of light in that medium (this is possible if the refractive index is greater than one in the medium), Čerenkov radiation is produced [Che37]. The Čerenkov radiation consists of photons in the region of visible to ultraviolet light. It is emitted with a sharp maximum at the angle θ with respect to the particle trajectory, given by the formula

$$\theta = \arccos\left(\frac{1}{\beta n}\right) \tag{5.1}$$

where β is the relativistic velocity of the particle ($\beta = \mathrm{v/c}$), and n is the refractive index of the medium.

Since Čerenkov photons can be emitted at any position along the particle trajectory inside the radiative volume, the Čerenkov photons are confined to a cone around the particle trajectory. The Čerenkov photons can be found anywhere inside this cone. A photon detector plane in the forward direction would see signals scattered inside a disc, as illustrated in figure 5.1. The radius of the circumference of this disc would give the Čerenkov angle, but since Čerenkov photons are emitted randomly, there will generally not be photons all over the theoretically possible cone. A reliable reconstruction of the particle velocity is therefore not possible using this straightforward approach.

5.2 The RICH principle

All parallell light rays falling on a spherical mirror will be focused onto one point on a sphere having half the radius of the mirror. This can be shown geometrically, and is true

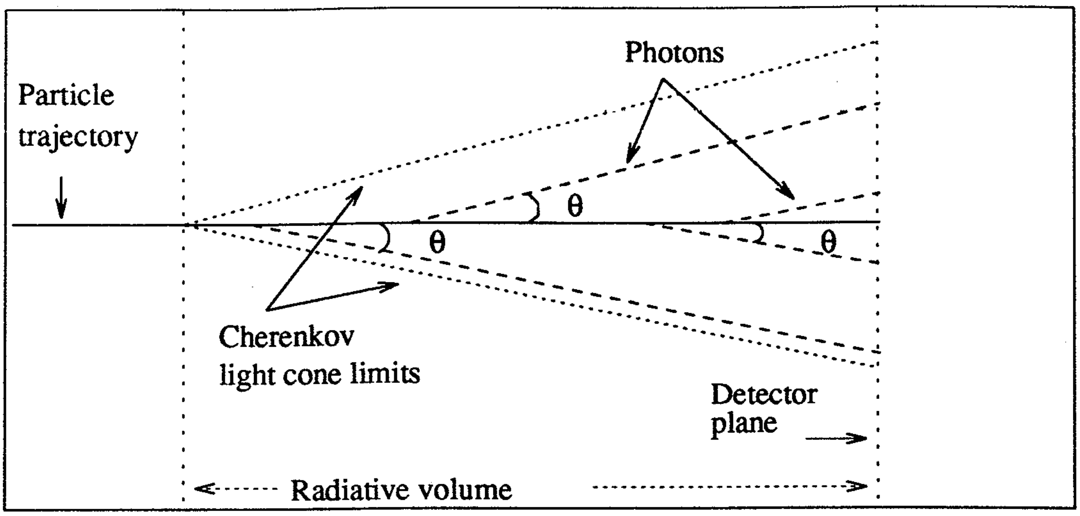

Figure 5.1: Čerenkov radiation

to the extent that $\sin\theta$ can be approximated by θ. By such an arrangement, the Čerenkov photons emitted at different positions along the particle trajectory, but with the same azimuthal angle, will be focussed onto one point on the image surface. The Čerenkov cone will thus be transformed into a ring, with a well defined radius. This radius depends directly on the Čerenkov angle, and thereby the particle velocity [Eke84].

The geometry is shown in figure 5.2. The particle traverses the detector along the solid line. The refractive medium, where Čerenkov photons are produced, is placed between the image surface and the mirror. Photons emitted at different points along the trajectory (dashed lines) are focussed onto the same point at the image surface. The dotted lines are the axes of incidence at the photon points of reflection.

5.3 The Omega RICH

The Omega RICH is part of the detector equipment of the Omega spectrometer. It was built by the WA69 Collaboration [Aps86], and was later taken over and improved by the WA89 Collaboration [For87]. A detailed description of the RICH can be found in ref. [Eng92].

The RICH consists principally of two systems. There is a radiator system where Čerenkov photons are produced, and a photon detector system where these photons are sensed and recorded. The radiator system fills most of the detector volume, and consists principally of a gas with a suitable refractive index. The detector system consists of Time Projection Chambers, mounted at a detector surface resembling a sphere with 5 m radius. The spherical mirror has a radius of curvature of 10 m. The radiator gas is placed between the detector sphere and the mirror sphere. The incoming charged particles will thus produce Čerenkov photons along a path of approximately 5 m.

A sketch of the detector is shown in figure 5.3. Charged particles enter through the TPC plane in front, and the Čerenkov photons are reflected at the spherical mirrors in

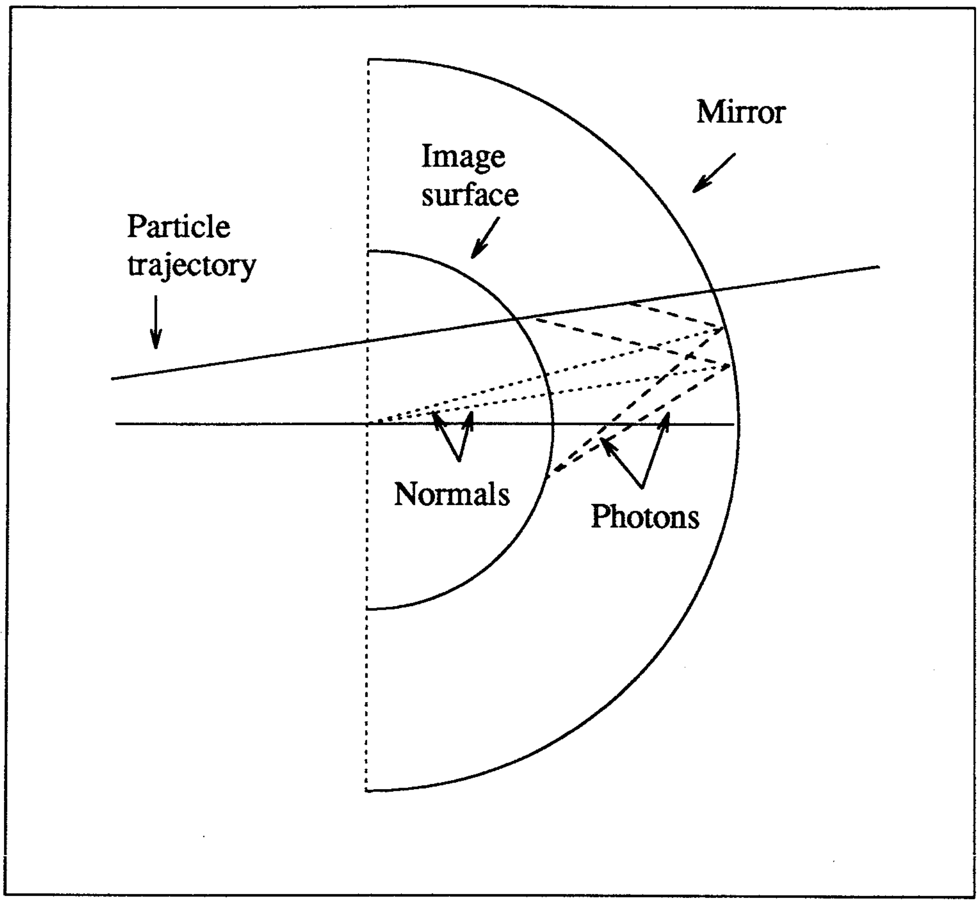

Figure 5.2: RICH geometry

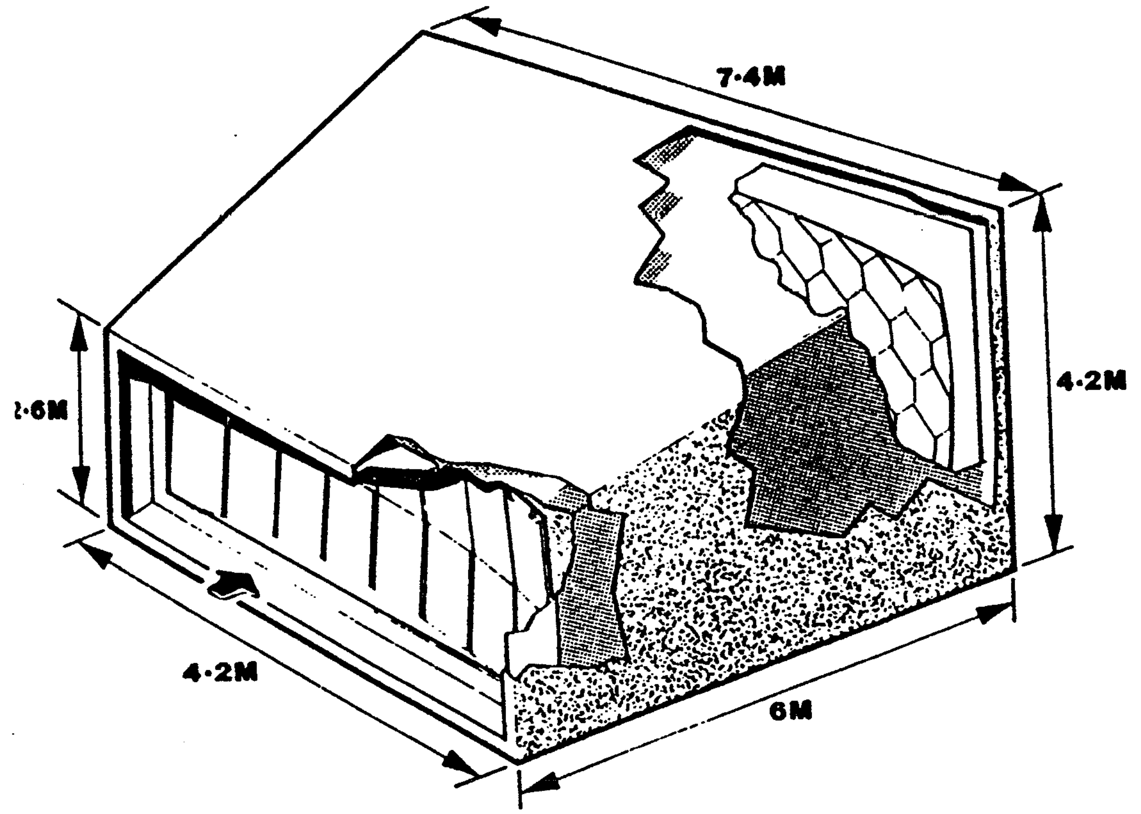

Figure 5.3: A sketch of the Omega RICH

the rear part of the detector box.

The Čerenkov photons are detected in the TPC modules in the front part of the detector. These modules contain a reactive gas (TMAE), which absorbs the incoming photons and emits electrons. The electrons drift towards the end of the chambers, where they are detected in sense wires. The combined information of wire number and drift time give Y and Z coordinates of the conversion point of the photon.

5.3.1 Radiator Gas

Only particles travelling with speeds greater than the threshold velocity $\beta = 1/n$ will produce Čerenkov light in the radiator. On the other hand, when the velocity is large, $1/\beta n$ doesn't change much, and the Čerenkov angle gets practically constant. This makes mass identification impossible. The radiator gas must have a threshold optimised to the momentum of the particles to be identified.

WA94 has chosen a mixture of nitrogen and freon (C_2F_6) [1]. Freon has a refractive index of 1.000793, giving thresholds for pions, kaons and protons at 3.8, 13.4 and 25.5 GeV/c respectively. We want to measure particles in the momentum range 15-50 GeV/c. Most protons will thus be below threshold, and we will have to identify protons and antiprotons by absence of signal in the RICH.

[1] This freon does no harm to the ozone layer. The environmentally questionable freons contain chlorine. These agents absorb UV light and release chlorine radicals. Such a behaviour would be disastrous inside the radiative volume, as we want to identify a very limited number of UV photons produced by the traversal of a charged particle.

For the 1992 run it turned out to be impossible to obtain enough C_2F_6. Towards the end of run we therefore increased the nitrogen content in the mixture. This probably reduced the number of produced Čerenkov photons per charged particle somewhat.

5.3.2 Mirrors

The Čerenkov photons are reflected at the mirror. The original WA69 RICH was equipped with 80 mirrors having a radius of curvature of 10 m. WA89 replaced the central mirrors by 19 new ones of better quality. These mirrors have a slightly lower radius of curvature. To make all mirrors focus onto the same image sphere, the new mirrors are placed correspondingly closer to the TPC sphere.

5.3.3 Chambers

After being reflected at the mirror, the Čerenkov photons are detected in the TPC chambers located at the RICH entrance. The chambers are arranged to resemble a spherical surface with a radius of curvature of 5 m, half the radius of curvature of the mirror.

The photons are let in through a thin quartz window at the rear side of the chambers. Once inside, the photons react with the photo-ionising agent TMAE [2], and produce electrons.

There is a central electrode in the chambers kept at a strong negative potential of –40kV. The produced electrons will thus drift towards the ends of the chambers, where sense wires are located (see figure 5.4). The hit wire number gives the Y coordinate of the photon, the Z coordinate is obtained from the drift time.

The electric field inside the chamber is inclined 50 mrad with respect to the vertical, to approximate the desired spherical shape of the sensitive region of the chambers (see lower right part of figure 5.4). There are 5 chambers, each with a width of 32.5 cm. They are mounted along an arc of 5 m radius in the Y direction.

In the WA94 setup, only particles that trace the silicon telescope, the RICH and the B chambers will be looked for. All these particles will produce rings at positive Y coordinates. The outermost chamber on the negative side was therefore not operated.

The chambers are filled with ethane, mixed with the photo-ionising agent TMAE. TMAE reacts violently with oxygen. The oxidation products absorb UV photons, and will thus degrade the detector efficiency if present. The chambers are therefore mounted in a closed volume filled with nitrogen. Oxygen is removed from all gases supplied to the RICH, and the oxygen content inside and outside the chambers is continuously monitored.

Furthermore, TMAE is a liquid at room temperature. The gas system in the chambers is therefore heated to 40°C. If TMAE were to condense inside the chambers, it would react with the plastic (G10) walls. Condensed TMAE cannot be removed from the walls, and the chambers would be rendered useless in case of contamination. The temperature of the gas in the chambers is thus closely monitored. If it should drop, the TMAE supply will be closed.

[2] Tetrakis(dimethylamino)ethylene

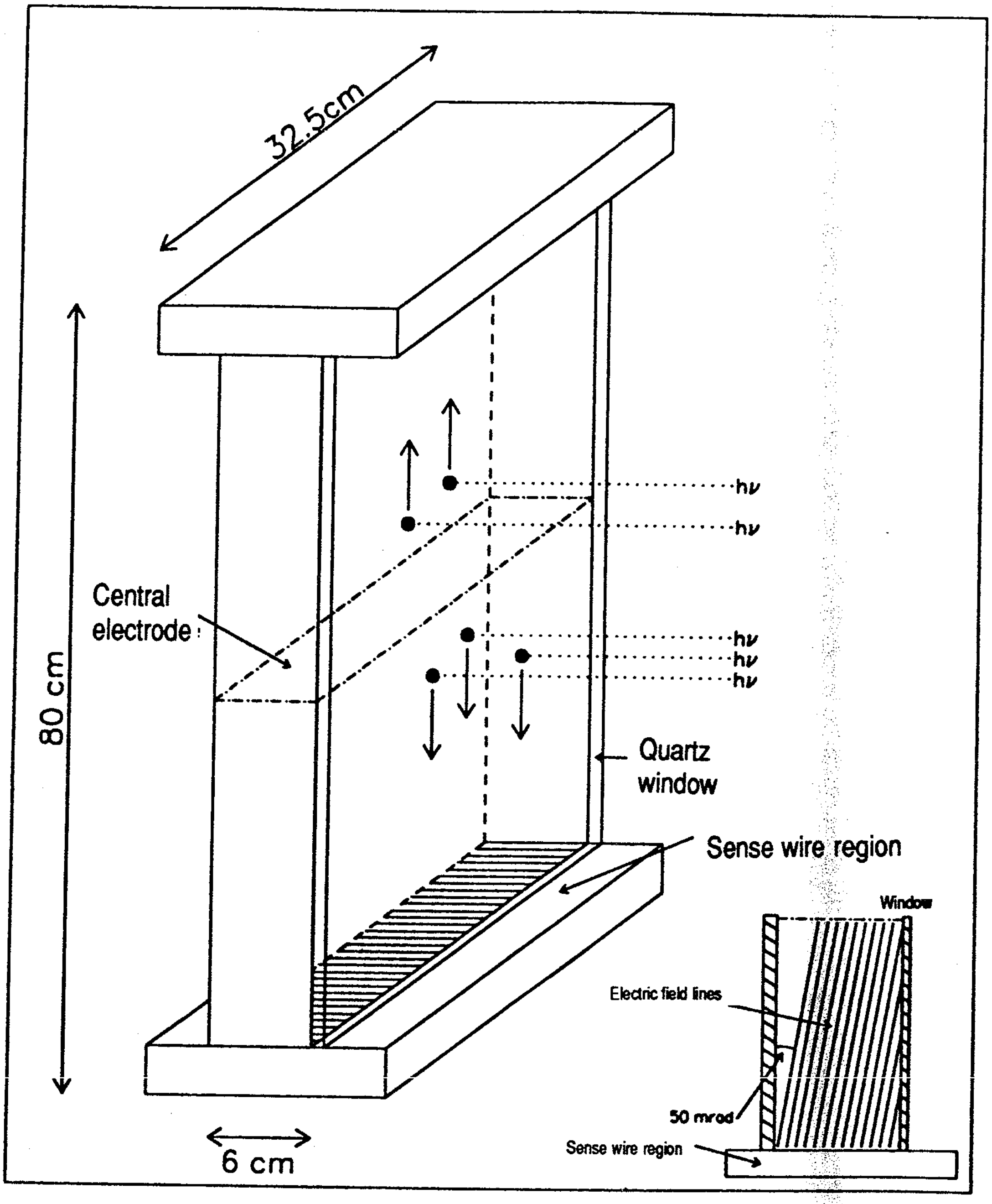

Figure 5.4: Design of a TPC chamber. The figure is taken from [Eng92]

5.4 RICH calibration

The Y and Z coordinates of the photons hitting the RICH TPCs are obtained from the wire number and drift time read from the chambers. To relate the information obtained from the RICH to an absolute coordinate system, several calibration constants are introduced. These constants are determined by detailed study of the RICH data.

A particle passing through the TPC will leave a signal in the chambers. The position obtained from the RICH can be related to track segments determined from the telescope and the B chambers, to obtain the exact RICH position.

The drift time in the RICH chambers, which is used to determine the Z coordinate, varies with the temperature. The exact values of the calibration constants must therefore be calculated at regular intervals, for example once per run.

The RICH mirrors may not be perfectly aligned. Slight rotations of individual mirrors may distort the rings produced by the Čerenkov photons. This effect is compensated by further calibration constants. The mirror calibration is done by searching well developed rings for assymmetries. Once the ring centre is known, this can be done by separate radial scans in different angular regions.

The calibration procedures are discussed in detail in [Eng92].

5.5 Simulations

The RICH is located downstream of the Omega magnet, as shown in the previous chapter. If the RICH were to be mounted there without any precautions, the high multiplicities of the heavy ion reactions would cause the RICH to be totally flooded. A simulation study has been carried out to figure out what measures to take to get managable multiplicities, without loosing too much of the desired signal.

5.5.1 Monte Carlo details

All simulations are performed by the purpose-made program RICHANA. This program reads event data produced by the event generator FRITIOF version 3.1 [Ben85, Ben86]. The particles in these events (sulphur on sulphur, 200 GeV·A, maximum impact parameter 2.5 fm) are traced through the field of the Omega magnet, then let into the RICH. The simulation program RICHANA may also implant one particle of given rapidity and transverse momentum into the background produced by FRITIOF. This 'signal' particle, chosen inside the acceptance region of the whole experimental setup, is marked with boldface dots in the figures.

Gamma conversion has been taken into account by simple redefinition. Ten percent of the gammas that reach the RICH entrance, have been converted into electrons at that point, conserving the original gamma momenta. Only gammas with energy above the pair production threshold have been allowed to produce electrons.

Short-lived particles (all except pions, kaons, nucleons, gammas, electrons and their anti-particles) are forced to decay at the target position, and their decay particles are traced through the field.

Table 5.1: Experimental setup

Item	Position (cm)		
	x	y	z
Target	-215	0	0
First Microstrip	-155	0	1.647
Last Microstrip	-75	0	7.176
Shield opening, lower left	820	20	50
Shield opening, upper right	820	90	90
RICH	1200	0	100

These simulations have furthermore been used to estimate the conditions in lead-lead collisions for the WA97 experiment. The background produced in lead-lead interactions have been approximated by adding ten sulphur-sulphur events produced by FRITIOF into one 'lead-lead' event. Only one 'signal' particle is implanted in the entire 'lead-lead' event. The 1000 sulphur-sulphur events available gave 100 'lead-lead' events. Percentages given at these high background events must therefore be considered as indications only, a one percent probability corresponds to one observed particle.

The positions of various detectors are given in table 5.1. In this table, the RICH position is defined as the position of centre of the TPC plane, or more accurately the centre of the upstream wall of the central TPC module.

5.5.2 Screening the mirror

To avoid having the beam pass through the chambers, the RICH is lifted 1 m in the Z direction. This protects the chambers from the incoming beam particles, but the reflected photon multiplicity is unaffected, since all parallel incoming rays will be focused onto the same point. This multiplicity is far too high to do reliable ring reconstruction.

Figure 5.5 shows the simulated TPC output from a 'raw' event where no further steps are taken to limit the particle multiplicity in the RICH. The ring produced by the particle that traced the telescope is shown by boldface dots.

Figure 5.6 shows the points where the Čerenkov photons hit the mirror in the same event. For simplicity, all the photons are produced at the RICH entrance in the simulation program, replacing the disc-shaped figures at the mirror by rings. This makes no difference at the TPC surface, due to the RICH principle discussed above. The rings shown at the mirror correspond to the circumference of the area where Čerenkov photons may be reflected. Note the different scale on the mirror and TPC pictures. The axes on the figures are given in units of centimetres in the RICH coordinate system.

The ring produced by the high-p_t particle is shown by boldface dots. In this picture it stands out more clearly than was the case in the TPC picture. Most particles produce rings close to the beam height. (Coordinates are shown in the RICH coordinate system. Since the RICH is raised 1 m with respect to the beam, Z=0 in the Omega system correspond to Z=−100 cm in the RICH system.)

The incoming charged particle pass through the mirror in the centre of the ring shown

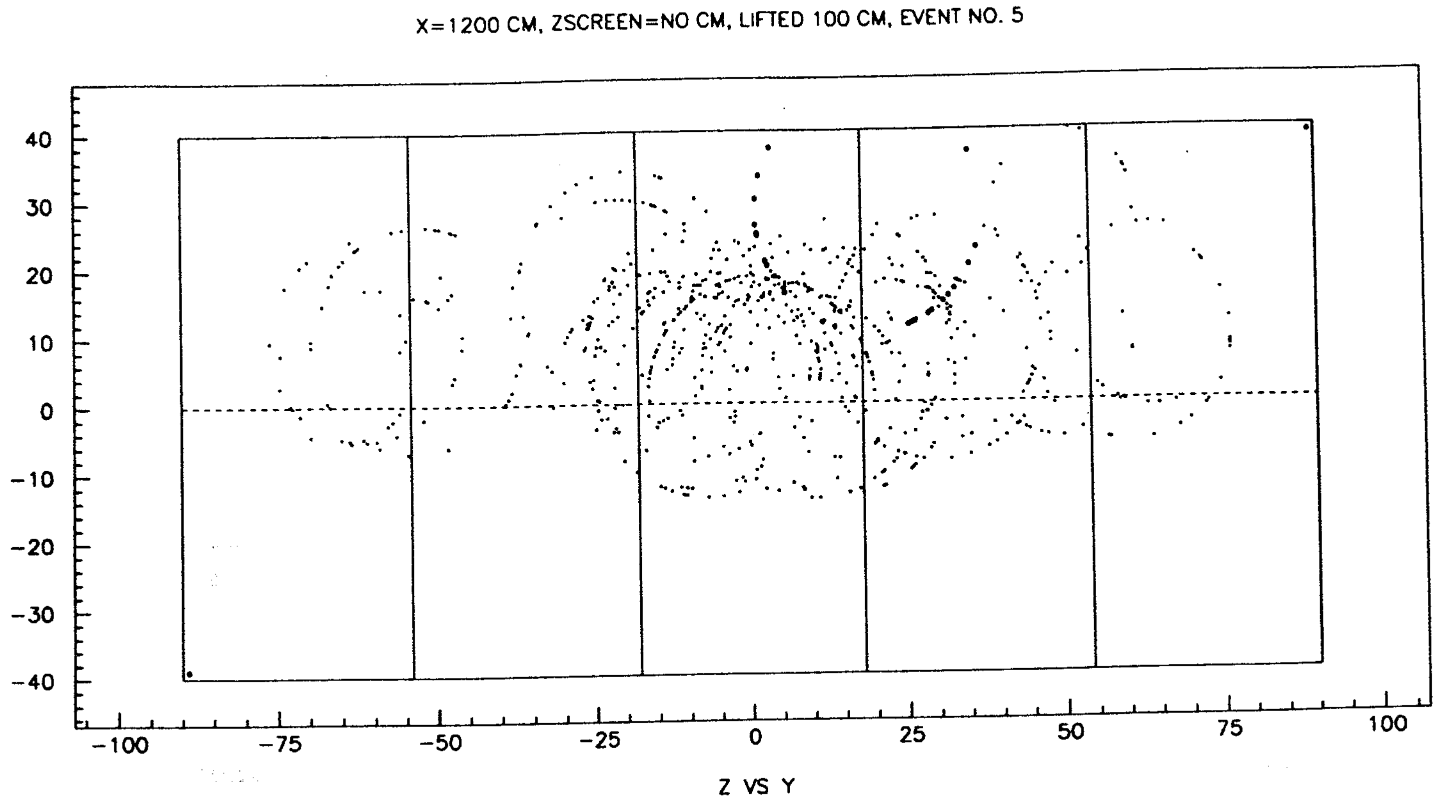

Figure 5.5: Simulated TPC images in 'raw' event. The RICH is lifted by 1 m, but no further steps have been taken to reduce the multiplicity. The 'good' ring is shown by boldface dots in the upper part of the figure.

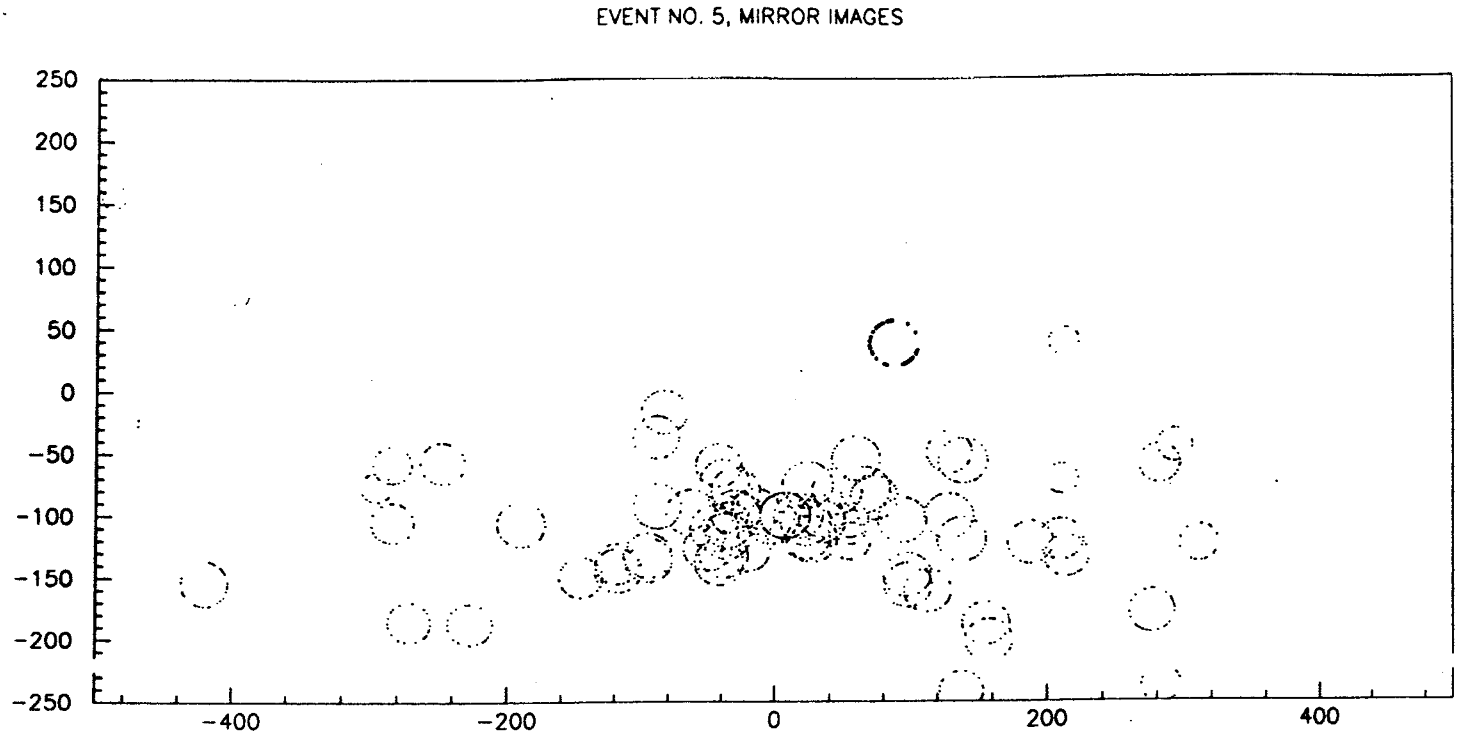

Figure 5.6: Simulated mirror images. Rings correspond to the circumference of the disc-shaped area of reflection.

on figure 5.6. Only Čerenkov photons, which fall in the visible to ultraviolet region, are reflected and returned towards the TPCs. These photons can be shielded by very simple means, for instance black paper or cloth.

Figure 5.7 shows the TPC images produced in the same event when the mirror was masked from Z=–5 cm downwards (corresponding to Z=95 cm in the Omega system). Now the signal is very clean, and a succesful reconstruction is very probable. Since the silicon telescope is tilted upwards, all the accepted high-p_t particles will hit the RICH mirror above this screen. The noise is thus reduced considerably, almost without affecting the signal.

5.5.3 Iron shield

When going to lead-lead interactions, the multiplicities are expected to increase considerably. Figure 5.8 shows TPC images in a simulated lead-lead event. The bold face ring corresponding to the 'good' particle would hardly be possible to reconstruct.

In order to reduce background levels further, an iron wall is placed between the Omega magnet and the RICH. A small opening in the wall allow particles in the acceptance region of the telescope to pass through.

This shield prevents beam particles from passing the RICH, and will also reduce the background produced by particles coming from the target. Assuming that all particles hitting the 2 m thick iron wall are stopped there, the simulated TPC picture is as shown in figure 5.9. Although the picture is relatively clean, the background levels in the region

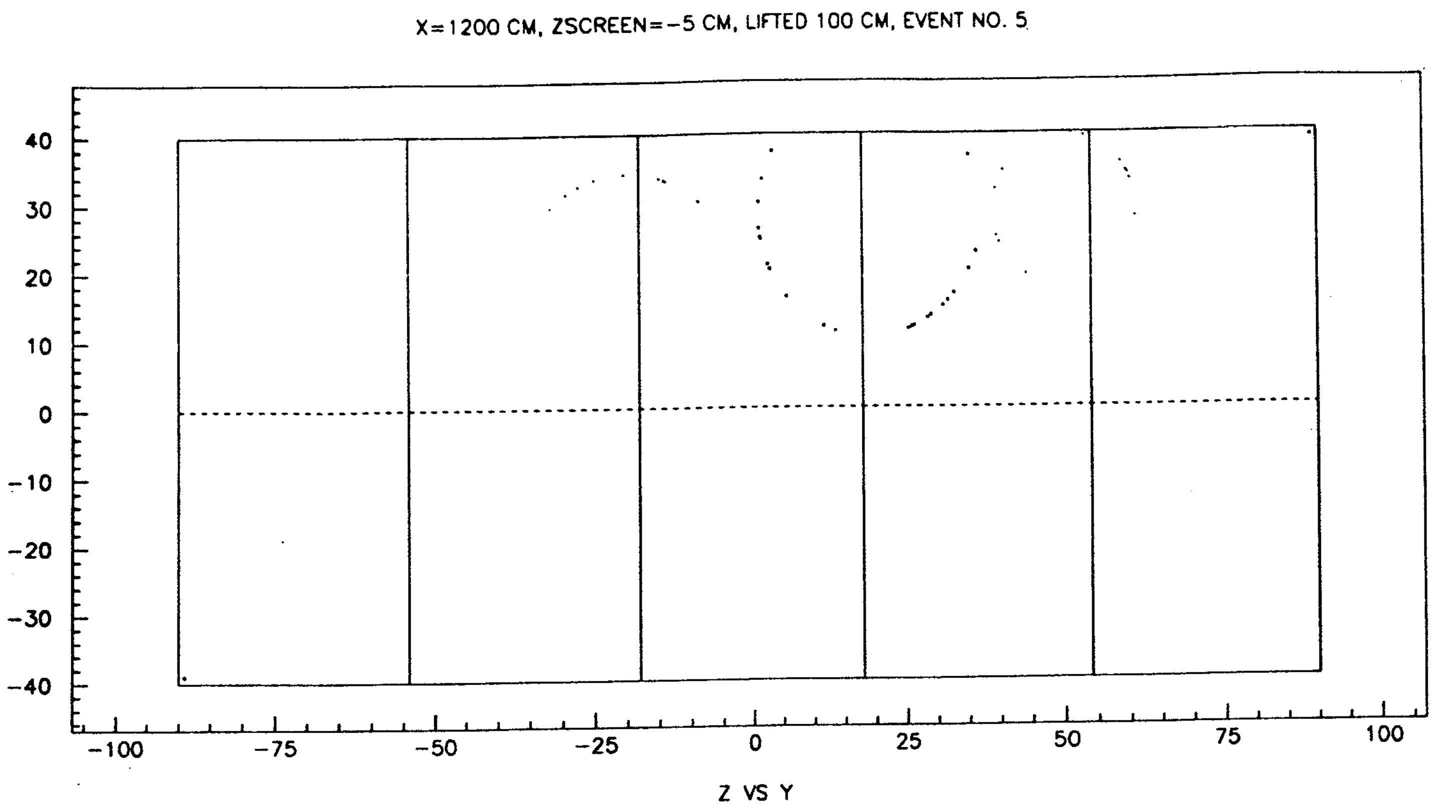

Figure 5.7: Simulated TPC images with a screen at the RICH mirror from Z=–5 cm downwards.

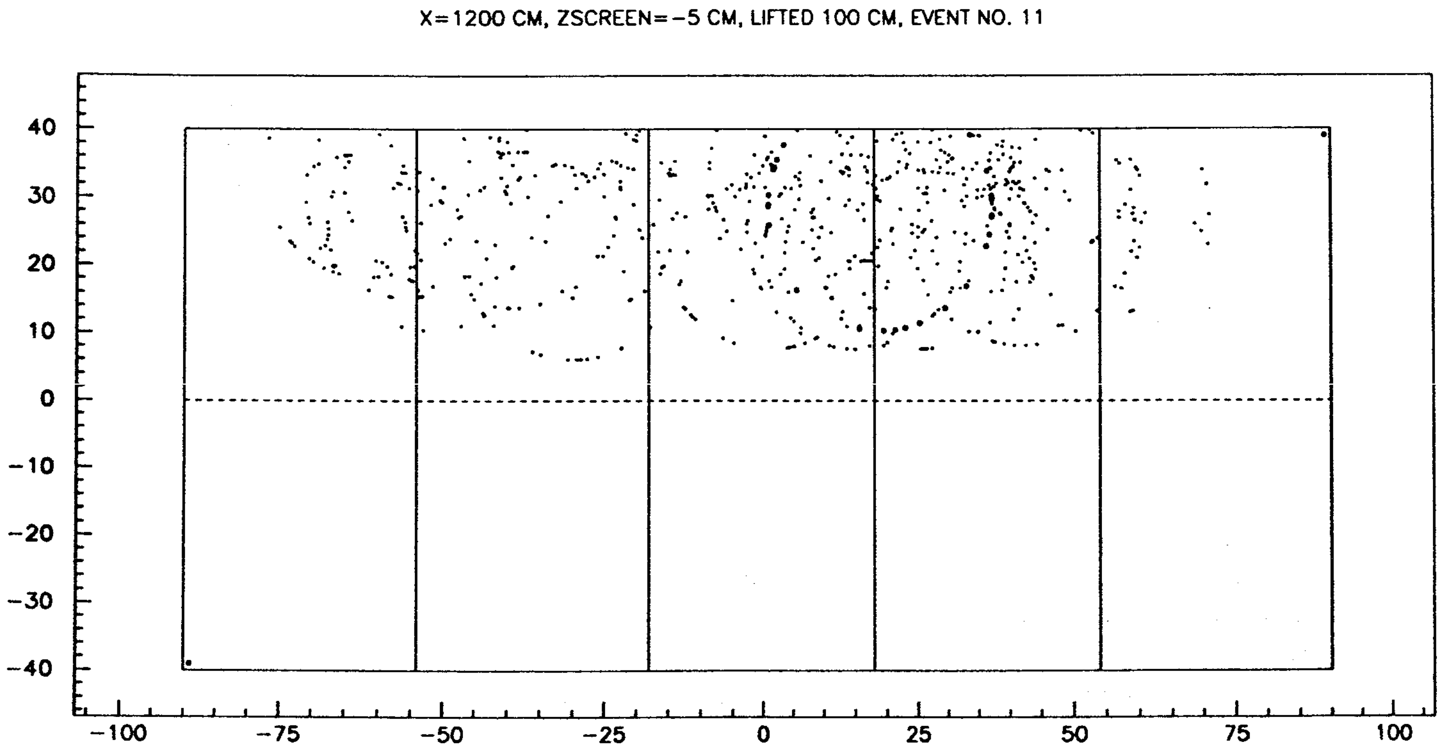

Figure 5.8: Simulated TPC images in 'lead-lead' event. The RICH mirror is screened from Z=–5 cm downwards.

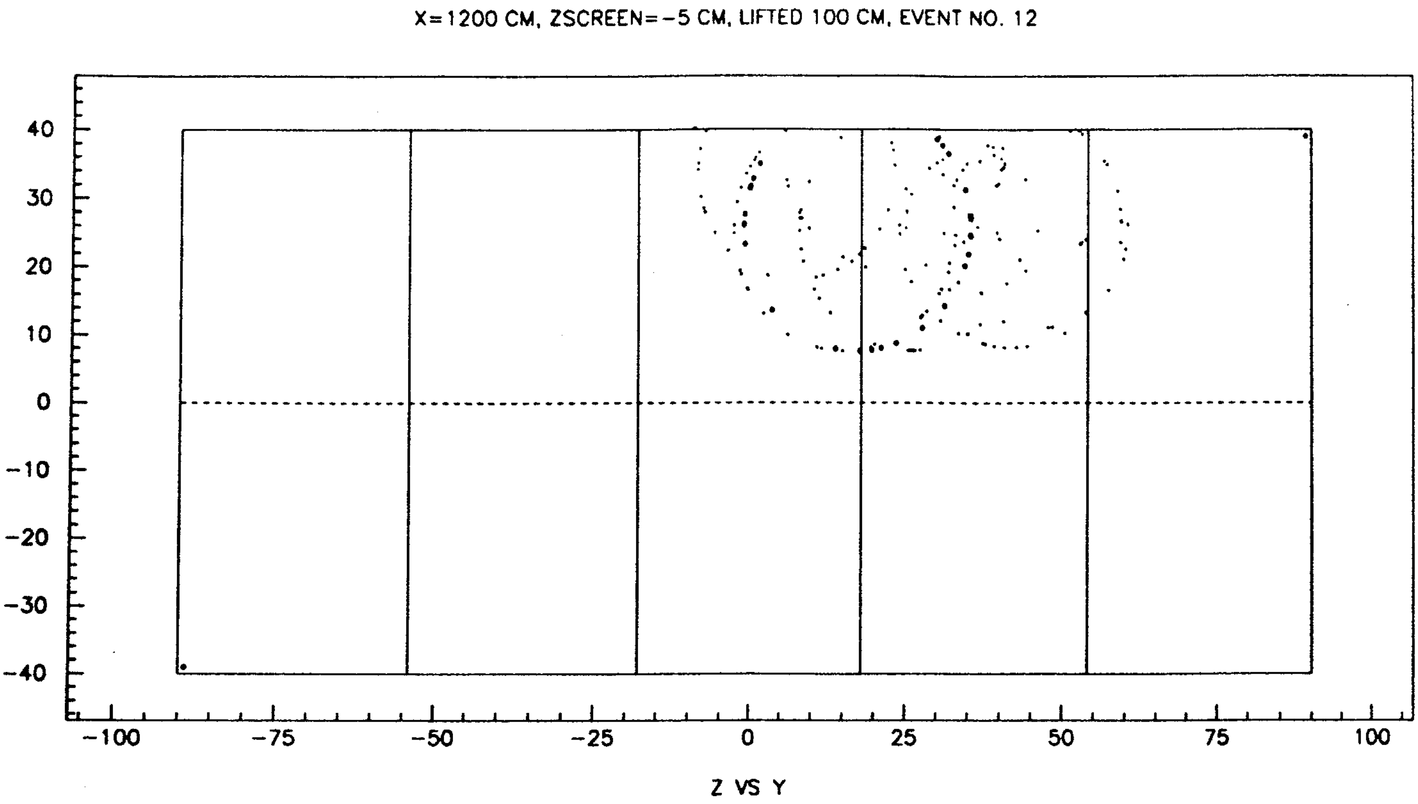

Figure 5.9: Simulated TPC images in 'lead-lead' event. The iron wall between the Omega magnet and the RICH is included. The RICH mirror is screened from Z=–5 cm downwards.

where the signal is expected is a bit too high to make identification by absence of signal reliable. A GEANT study on how to reduce this background is in progress [Hol93].

5.5.4 Geometric acceptance

The geometric acceptance of the detector setup is constrained by the end plane of the microstrip telescope. Figure 5.10 shows the acceptance for protons of different rapidities and transverse momenta. All the numbers in the figure are percentages. The line in the lower left corner limits the region where negative proton identification can be applied. Below this line the signal produced by a kaon will be too weak to allow reliable reconstruction (less than 50% of the photons produced in a β=1-ring would be emitted). This corresponds to a kaon momentum of 17 GeV/c. The dashed line somewhat above gives the Čerenkov threshold for protons. Protons near threshold will emit only a few Čerenkov photons while traversing the radiative medium, making negative identification necessary in a greater region than indicated by the threshold line.

Figure 5.11 shows the impact point on the iron shield of the particles that pass through the end plane of the microstrip telescope. Since only these particles will be of further interest, this plot indicates where to make the opening in the shield. The exact positions of the dots correspond to the positions of the test particles used in the simulations.

The multiplicities in the RICH TPCs in the 'lead-lead' events can be reduced by moving the left edge of the shield opening to higher Y values. A shield setting at Y=50 cm

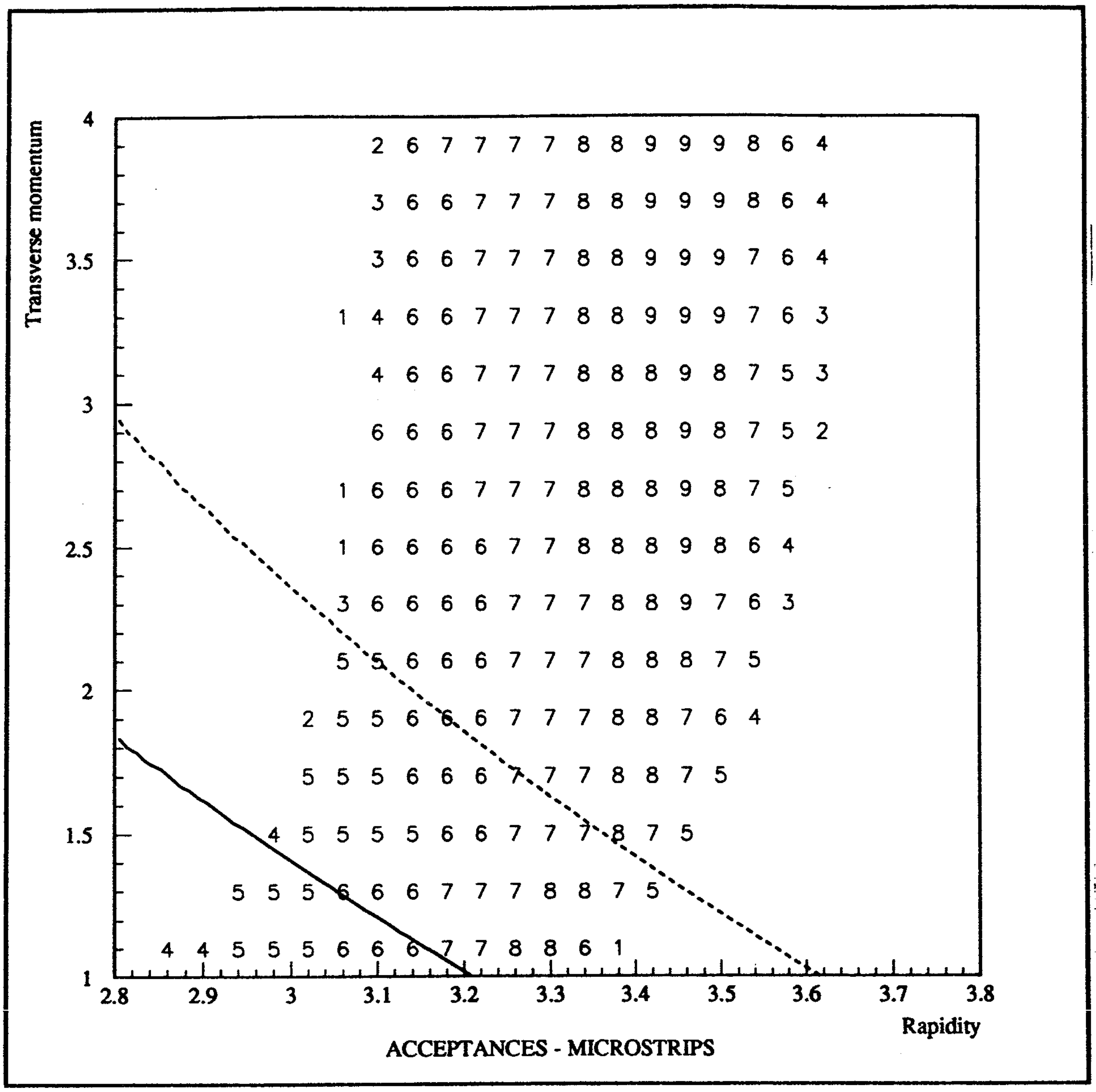

Figure 5.10: Telescope acceptances (given as percentages)

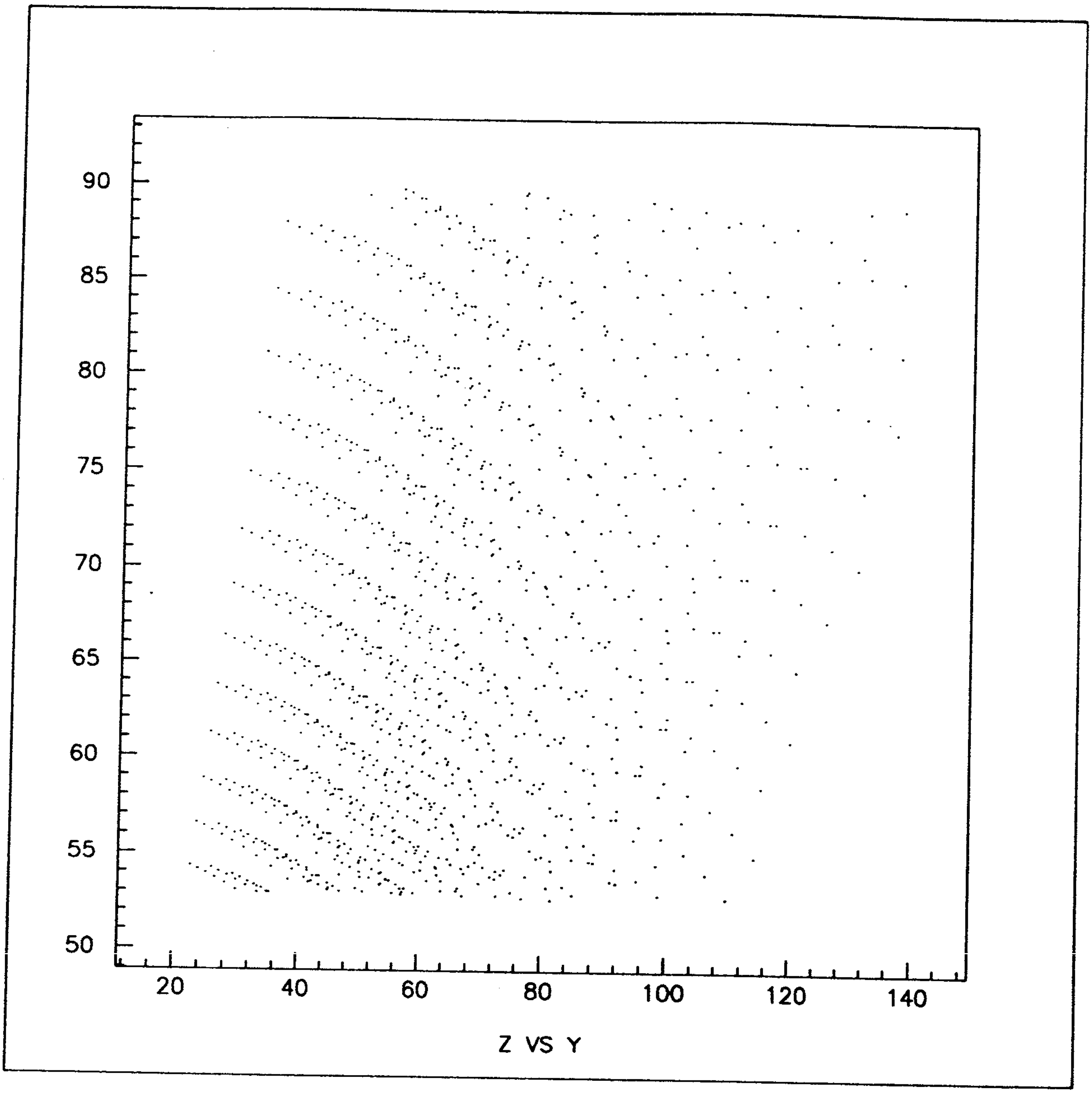

Figure 5.11: Shield impact point of accepted particles

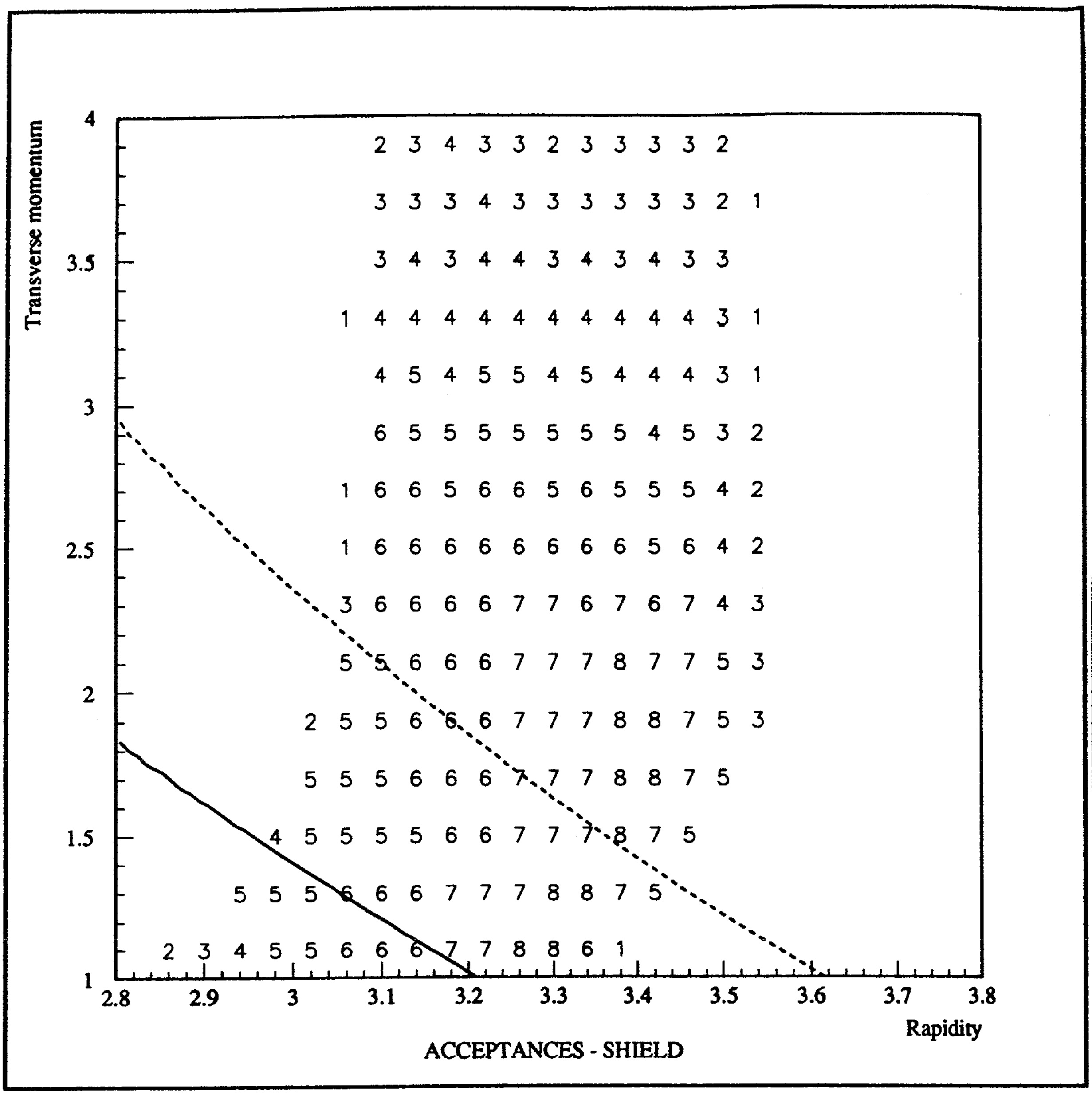

Figure 5.12: Acceptances with shield opening at Y=50 cm.

reduces the acceptance in the very high p_t region, (above p_t= 3 GeV/c), but the number of protons produced in this region is expected to be very small. The acceptances with the modified shield are shown in figure 5.12. All numbers are given as percentages.

5.5.5 Radial scans

The signal will be reconstructed by a radial scan in the data read from the RICH TPCs. The positions of the particles we want to identify are known from the microstrip telescope and from the B chambers. The position of the centre of the produced ring at the RICH TPCs can thereby be calculated.

The radius of a ring produced by a pion, kaon or proton at the same rapidity and transverse momentum differ by approximately 3 cm. As rapidity and transverse momentum are known from the microstrip telescope, the appropriate ring size for each of the three particle species may be calculated. A scan with a total width of 1 cm is then performed in the data, centered around the calculated ring size. The number of counts in this area will be considered as 'signal'. A wider scan is performed to calculate the appropriate background level.

As we only want to identify the particle, the exact peak height is of no importance. We want to acknowledge a ring as 'identified' if the signal exceeds the background by a fixed number of counts. If no ring is found, the particle is classified as a proton, by negative identification.

This scheme introduces two main sources of error. Either the signal may fluctuate down to the background level, in which case a real pion will be counted as a proton ($\pi \rightarrow$ p). On the other hand, the background may fluctuate above the fixed level, thereby faking a signal, and causing a real proton to be counted as a pion (p $\rightarrow \pi$). The same may of course happen to kaons.

The probability of each of these errors has been estimated by Monte Carlo calculations. Increased background levels have been achieved by adding the background produced by several FRITIOF events, as described in section 5.5.1.

Pions and kaons of rapidity y=3.2 and transverse momentum p_t= 1.5 GeV/c are implanted into the sulphur and 'lead' events. Then a radial scan is performed, as discussed above. The probability for the signal to fluctuate down to the background is calculated by the Poisson expression [ppd90]

$$p = e^{-s} \sum_{j=0}^{b+i} \frac{s^j}{j!} \tag{5.2}$$

where p is the probability in question, s is the size of the signal, b is the size of the background and i is the threshold by which the signal is required to exceed the background. The probability for fake signals is obtained from a radial scan in background events, where no particle has been implanted. All probabilities are given as percentages.

The results are given in table 5.2. A succesful reconstruction of sulphur-sulphur events seems very probable. A threshold of 5 or 6 gives probabilities below 1% for all the possible misidentifications. In the 'lead-lead' events the risk of misidentification is at best at the 5% level. To obtain more reliable identification, either the background must be reduced, or more sophisticated pattern recognition algorithms must be used.

A similar analysis has been done using experimental data from the 1992 run of WA94 as background. The events were all taken with freon as radiator in the RICH. The RICH data are not calibrated. 'Lead-lead' events were generated by adding 10 sulphur-sulphur events. One particle (pion or kaon) with rapidity y=3.2 and transverse momentum p_t= 1.5 GeV/c was added to each event. The results shown in table 5.3 are based on 1000 S+S events, and 500 'Pb+Pb' events (originally 5000 S+S events). The observed experimental background is larger than the simulated one. This can be due to spurious particles in the RICH, originating from rescatterings in the detector setup.

Some examples of radial scans, with their corresponding TPC images, are shown in figures 5.13 and 5.14. Both events are 10-fold background ('lead-lead' events) with an implanted kaon, shown in bold face in figure 5.13. The reliability of the reconstruction depends on the distribution of rings in the TPCs, not directly on the TPC multiplicity.

Table 5.2: Radial scans, concrete shield included. All probabilities given as percentages.

Sulphur-sulphur events

Background + n	$\pi \rightarrow p$	$K \rightarrow p$	$p \rightarrow \pi$	$p \rightarrow K$
n = 1	0.10	0.10	9.4	8.9
n = 2	0.10	0.10	5.3	3.1
n = 3	0.10	0.11	2.6	1.4
n = 4	0.10	0.19	1.1	0.9
n = 5	0.10	0.64	0.6	0.6
n = 6	0.10	1.7	0.5	0.2
n = 7	0.10	3.4	0.4	0.2
n = 8	0.13	6.6	0.2	0.1
n = 9	0.35	11.3	< 0.1	0.1
n = 10	0.77	17.8	< 0.1	0.1

'Lead-lead' events

Background + n	$\pi \rightarrow p$	$K \rightarrow p$	$p \rightarrow \pi$	$p \rightarrow K$
n = 1	0.10	0.14	46	38
n = 2	0.10	0.25	33	23
n = 3	0.10	0.53	17	15
n = 4	0.11	1.1	15	9
n = 5	0.15	2.2	6	5
n = 6	0.23	4.0	5	4
n = 7	0.42	6.7	4	2
n = 8	0.76	10.5	2	2
n = 9	1.4	15.6	1	2
n = 10	2.3	21.9	1	2

Table 5.3: Radial scans, experimental background. All probabilities given as percentages.

Sulphur-sulphur events

Background + n	$\pi \rightarrow$ p	K $\rightarrow$ p	p $\rightarrow \pi$	p $\rightarrow$ K
n = 1	0.10	0.11	19.3	16.2
n = 2	0.10	0.13	9.5	7.4
n = 3	0.10	0.18	5.8	3.8
n = 4	0.11	0.37	3.1	3.1
n = 5	0.12	0.97	2.2	1.7
n = 6	0.14	2.1	1.5	1.4
n = 7	0.26	4.2	1.0	1.2
n = 8	0.59	7.5	0.8	0.6
n = 9	1.3	12.4	0.7	0.5
n = 10	2.4	19.0	0.3	0.2

'Lead-lead' events

Background + n	$\pi \rightarrow$ p	K $\rightarrow$ p	p $\rightarrow \pi$	p $\rightarrow$ K
n = 1	0.14	1.3	56.8	44.6
n = 2	0.19	2.1	47.4	35.2
n = 3	0.29	3.1	40.2	26.8
n = 4	0.47	4.6	31.0	20.0
n = 5	0.78	6.7	25.8	15.4
n = 6	1.2	9.4	20.6	12.6
n = 7	2.0	12.9	16.0	11.4
n = 8	3.1	17.2	13.6	9.4
n = 9	4.6	22.1	12.4	7.6
n = 10	6.5	27.8	8.8	6.2

The number of Čerenkov photons is higher in the lower event of figure 5.13, but the noise level in the radial scan is higher in the upper event (see figure 5.14).

5.6 RICH vs. C1

The Čerenkov detector C1 used in the WA85 1990 run (see section 3.2.4) was intended to identify protons and antiprotons by absence of signal. The detector was first used in the 1989 proton run, where it was found to be 94±9 % efficient [Bar93]. The electronic noise was about 1 noise signal per 4 events.

This performance should indicate usefulness of the C1 detector, but during the 1990 sulphur run it turned out to be too many signals in C1 to do negative identification.

Although the principle of negative identification remains, there is a number of reasons to believe that the RICH will do better than C1:

1. The RICH gives a more specific signal than does C1. Once the predicted ring centre is calculated from the tracks in the telescope and B chambers, the absence of signal is only required in a region close to the predicted ring. (A ring produced by a rescattered particle somewhere else in the TPC plane doesn't hurt the signal much.)
2. The screening of the RICH mirror removes much of the undesired signal, even if Čerenkov photons are produced by some traversing charged particle.
3. The RICH is much better shielded than was C1. The iron wall stops most of the particles that could otherwise reach the detector through secondary interactions or pair production.

5.7 On-line monitoring

Several programs are needed to monitor the RICH operation. All these programs are modified versions of programs developed by the WA89 collaboration [Eng92a].

The RMON program runs continuously and monitor physical parameters of the RICH operational environment, such as pressures, temperatures and oxygen contents in the gases in the RICH and in the TPC chambers. If central values fall outside predefined limits, alarms are given. If the most critical parameters (temperatures, oxygen contents) fall outside some other 'final' limits, the TMAE supply to the chambers will be turned off automatically.

The parameters measured by RMON are also used in the calibration of the RICH data. They are therefore written to tape at regular intervals.

The RICHON program can be used to estimate the quality of the RICH data. Wire maps and time distributions are histogrammed in a number of events defined by the user. This program is run at least once per shift, and the result is compared to template histograms available in the control room.

Finally the CINEMA program is used to plot TPC images on line. This program is run at regular intervals to ensure that everything looks 'normal'.

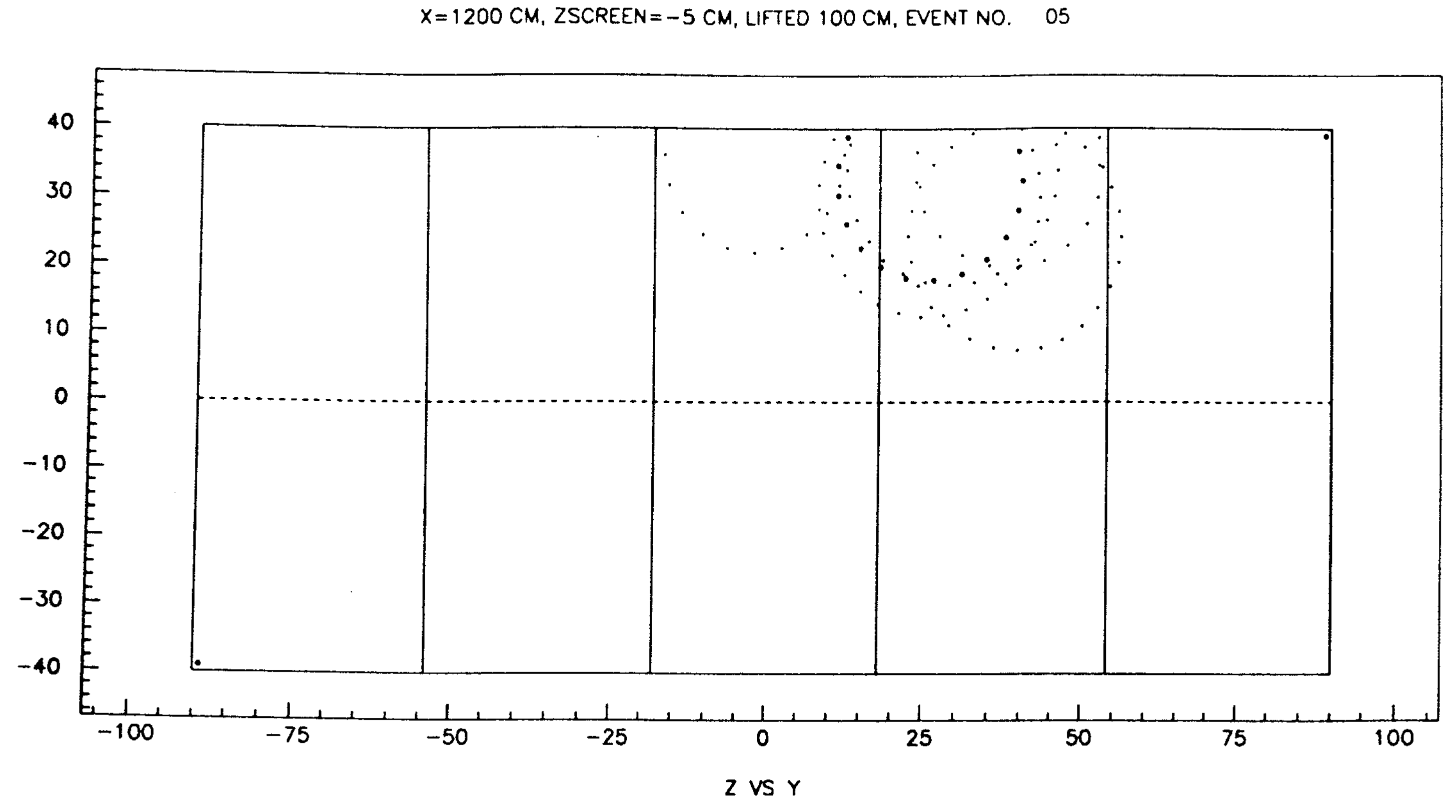

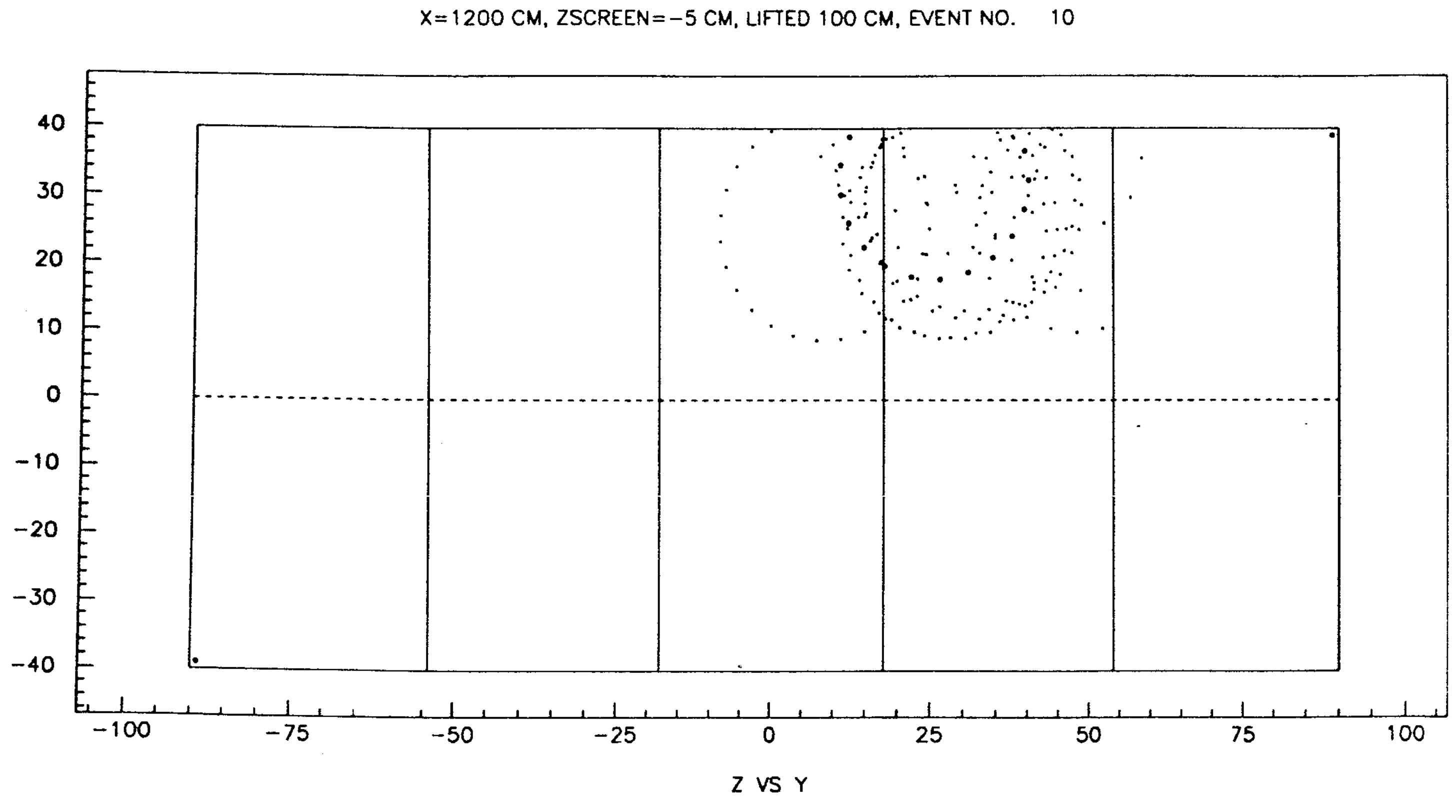

Figure 5.13: TPC images of 'lead-lead' events with implanted kaon

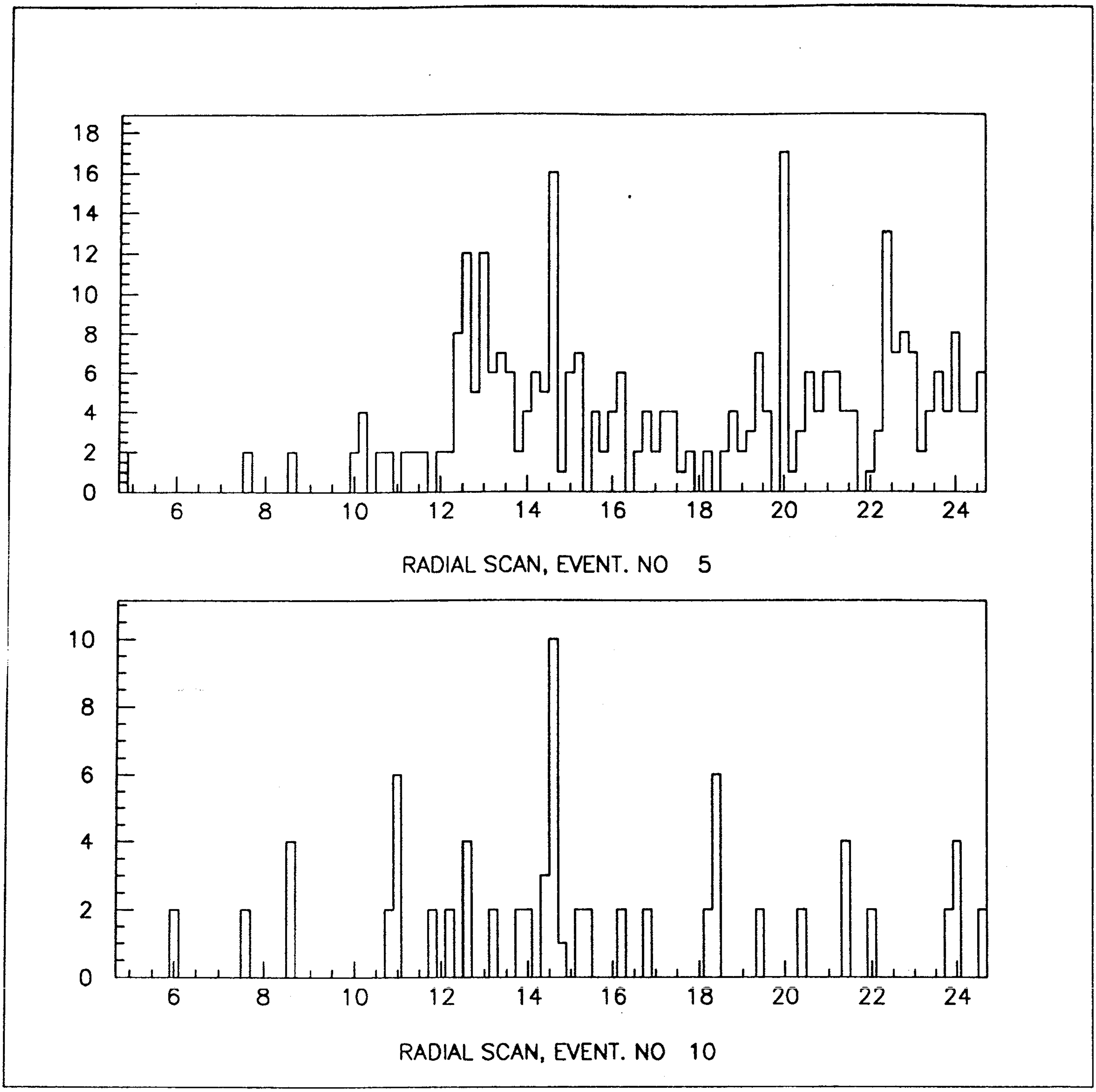

Figure 5.14: Radial scans. The implanted kaon produce a ring radius of 14.6 cm

5.8 B Chambers

To make a reliable radial scan in the RICH output, the ring centre must be known rather precisely. This position can be calculated from information obtained in the silicon telescope, but since the distance between the end of the telescope and the RICH is large (12 m to the TPCs, 18 m to the mirror), the uncertainty would be significant.

This uncertainty can be reduced by measurements of particle coordinates close to the RICH position. A set of wire chambers is therefore located behind the RICH, its position is adjusted so particles that trace the telescope should also pass the sensitive region of the chambers. When the tracks observed in the telescope and the B chambers are combined, a reliable determination of positions inside the RICH should be possible.

The B chamber package is one of the general detectors of the Ω facility. It is normally located inside the magnet, ahead of the A chambers. In WA94 the whole setup was moved behind the RICH, without other modifications.

The B chamber setup consists of 8 chambers, each with two wire planes. There are two different kinds of chambers, UY and VY. U and V planes are rotated 10.14° with respect to the vertical, as discussed in section 3.2.2. There are four chambers of each type in the package, placed alternatingly. The sequence of planes is thus UYVYUY etc.

Each wire plane contains 768 anode wires, with an internal spacing of 2 mm. The first chamber (B1) is positioned at X=1790 cm, the last chamber (B8) is placed at X=1832 cm. All planes have a sensitive region of 182×95 cm^2.

5.8.1 Track reconstruction

The magnetic field is negligible at the position behind the RICH. Thus the B chamber tracks are linear. Track finding routines have been developed in the framework of TRIDENT version 5.04. This program package will be used for all track finding in WA94.

First the Y, U and V projections are considered separately. Raw data points are collected into linear track projections. A minimum of 5 points is required in the Y projection, 3 points are required in the U and V projections. One raw data point can be assigned to one track projection candidate only.

Y coordinates can be obtained from U and V coordinates by the relation

$$Y = \frac{U+V}{2\cos\alpha} \tag{5.3}$$

where α is the inclination angle (10.14°). Similarly, the linear track parameters in the Y direction can be calculated from parameters in the U and V directions by

$$A'_Y = \frac{A_U + A_V}{2\cos\alpha}; \quad B'_Y = \frac{B_U + B_V}{2\cos\alpha} \tag{5.4}$$

as a linear track can be parametrised by Y = A·X+B. All possible combinations of U and V track projection candidates are made, and the Y′ parameters obtained are compared to the Y track projection candidates found directly from the Y planes. The best candidate is found by least squares fit, and the three projections are assigned to a track. The track parameters in the Z direction can then be found by the relations

$$A'_Z = \frac{A_U + A_V}{2\sin\alpha}; \quad B'_Z = \frac{B_U + B_V}{2\sin\alpha} \tag{5.5}$$

The same procedure is repeated for the remaining projection candidates. A track projection can be assigned to one track only. If there are different numbers of track projection candidates in the Y, U and V directions, the maximum number of physical tracks is given by the smallest number of projection candidates.

Finally, a three-dimensional track fit is done on the selected data points, to obtain the optimal track parameters.

5.9 Experimental data

5.9.1 Čerenkov rings

Experimental data with freon radiator in the RICH were taken in April 1992. The analysis of these data is still in its early phase, but some initial points will be discussed below.

So far track reconstruction is available for the B chambers only. These tracks will later on be merged with tracks from the telescope, when the telescope tracking routines are completed.

The calibration of the RICH needs reliable tracking. So far, the basic calibration constants found by WA89 are used as a first approximation.

Figure 5.15 shows an experimental TPC image from a sulphur on sulphur event. The charged particle traced through the lower right TPC module in this event, leaving a cluster of data points in the upper right corner of the lower right TPC module. The cross close to this cluster is the predicted particle impact obtained from a B chamber track. The cross in the upper part of the picture gives the predicted centre of the ring of Čerenkov photons produced by this charged particle. There is some noise in this part of the image, but parts of a ring structure can clearly be seen. A radial scan based on this ring centre is shown in figure 5.16. Calibration will hopefully make the radial scans cleaner, but there is a clear peak corresponding to the ring radius.

5.9.2 Track origin

As the magnetic field lines are in the Z direction (i.e. particles are bent in the XY plane), a linear extrapolation of the tracks in the XZ plane should intersect the beam axis close to the target if the particle in question originates there.

A sample of tracks was taken from the 1992 run; the first 3325 events from run 3924, with a level 1 trigger (tracks in the B chambers were not required). Track reconstruction is done in the B chambers only. A track is accepted if it produces hits in at least half of the chamber planes (4 Y planes, 2 U planes and 2 V planes).

A linear extrapolation of the tracks in the XZ plane is shown in figure 5.17. The distribution is rather wide, but there is a high number of counts close to the target. The track reconstruction is less accurate in the Z direction than in the Y direction, due to the geometry of the wire planes. In a simulation study tracks were produced at the target and fed into the B chambers. When reconstructed, even these tracks show a rather wide distribution (figure 5.18).

Some of the tracks in figure 5.17 cannot come from the target. The multiplicity of tracks in the B chambers is also higher than expected from simulation studies. Most of

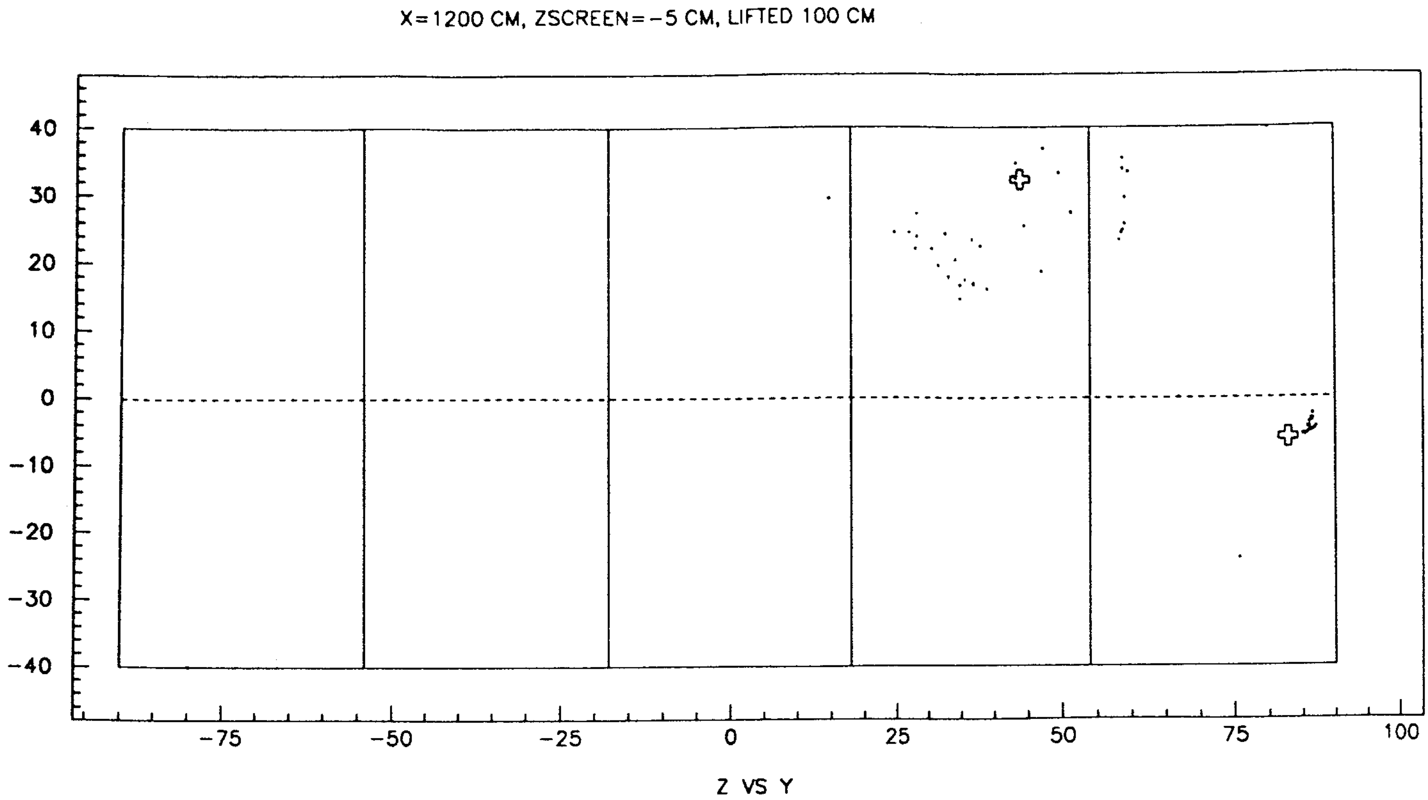

Figure 5.15: Experimental TPC images from WA94 1992 run.

these tracks probably originate from pair production and rescatterings. The events in the sample were searched for tracks having a common space point. The X position of the common space point was plotted. There is a large peak at the position of the mirrors and rear body of the RICH, corresponding to a significant pair production there.

Other noise tracks are probably produced in interactions between beam particles and the support of the silicon telescope. Detailed simulation studies to estimate the amount and significance of such scatterings are carried out by Alv Kjetil Holme and Guttorm Undheim [Hol93].

5.10 Conclusions

The initial analysis of the 1992 data seems to confirm that the RICH provides clean pictures even in heavy ion collisions. No real problems were encountered in RICH operation during the run. With freon radiator enough Čerenkov photons are emitted to produce well developed rings.

All the measures discussed in this chapter were taken to reduce the multiplicity in the RICH. In the sulphur-sulphur reactions of WA94, this seems sufficient to identify rings by simple radial scans, and to identify protons by absence of signal.

Noise levels are higher in the lead-lead collisions of WA97. Simulations indicate an uncertainty in the particle identification at the 5% level. This figure can be improved by better shielding of the RICH to reduce the background further. This would also limit the acceptance region of the RICH/B chamber setup. Alternatively, more sophisticated reconstruction algorithms can be used to identify rings in the RICH data.

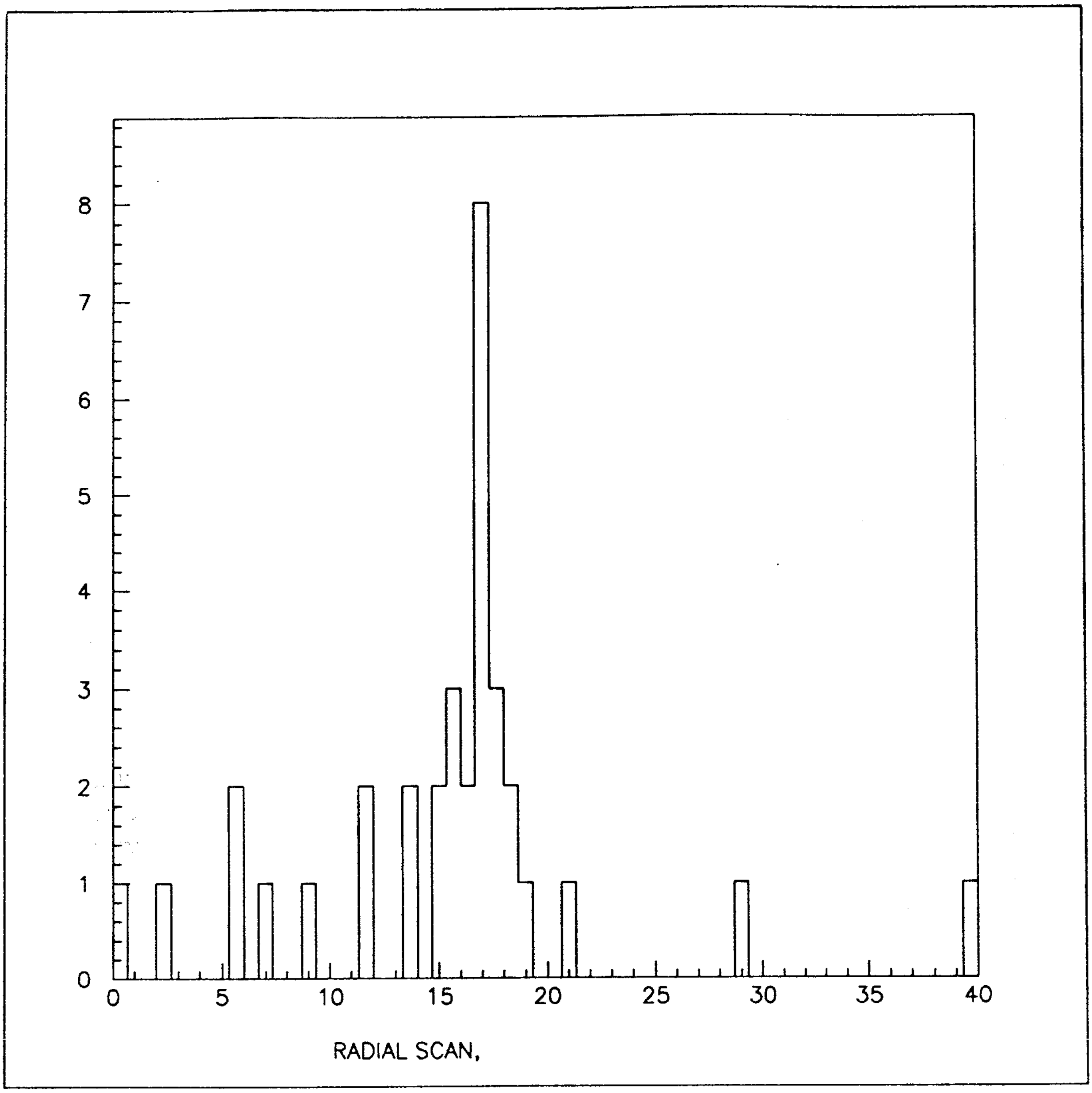

Figure 5.16: Radial scan from WA94 1992 run.

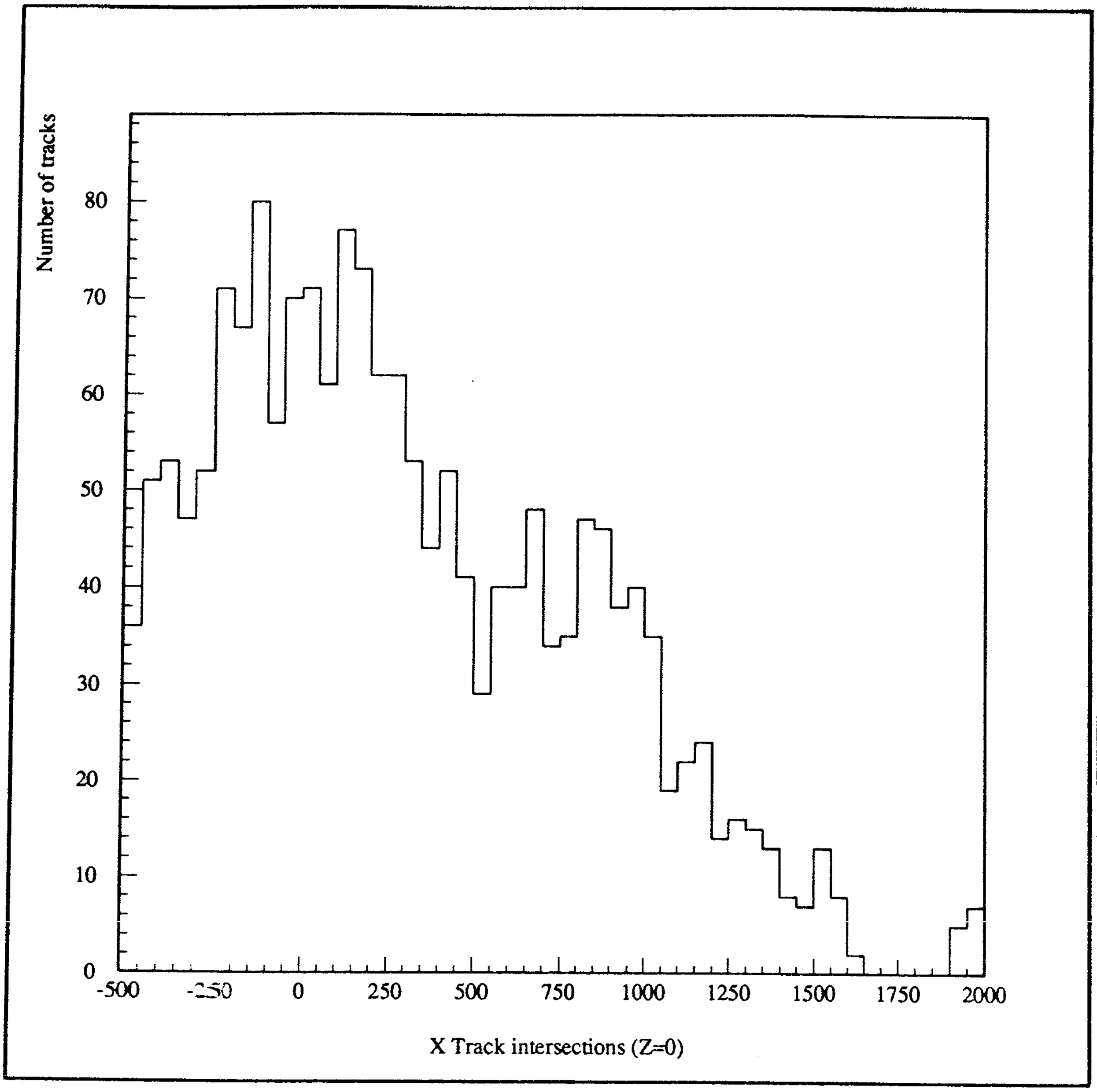

Figure 5.17: B chamber track intersection with Z=0 plane. The target position is at X=–215 cm.

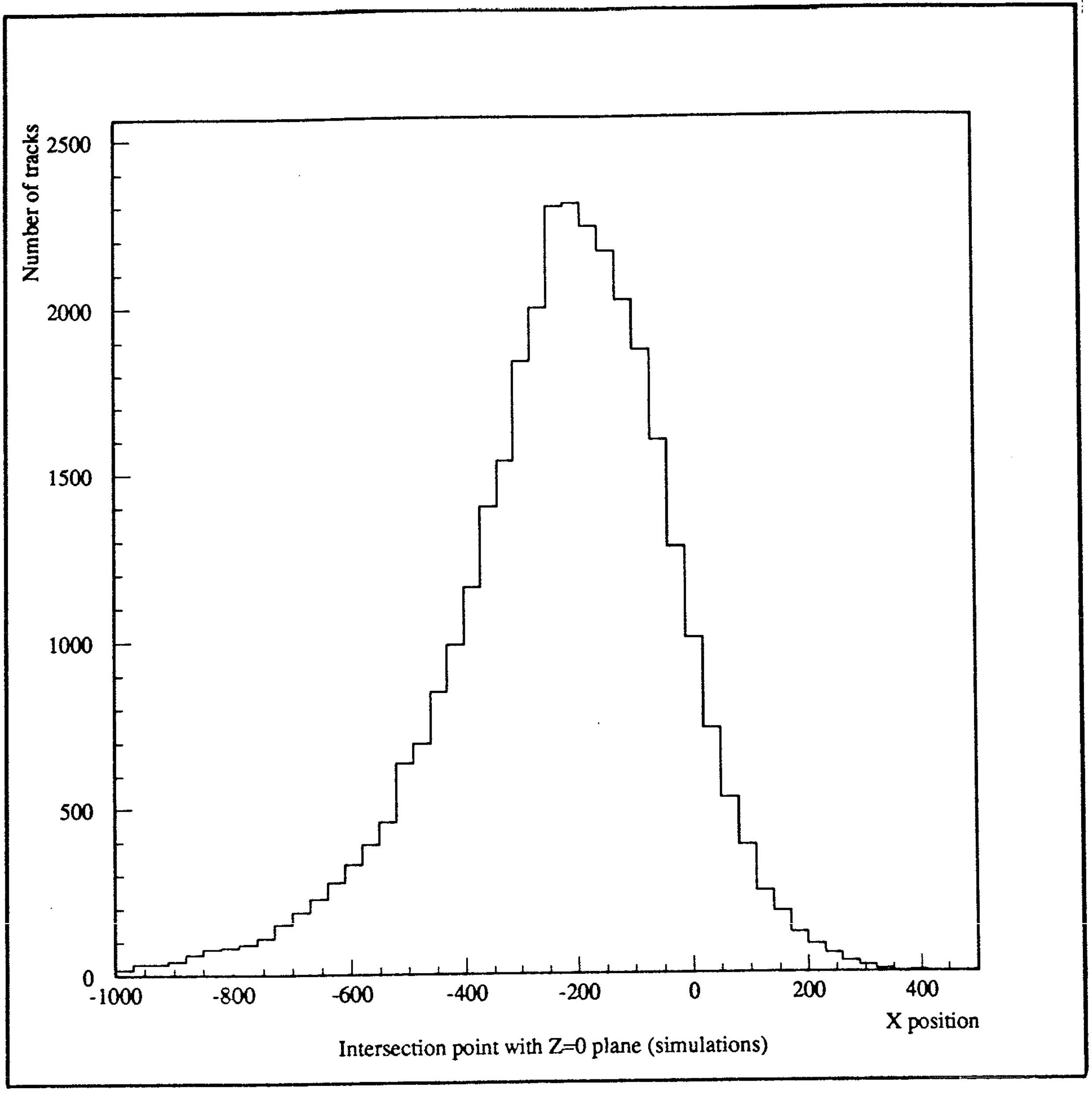

Figure 5.18: Track intersection with Z=0 plane for simulated tracks produced at the target (X=–215 cm)

Chapter 6

The WA97 Experiment

The WA97 collaboration will take data when the lead beam becomes available at the CERN SPS. The larger volume of dense matter produced in lead-lead interactions make formation of a quark gluon plasma more probable than in the smaller sulphur-sulphur or sulphur-tungsten systems. The larger volume of the system will also make the life time of the central hot zone longer, giving more time for equilibration.

On the other hand, the multiplicity of produced particles in the collisions will increase considerably, making it a challenge to reconstruct individual tracks in a reliable way, and to avoid flooding of the individual detectors. A QGSM simulation [Ame90], a string model including rescattering, shows average multiplicities of charged particles per event around 300 in sulphur-sulphur collisions, 700 in sulphur-tungsten collisions and 3000 in lead-lead collisions.

The WA97 collaboration will carry forward the work done by the WA85 and WA94 collaborations, and investigate the production of strange baryons and antibaryons in the realm of collisions with the heaviest ions available.

6.1 Data taking

The WA97 experiment [Arm91] will use the lead beam with an energy of 160 GeV per nucleon, scheduled to be available in the CERN SPS towards the end of 1994. Several tests of the apparatus are planned during WA94 proton runs in 1993 and early 1994.

6.2 Apparatus

The layout of the WA97 experiment is shown in figure 6.1. It is an improved version of the WA94 setup, with several modifications to handle larger multiplicities. In particular, two-dimensional readout is introduced in many of the tracking detectors.

6.2.1 The multiplicity detector

The charged particle multiplicity is measured in a silicon microstrip array placed close to the target. The detector consists of three arms, two of them directed in the positive and negative Y directions, and the final one in the negative Z direction. The arms are

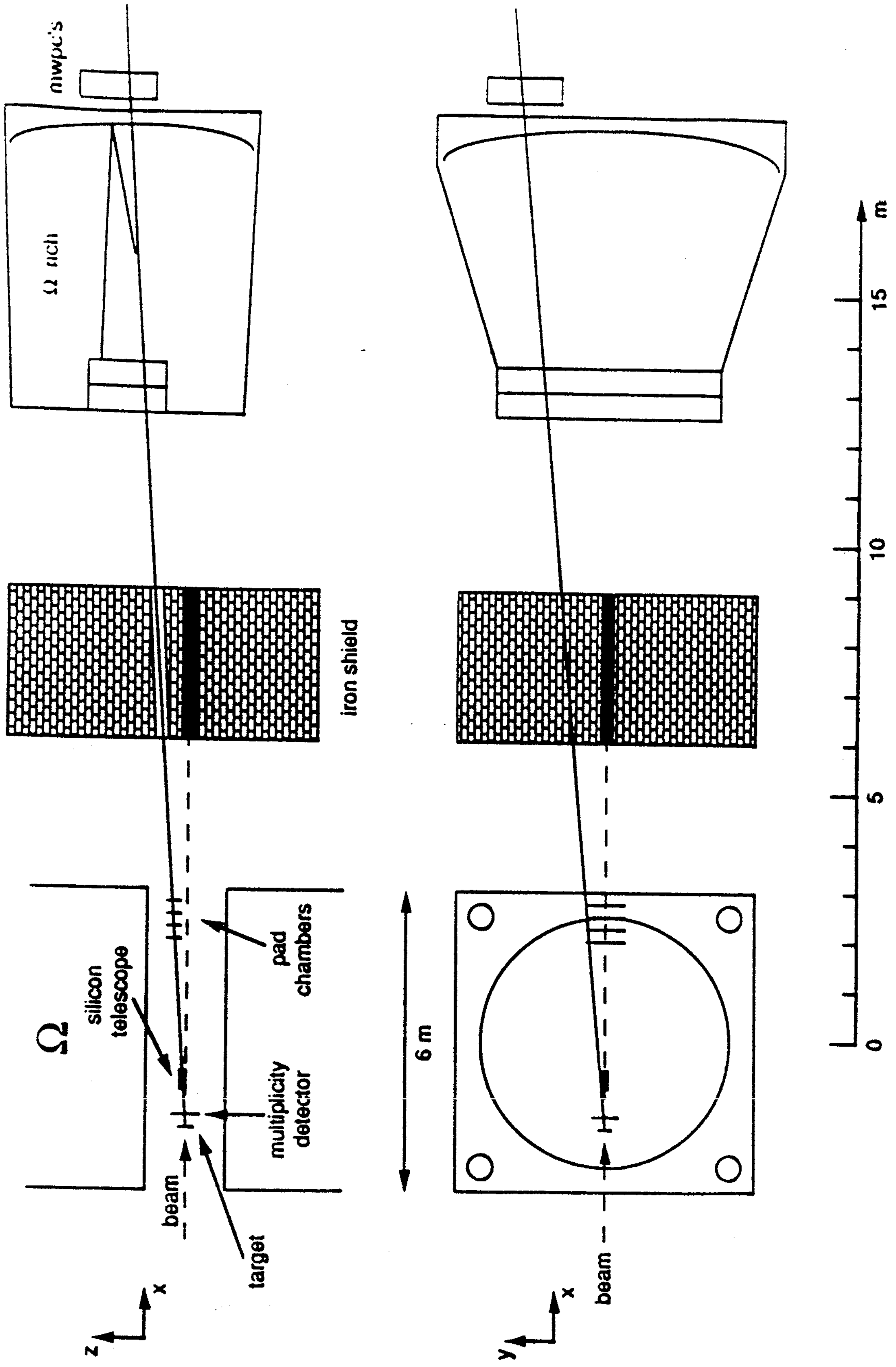

Figure 6.1: Experimental setup for WA97

arranged with a central hole to avoid secondary interactions. The arm in the positive Z direction is removed to avoid interactions in the path of the other detectors in the setup.

The multiplicity detector will be used in the trigger, and to provide information on charged particle multiplicity which will be used to estimate the centrality of the collisions.

6.2.2 The silicon telescope

The silicon microstrip planes used in WA94 are supplemented by several pad planes, with two-dimensional readout. These planes, which have a coarser resolution (around 1 mm) than the ordinary strips, will be used to resolve ambiguities arising from the one-dimensional measurements of the ordinary microstrips. The one-dimensional strips have a pitch of 50 μm. The new telescope is configured as five plus one triplets, consisting of one pad plane, one Y plane and one Z plane. The first five triplets make up the body of the telescope, and cover an X distance of 25 cm. The sixth triplet is placed further downstream, and works as a lever arm detector to improve the momentum resolution.

The silicon telescope is the heart of the experimental setup, and it will be used as tracking device. By locating the telescope at at three different positions, one unit of rapidity can be covered. (The acceptance will be in the region $y = -1$ to $y = 1$ in the centre-of-mass frame.) The acceptance varies for each particle species in question. The acceptance for Λs are shown in figure 6.2, taken from [Arm91]. The lower threshold on the transverse momentum will be p_t= 0.5 GeV/c.

By further rearrangement the same apparatus can be made to cover a rapidity window of $\pm$ 2 units at a later stage.

A newly developed pixel plane was tested in the 1992 run of WA94 [Beu90]. The pixels have two-dimensional readout like the pads, but their resolution is the same order as the ordinary microstrips. If the development of such planes proves succesful, they may be used to improve the quality of the WA97 telescope.

6.2.3 Pad chambers

The Omega wire chambers will be replaced by newly developed pad chambers, with two-dimensional readout. This is necessary to handle the large multiplicities in lead-lead interactions. The pad chambers will be located between 3.4 and 4.2 metres downstream from the target. They will provide extra space points on the charged particle tracks, both to improve the momentum resolution and to provide reliable track extrapolation to the RICH.

6.2.4 The RICH detector

The Omega RICH will be used to identify protons and antiprotons, as discussed in some detail in the previous chapter. The need for further shielding or improved pattern recognition algorithms will be investigated when experimental results from WA94 become available.

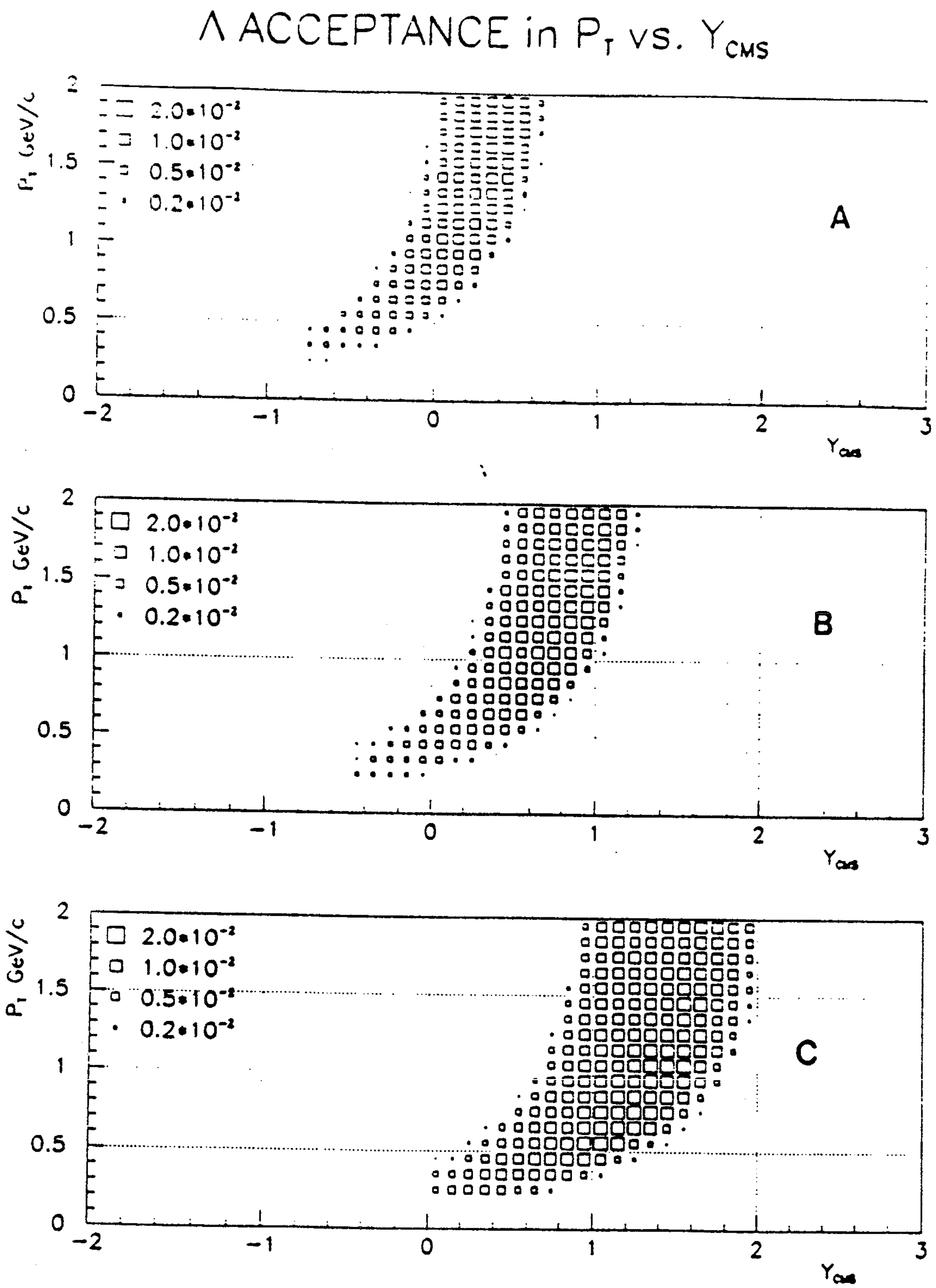

Figure 6.2: WA97 acceptance for Λs. Each plot (A,B and C) corresponds to different telescope locations.

Chapter 7

Summary and outlook

During the last five years an extensive experimental programme on relativistic heavy ion collisions has been carried out by several groups. No unambigous signal of quark gluon plasma is observed yet.

An increased production of strange antiquarks has been proposed as a good signal of quark gluon plasma formation, although an effect has also been seen in purely hadronic models.

The high $\overline{\Xi^-}/\overline{\Lambda}$ ratio observed in the WA85 1987 data is not explained by any hadronic model. It has been argued thet this might be a signal of a quark gluon plasma formation.

The error bars on the measured ratio are large, mainly due to poor statistics. The increased statistics of the 1990 data will help clarify the experimental situation.

An overall increase in strangeness production about a factor of two is observed in sulphur-tungsten collisions compared to proton-tungsten reactions. This result is in general agreement with the other experiments that measure strangeness production in heavy ion collisions. This increase can be explained by rescatterings in a dense hadron gas [Cle91], although there is some disagreement whether the equlibration time required by such models is realistic [Egg91].

The lack of conclusiveness in the overall strangeness production result suggests further investigations of the detailed mechanisms involved in strangeness production. Strange antibaryons has been suggested as a particularly well suited observable for plasma production, encouraged by the WA85 result.

Further experimental efforts will be devoted to obtaining production yields of as many different particle species as possible. Omegas and anti-omegas will probably be identified with the increased statistics of the 1990 data.

In order to compare the production of strange and non-strange baryons and antibaryons, protons and anti-protons must be identified among the non-decaying particles in the experiment. Simulation studies indicates that particle identification with a RICH counter is feasible, once a series of measures are taken to reduce the charged particle multiplicity in the RICH.

Experimental data with the RICH detector were taken in spring 1992. The result looks promising, although no real analysis has been possible yet. The background is slightly higher than in the simulation studies, but not alarmingly much (less than a factor two). The real test of merit of the detector system can be carried out when the telescope tracking is completed, and the RICH can be calibrated and its final signal extracted.

The results foreseen from the symmetric sulphur-sulphur interactions in the WA94 experiment will be interesting in their own right, but they will also provide a suitable comparison to the results from the lead-lead collisions to be measured by WA97.

If a phase transition to quark matter occurs, the plasma phase should be more developed in the larger system of lead-lead interactions than is the case in central sulphur-tungsten reactions. A larger system will provide longer life times for the hot central zone, making plasma equilibration more likely. The strangeness enhancement signal is based on thermodynamical equilibrium, making detailed measurements of strange particle production even more important in the future lead experiments.

References

[Aba90] WA85 Collaboration:, S. Abatzis, *et al.*, Phys. Lett. **B244** (1990) 130.

[Aba91] WA85 Collaboration:, S. Abatzis, *et al.*, Phys. Lett. **B259** (1991) 508.

[Aba91a] WA85 Collaboration:, S. Abatzis, *et al.*, Phys. Lett. **B270** (1991) 123.

[Abb91] E802 Collaboration:, T. Abbott, *et al.*, Phys. Rev. Lett. **66** (1991) 1567.

[Ake90] NA34 Collaboration:, T. Åkesson, *et al.*, Z. Phys. **C46** (1990) 369.

[Alb91] WA80 Collaboration:, R. Albrecht, *et al.*, Z. Phys. **C51** (1991) 1.

[Ale90] E735 Collaboration:, T. Alexopoulus, *et al.*, Phys. Rev. Lett. **64** (1990) 991.

[Ame90] N. S. Amelin, K. K. Gudima, S. Y. Sivoklokov, and V. D. Toneev, Sov. J. Nucl. Phys. **52** (1990) 172.

[Ant79] D. Antresayan *et al.*, Phys. Rev. **D19** (1979) 764.

[Aps86] R. J. Apsimon *et al.*, Nucl. Inst. and Meth. **A248** (1986) 76.

[Arm91] WA97 Collaboration:, N. Armenise, *et al.*, WA97 proposal, Technical Report 91-29, CERN/SPSLC, 1991.

[Bag91] NA38 Collaboration:, C. Baglin, *et al.*, Phys. Lett. **B255** (1991) 459.

[Bam88] NA35 Collaboration:, A. Bamberger, *et al.*, Phys. Lett. **B203** (1988) 320.

[Bam89] NA35 Collaboration:, A. Bamberger, *et al.*, Z. Phys. **C43** (1989) 25.

[Bam90] NA35 Collaboration:, A. Bamberger, *et al.*, Z. Phys. **C48** (1990) 191.

[Bar93] R. P. Barnes, Private communication.

[Ben85] H.-U. Bengtsson and T. Sjöstrand, University of Lund Preprint **LU TP 85-10** (1985).

[Ben86] H.-U. Bengtsson and T. Sjöstrand, University of Lund Preprint **LU TP 86-22** (1986).

[Beu84] W. Beucsh, Omega prime, Technical Report 84-62, CERN/SPSC, 1984.

[Beu86] W. Beusch, Nucl. Instr. and Meth. **A249** (1986) 391.

[Beu90] W. Beusch *et al.*, R& D Proposal. Development of hybrid and monolithic silicon micropattern detectors, Technical Report 90-81/P22, CERN/DRDC, 1990.

[Bur86] JACEE Collaboration:, T. H. Burnett, *et al.*, Phys. Rev. Lett. **57** (1986) 3249.

[Bus88] NA38 Collaboration:, A. Bussiere, *et al.*, Z. Phys. **C38** (1988) 117.

[Che37] P. A. Čerenkov, Phys. Rev. **52** (1937) 378.

[Cho74] A. Chodos, R. L. Jaffe, K. Johnson, C. B. Thorn, and V. F. Weisskopf, Phys. Rev. **D9** (1974) 3471.

[Cle91] J. Cleymans, Nucl. Phys. **A525** (1991) 205c.

[Col75] J. Collins and M. Perry, Phys. Rev. Lett. **34** (1975) 1353.

[Cro75] J. W. Cronin *et al.*, Phys. Rev. **D11** (1975) 3105.

[Cse89] L. P. Csernai, A. K. Holme, and E. F. Staubo, What can we learn from pt distributions in relativistic heavy ion collisions?, in *The Nuclear Equation of State*, edited by W. Greiner, p. 369, Plenum Press, 1989.

[Cse92] L. P. Csernai, Hydrodynamic flow, in *Proceedings NATO/ASI '92. 'Particle Production in Highly Excited Matter'*, edited by H. Gutbrod and J. Rafelski, To be published by Plenum Press, 1993.

[Dra92] NA38 Collaboration:, O. Drapier, *et al.*, Nucl. Phys. **A544** (1992) 209c.

[Egg91] H. C. Eggers and J. Rafelski, Int. Journ. of Mod. Phys. **A6** (1991) 1067.

[Eis92] E810 Collaboration:, S. E. Eiseman, *et al.*, Phys. Lett. **B297** (1992) 44.

[Eke84] T. Ekelöf. CERN-EP **84-168** (1984).

[Eng92] J. Engelfried, *Einsatz eines Ringabbildende Cherenkovzählers zur Suche nach dem exotischen Zustand U(3100)*, PhD thesis, Ruprecht-Karls-Universität Heidelberg, 1992.

[Eng92a] J. Engelfried, Private communication.

[Eva92] D. Evans. *Strange and Multistrange Baryon and Antibaryon Production in Sulphur-Tungsten Interactions at 200 GeV/c per Nucleon*, PhD thesis, University of Birmingham, 1992.

[Eva93] D. Evans. Private communication.

[Fol92] E810 Collaboration:, K. J. F. Foley, *et al.*, Nucl. Phys. **A544** (1992) 335c.

[For87] WA89 Collaboration:, A. Forino, *et al.*, WA89 proposal, Technical Report 87-43, CERN/SPSC, 1987.

[Ger92] C. Gerschel and J. Hüfner, Nucl. Phys. **A544** (1992) 513.

[Gol60] G. Goldhaber, S. Goldhaber, W. Lee, and A. Pais, Phys. Rev. **120** (1960) 300.

[Gon93] E866 Collaboration:, M. Gonin, *et al.*, Nucl. Phys. **A553** (1993) 799c.

[Gre92] NA36 Collaboration:, D. E. Greiner, *et al.*, Nucl. Phys. **A544** (1992) 309c.

[Hag83] R. Hagedorn, Riv. Nuovo Cimento **6** (1983) 1.

[Han54] R. Hanbury Brown and R. Q. Twiss, Phil. Mag. **45** (1954) 663.

[Han56] R. Hanbury Brown and R. Q. Twiss, Nature **178** (1956) 1046.

[Hol93] A. K. Holme and G. Undheim, Private communication.

[Jac91] B. Jacak, Nucl. Phys. **A525** (1991) 77.

[Jud92] E. G. Judd, PhD thesis, University of Birmingham, 1992.

[Kam92] WA80 Collaboration:, K. H. Kampert, *et al.*, Nucl. Phys. **A544** (1992) 183.

[Kar87] F. Karsch, J. Kogut, D. K. Sinclair, and H. W. Wyld, Phys. Lett. **B188** (1987) 353.

[Kar90] F. Karsch, Simulating the quark-gluon plasma on the lattice, in *Quark-Gluon Plasma*, edited by R. C. Hwa, p. 61, World Scientific, 1990.

[Kin92] WA85 Collaboration:, J. B. Kinson, *et al.*, Nucl. Phys. **A544** (1992) 321c.

[Koc86] P. Koch, B. Müller, and J. Rafelski, Phys. Rep. **142** (1986) 167.

[Koc90] P. Koch, U. Heinz, and J. Pišút, Phys. Lett. **B243** (1990) 149.

[Kow92] NA35 Collaboration:, M. Kowalski, *et al.*, Nucl. Phys. **A544** (1992) 609c.

[Las79] J. C. Lassalle *et al.*, *TRIDENT manual*, CERN DD/EE/79-2.

[Las80] J. C. Lassalle *et al.*, Nucl. Instr. and Meth. **176** (1980) 371.

[Lov93] G. Løvhøiden and T. Storås, Private communication.

[Mat86] T. Matsui and H. Satz, Phys. Lett. **B178** (1986) 416.

[Mia91] E802 Collaboration:, Y. Miake, *et al.*, Nucl. Phys. **A525** (1991) 231.

[Mul92] B. Müller, Nucl. Phys. **A544** (1992) 95c.

[Mul92a] B. Müller, Physics of quark gluon plasma, in *Proceedings NATO/ASI '92, 'Particle Production in Highly Excited Matter'*, edited by H. Gutbrod and J. Rafelski, To be published by Plenum Press, 1993.

[Nag92] S. Nagamiya, Nucl. Phys. **A544** (1992) 5c.

[Nar91] WA85 Collaboration:, J. L. Narjoux, *et al.*, Nucl. Phys. **A525** (1991) 445c.

[Pet91] B. Peterson, Nucl. Phys. **A525** (1991) 237c.

[Pod54] J. Podolanski and R. Armenteros, Phil. Mag. **45** (1954) 13.

[ppd90] Particle Data Group, Particle Properties Data Booklet, North-Holland, April 1990.

[Raf91] J. Rafelski, Phys. Lett. **B262** (1991) 333.

[Ruu92] P. V. Ruuskanen, Nucl. Phys. **A544** (1992) 169c.

[Sak92] NA36 Collaboration:, I. Sakrejda, *et al.*, Strangeness production in s+pb and p+pb collisions at 200 gev/c per nucleon, in *Hadron Structure '92*, edited by D. Brancko and J. Urbán, p. 108, 1992.

[Sch92] H. R. Schmidt and J. Schukraft, CERN/PPE 92-42; To be published in Int. J. of Mod. Phys. G (1992).

[Sey92] NA35 Collaboration:, P. Seyboth, *et al.*, Nucl. Phys. **A544** (1992) 293.

[Sor92] H. Sorge, RQMD, in *Proceedings NATO/ASI '92, 'Particle Production in Highly Excited Matter'*, edited by H. Gutbrod and J. Rafelski, To be published by Plenum Press, 1993.

[vHe91] NA34 Collaboration:, H. van Hecke, *et al.*, Nucl. Phys **A525** (1991) 227c.

[vHo85] L. van Hove, Z. Phys **C27** (1985) 135.

[vHo88] L. van Hove, CERN preprint **TH-5236** (1988).

[Zaj92] E802 Collaboration:, W. A. Zajc, *et al.*, Nucl. Phys **A544** (1992) 237.

[Zim92] J. Zimanyi, Rehadronisation, in *Proceedings NATO/ASI '92, 'Particle Production in Highly Excited Matter'*, edited by H. Gutbrod and J. Rafelski, To be published by Plenum Press, 1993.